Modeling of Particle Trajectories in an Electrostatic Precipitator (ESP) for Small-Scale Wood Combustion

Janne-Petteri Niemelä

Master's Thesis
University of Jyväskylä
Department of Physics
Master's Degree Programme in Renewable Energy
25 March 2009

Foreword

This thesis can be seen as a continuation of earlier research done in 2006-7 as part of the MiniDust Project co-ordinated by VTT and the Universities of Jyväskylä and Tampere. In the MiniDust project the feasibility of electrostatic precipitation for small-scale wood combustion devices was studied. The experimental results of the of the said project and the information gathered by Ismo Talka in his Master's Thesis, Pienpolton hiukkasten sähköinen suodattaminen, have beed the invaluable bases for my work. Besides Ismo Talka, I wish to thank my supervisors Jussi Maunuksela and Martti Aho for advice. The inspectors of the thesis are Ari Laitinen (TTY) and Ari Jäsberg (VTT/JYU).

Janne-Petteri Niemelä

25 March 2009

Abstract

This paper presents a mathematical model for particle trajectory simulation in overlapping gas velocity and electric fields of a two-stage electrostatic precipitator in order to provide the means for further feasibility analysis for small-scale wood combustion flue gas after treatment. The flue gas velocity field is generated solving the incompressible Navier-Stokes equation, whereas to produce the electric field the Poisson's equation is resolved. All the simulations are executed employing commercial Comsol 3.4 software. It was of interest to discover whether it would be reasonable to build an ESP with no ion source in the precipitation stage. Consequently, particular attention was given to particle diffusion charging, finally calculated as suggested by the Source-and-Sink method. The results show that the charge levels of larger particles $d_p \approx 1\ \mu m$ at typical charging conditions $N_i t = 10^{13}\ s/m^3$, where N_i is the ion concentration and t is the charging time, are too low for satisfactory precipitation. Furthermore, at $N_i t = 10^{12}\ s/m^3$ the charge acquired by the smaller than 0.1 μm particles also remains insufficient. The simulated results for required plate lengths for collection are in good agreement with predictions of laminar collection efficiency equation, which was expected for low Reynolds number flows studied. For a 0.1 μm particle, corresponding to the mode of a typical size distribution of wood combustion flue gas, the plate length required for collection is 0.14 m at $N_i t = 10^{13}\ s/m^3$, $T = 130\ ^oC$ and $E = 400\ kV/m$ for flow velocity 0.13 m/s, in the absence of space charge. Space charge densities of around $7 \cdot 10^{-7}\ C/m^3$, corresponding to measured particle number concentration of $7 \cdot 10^{11}\ 1/m^3$, caused approximately 1 % electric field perturbation. This level is too modest to interfere with the particle capture. Furthermore, the hypothetical densities of order $10^{-5}\ C/m^3$ and $10^{-4}\ C/m^3$ were found to have slightly and seriously harmfull impacts respectively on precipitation. The simulation results support the analytical prediction in that the implementing electrostatic precipitation in small wood-fired appliances seems feasible, provided the sufficient charging conditions.

Contents

1 Introduction **1**

2 Why Is Particle Removal Needed? **3**

3 Why an ESP? **5**
3.1 Electrostatic Precipitator 5
3.2 Review of Present Small-Scale ESPs for Wood Combustion . . 6
3.3 The New ESP Configurations 7
3.3.1 The Helicoidal ESP 7
3.3.2 The Rotating Plate ESP 7

4 Electric Field Equations **9**
4.1 About Electrostatics 9
4.1.1 Polarization 9
4.2 Poisson's Equation 12
4.3 Electric Displacement Vector 13
4.4 Boundary Conditions for the Poisson Equation 14

5 Flow Velocity Field Equations **15**
5.1 About Fluid Kinematics 15
5.1.1 Acceleration Corresponding to a Velocity Field 16
5.1.2 The Equation of Continuity, i.e., A Local Equation for Conservation of Mass 16
5.1.3 Velocity Gradient Tensor 18
5.2 About Fluid Dynamics 19
5.2.1 The Stress Tensor 19
5.3 The Navier-Stokes Equation 21
5.4 Boundary conditions for the Navier-Stokes Equation 24

6 Fluid Properties of Flue Gas of Wood Combustion **27**
6.1 Viscosity 27
6.2 The Reynolds Number 27
6.3 Flow Velocity Profile And Analysis Of The Nature Of The Flow Based on Reynolds Number 29
6.4 The Mean Free Path Of A Gas 31

7 Particle Properties of Flue Gas from Wood Combustion **32**
7.1 Particles' Size And Shape 32
7.1.1 The Particle Size Distribution 33
7.1.2 The Cunningham Slip Correction Factor 33

7.2 Cohesivity and Resistivity of the Particles 34
7.3 Particle Charging 35
7.3.1 The Limiting-Sphere Theory 37
7.3.2 Ion Properties 39
7.3.3 The Source-and-Sink Method 40
7.4 Particle Equation Of Motion 44
7.5 Particle Migration 46
7.6 Collection Efficiency 48
7.7 Influence of Space Charge 49
7.7.1 Turbulent Space Charge Profile 49
7.7.2 Laminar Space Charge Profile 52

8 Overview of the Model 55

9 Simulations, Results and Discussion 57
9.1 Comparison of the Proposed ESP Configurations 57
9.1.1 The Rotating Plate ESP, 2D 58
9.1.2 The Rotating Plate ESP, 3D 62
9.1.3 The Helicoidal Type ESP, 2D 64
9.1.4 The Helicoidal Type ESP, 3D 68
9.2 Influence of the Space Charge Density 69
9.2.1 Constant Space Charge Density 69
9.2.2 Turbulent Space Charge Profile 73
9.2.3 Laminar Space Charge Profile 74

10 Conclusions 77

A Appendix, Particulate Matter Deposition in the Human Organism 84

B Appendix, Health Impact Of Particulate Matter Exposure 85

C Appendix, The Structure of the Rotating Plate ESP 86

D Appendix, The Structure of the Helicoidal ESP 88

E Appendix, Resolving the Problems in Below-$1\mu m$ Particle Tracing with 'the Equivalence Velocity Principle' 89

List of Symbols

A	Area $[m^2]$
a	Radius of an aerosol particle $[m]$
a_f	Size of a fluid element $[m]$
$\vec{a}$	Amount of distortion of the charge distributions of single atoms $[m]$
α	Collision probability
b	Collision parameter $[m]$
C	Capacitance $[F]$
C_u	Cunningham slip correction factor
C_0	Capacitance in vacuum $[F]$
c_i	Mean thermal speed of ions $[m/s]$
χ_E	Electric susceptibility
$\vec{D}$	Electric displacement $[(C \cdot m)/m^3]$
D_i	Diffusion coefficient of ions $[m^2/s]$
d	The plate distance $[m]$
d_{ij}	The deviator tensor $[1/s]$
d_m	The collision diameter of gas molecules $[m]$
d_p	The particle diameter $[m]$
δ	Limiting sphere radius $[m]$
δ_{ij}	The Kronecker delta
$\vec{E}$	Electric field $[V/m]$
e	Elementary charge ($e = +1.602 \cdot 10^{-19}\ C$)
e_{ij}	The symmetric component of the velocity gradient tensor $[1/s]$
ϵ_0	The electrical permittivity of vacuum ($\epsilon_0 = 8.854 * 1012 F/m$)
ϵ	The relative permittivity
η	Dynamic viscosity $[Pa \cdot s]$
η_r	Reference viscosity $[Pa \cdot s]$
F_w	Drag force $[N]$
$F_e l$	Electrical force $[N]$
F_I	Inertial force $[N]$
F_f	Frictional force $[N]$
ϕ	Electric potential $[V]$
Φ	Ion-particle interaction potential energy $[J]$
g_{ij}	The velocity gradient tensor $[1/s]$
J	Ion flux on a particle of given size $[1/s]$
L	Characteristic length of a flow channel or of a particle $[m]$
λ	The mean free path $[m]$
λ_i	The mean free path of ions $[m]$
m	mass $[kg]$

n	Number of ions or elemental charges
n_m	Molecular concentration $[1/m^3]$
$\vec{n}$	A normal vector of a surface $[m]$
N	Number of atoms per unit volume $[1/m^3]$
N_A	Avogadro's number ($N_A = 6.022 * 10231/mol$)
ω_{ij}	The antisymmetric term of the velocity gradient tensor $[1/s]$
$\vec{P}$	Polarization per unit volume $[(C \cdot m)/m^3]$
p	Hydrostatic pressure$[Pa]$
Q	Volume flow $[m^3/s]$
Q_p^∞	The Coshet particle saturation charge $[C]$
q_{surf}	Surface charge $[C/m^2]$
$\vec{r}$	Position vector $[m]$
R	The universal gas constant ($8.314 J/(mol \cdot K)$)
R_e	Flow Reynolds number
$R_{e,p}$	Particle Reynolds number
ρ	Mass density $[kg/m^3]$
ρ_{el}	Particle dust electric resistivity $[\Omega m]$
ρ_f	Fluid Density $[kg/m^3]$
ρ_{tot}	Total charge density $[C/m^3]$
ρ_p	Polarization charge density $[C/m^3]$
ρ_{pa}	Density of a particle $[C/m^3]$
ρ_s	Space charge density $[C/m^3]$
S	Sutherland interpolation constant $[K]$
σ_{ij}	The stress tensor $[N/m^2]$
σ'_{ij}	The viscosity stress tensor $[N/m^2]$
t	Time $[s]$
T	Flue gas temperature $[K]$
T_r	The reference temperature $[K]$
$\vec{\tau}$	A tangential vector of a surface $[m]$
U	The speed of the flow $[m/s]$
$\vec{U}$	Eulerian velocity $[m/s]$
$\vec{u}$	Lagrangian velocity $[m/s]$
V	Volume $[m^3]$
V_m	Molar volume of the aerosol $[m^3/mol]$
V_f	Volume of a fluid particle $[\mathrm{m}^3]$
w	Migration velocity $[m/s]$
w_{th}	The theoretical migration velocity $[m/s]$
ξ	Bulk viscosity $[Pa \cdot s]$
Z	Number of electrons in a atom
Z_i	Electrical mobility of ions $[m^2/(Vs)]$

1 Introduction

Due to increased awareness of anthropogenic nature of climate change, the pressure to enhance renewable energy utilization is increasing. Small-scale wood combustion is a possible field where some enhancement can be gained. Unfortunately, small wood-fired appliances are already causing significant amount of air pollution, leading to many premature deaths. Particulate matter emissions of wood combustion can be cut by improving the existing combustion technology or by flue gas after treatment. Developing a simple but efficient electrostatic precipitator (ESP) could be a solution to the problem. An ESP is a device that is used to separate and collect charged particles from a fluid flow. Once charged, the particulates are subjected to an electric field with intention to deflect them to collector plates.

In this paper a mathematical particle trajectory model for a two-stage ESP is developed. Modeling of the phenomena occurring in an ESP is a real multiphysics task. The electrohydrodynamics of flue gases is studied solving the Navier-Stokes equation for gas velocity and the Poisson's equation for electric potential employing the Mulphysics mode of commercial Comsol 3.4. software. Finally, the particle trajectories are calculated in the said overlapping vector fields. It is of interest to discover whether it would be reasonable to build an ESP with no ion source in the precipitation stage. Consequently, particle charging is studied assuming firstly and primarily diffusion charging, as yielded by the Source-and-Sink method, and secondly combined charging. As a consequence of complex nature of the physics involved, and the scope of this thesis, various simplifying assumptions have to be taken. Nevertheless, the flue gas particle trajectories in the presence of gas flow field and electric field are calculated also taking roughly into account the particle space charge effects. When possible, property values are obtained from the previous measurements done as part of the MiniDust project, realized 2006-2007 in cooperation between the University of Jyväskylä, the University of Tampere, VTT and industrial partners.

In Chapter 2 we briefly consider the importance of fine particle control based on the emission characteristics, the health impact and the legislative issues. Once motivated, in Chapter 3 we get convinced that ESPs are indeed the devices that provide the means for particle removal for small-scale wood combustion. This chapter also includes brief discussions of the basic principle of ESPs, a review of the present small-scale ESPs for wood-fired appliances and an introduction of the two configurations suggested based on the

groundwork done in the MiniDust project. In Chapters 4 and 5 we derive the field equations required to model the wanted electrical and flow conditions, respectively, whereas in Chapters 6 and 7 the fluid and the particle properties of wood combustion aerosols are discussed, simultaneously supporting the introduced equations with illustrative example plots corresponding to realistic conditions, consequently fixing the property values needed in the simulations. In Chapter 8 the model developed and its philosophy is summarized to provide a brief overall view before the simulations, results and discussion, presented in Chapter 9. Based on particle trajectory analysis, the conclusions are drawn in Chapter 10. Furthermore, in Appendixes A - D some extra information is provided on health impacts due to the particulate matter exposure and equivalence velocity principle used in particle tracing, additionally including a description of the two ESP configurations.

2 Why Is Particle Removal Needed?

The famous 20-20-20-target of the European Union (EU) member states is to reduce the CO_2 emissions by 20 % compared to 1990 level and increase the utilization of renewable energy up to 20 % of total by 2020 [17]. Additional wood fuel consumption, in both large and small-scale, is favorable for achieving both of these goals. Therefore, even though the emissions of particulate matter, and those of methane for old wood boilers are relatively high for wood combustion, actually higher than for example for oil [19], a reduction of wood fuel usage is not in sight, thus implying a tendency towards increase in flue gas emissions.

The flue gases, treated as aerosols, are typically characterized by particle diameter. The majority of small-scale wood combustion particulate emissions are found in the fine particle (PM2.5) region and the results of a present study [10], imply that in Finland the largest fractions of the local fine particulate matter emissions are, indeed, formed by small-scale wood combustion (41 %), power plants (24 %), domestic traffic (13 %), and industry (8 %). Harmfulness of the traffic and small-scale combustion pollution is largely due to low emission height, because of which, the particle concentration remains high until the transportation to the respiratory systems. Thus, it is likely that traffic and small-scale combustion emissions are a major cause of health hazards in Finland. [10]

Fine particle emissions from wood combustion are mainly formed by fly ash, soot and tar compounds. The composition of emissions varies with combustion device, burning conditions and quality of the fuel. The fly ash of wood is formed mainly by cooling of Alkali metals and Alkaline earth metals (Na, K, Mg, Ca) evaporated in combustion. The size distribution of fly ash, ranging from below 0.1 μm up to over 100 μm, has notable modes at around 0.3 μm and $50 - 100$ μm, the previous contributing unfavorably in PM2.5 region. Soot particles emitted typically have a chain-like agglomerate structure consisting of almost symmetrical, spherical primary particles with diameters around $0.03-0.04$ μm. The surface layer is mainly formed of stable elemental carbon, whereas the core is occupied by easily oxidized carcinogenic PAH compounds. Tar, also know as heavy condensed hydrocarbons, for its part, is a very complicated mixture of even 200 compounds and its formation is strongly influenced by water content of the fuel [11, 8].

In Clean Air for Europe project the health impacts of PM2.5 exposure were investigated resulting a suggestion that in the area of EU25 the number of PM2.5 originated premature deaths would rise even up to 347900, and in Finland, correspondingly, up to 1270. Generally, the ones having respiratory diseases are, in addition to the elderly and the infants, the most vulnerable

to the particulate matter exposure. Fine particulates are transported to human organism through the respiratory passage, and how far or to which part of it, depends on the particle size. The most hazardous impact on human health is caused by the ultra-fine particulates, $0.01 - 0.1\ \mu m$ in diameter, of which a half can drift to the lower respiratory system, *i.e.*, to the bronchi and the alveoli, where they can enter to blood circulation. Through blood circulation thay can get absorbed by the organs, possibly inducing change in DNA copying process or transformation of DNA often triggered by PAHs. As a consequence, there is increased risk of heart diseases and inflammations in respiratory passage, to mention the most common ones of the severe implications of PM2.5 exposure (see Appendixes A and B). [10]

At present the fine particulates are only regulated as a part of PM10. However, due to increased knowledge about the health hazards caused by fine particulates, the EU has recently taken steps aiming at regulation of PM2.5 concentration in ambient air. Clean Air for Europe (CAFE) Programme was launched in 2001, under the Sixth Environmental Action Programme, in order to improve the air quality management in Europe, and as an outcome the European Commission came up with a Thematic Strategy on air pollution on 21.9.2005, on which the European Council adopted the "the Council conclusions" on 15.3.2006 [14, 13]. The strategy sets multi-stage objectives to be completely attained by 2020, implying PM2.5-concentration to be reduced by 75 % from what is technically feasible, meaning reduction of primary PM2.5 emissions by 59 % relative to the year 2000 level. Following the guidelines of the Thematic Strategy the European Commission has presented a Proposal for a Directive of the European Parliament and of the Council on ambient air quality and cleaner air for Europe [15]. The proposal for "CAFE" Directive suggests, based on ambition levels assessed in Ref. [16], exposure reduction target of 20 % to be attained between 2010 and 2020 and concentration cap for PM2.5 of 25 $\mu g/m^3$. Nevertheless, the limits proposed can be argued to be insufficient if compared to 10 $\mu g/m^3$, that is WHOs global guideline value for concentration cap [18]. What comes to small-scale combustion, the Commission will examine the need to set emission standards for below 50 MW power plants and the domestic combustion appliances [13].

To be able to fulfill the need to reduce the concentration of particulate matter in the ambient air, above all PM2.5, the emission sources have to be controlled. Because small-scale wood combustion is of special importance in Finland, serious attention should be given to flue gas after treatment. Probably the best solution for particle capture in small wood-fired appliances would be an electrostatic precipitator.

3 Why an ESP?

To filter the particles from flue gas, various methods exist. The boundary conditions set by small-scale wood combustion are the requirements for simplicity, moderate material costs compared to the price of the burning device, practically automated maintenance and of course small dimensions. In addition, one has to bear in mind the relatively high operating temperatures around 150 ^oC, and possible corrosive effects when operating around the condensation point.

The typical methods for separation of aerosol particulates include inertial separation used in cyclones and impactors, diffusion as used in fabric filtration, impingement and contacting as applied in wet scrubbers, diffusion in the case of fabric filtration and electrical means as applied in electrostatic precipitators. Normally the size distribution of wood combustion flue gas particulates has a mean around 0.1 μm [19, **?**, 8]. According to Ref. [2] electrostatic precipitators are the only ones, of the above mentioned devices, that can separate particles smaller than 0.1 μm in diameter making the choice of method for flue gas after treatment for wood burning appliances evident. In Ref. [20] a wet type ESP is discussed reporting excellent achieved collection efficiencies and low power consumption. Nevertheless, keeping in mind the small-scale requirement of simplicity, the wet type applications of ESPs, involving extra equipment for water treatment, can be excluded, at least in the preliminary designs.

3.1 Electrostatic Precipitator

When considering particulates suspended in combustion flue gases, we are talking about PM10 and PM2.5. Thus we are dealing with quite small bodies having small masses for which gravitational force and inertial forces are outweighed by electrostatic forces. This is the physical fact exploited in electrostatic precipitators. Having an intention to capture the particles taking advantage of electric force, the first step is to charge the particles. This is typically achieved using corona discharge, producing ion wind, followed by particle charging by means of field and diffusion charging, respectively. Once particles are charged they can be deflected with electric field induced by a potential difference applied. The deflection is intended to be such that the trajectories of the particles end on the surface of collector electrodes. The last step is to remove the accumulated dust layer, typically by rapping or washing, to hoppers placed outside of the flow stream. [1]

ESPs can be classified according to charging location of the particulates. If charging is done before the actual collection section, we talk about two-

stage ESPs, whereas if the charging procedure is realized between the collector plates in the collecting zone itself, we refer to one-stage ESPs. Most of the industrial applications seem to be one-stage ESPs.

Furthermore, two typical configurations dominate in the field of industrial ESPs. In plate type ESPs the corona wires are placed between parallel, typically grounded, plates constituting an entity of one or more units mounted in series or parallel. Other frequent configuration is tubular type ESP, in which the corona discharge element lies on the axis of a tube whose walls function as grounded collection surfaces.

Compared to small scale applications, industrial scale possesse the advantage of allowing the use of complex rapping systems, maintenance personnel and larger dimensions allowing positioning of elements, such as insulators, well away from the peak electric field. So even though in theory there are no reasons why the electrostatic precipitation method could not be applied on a small scale as well, in practice some problems, mainly related to cleaning of both the collector surfaces and the insulators, have to be overcome.

3.2 Review of Present Small-Scale ESPs for Wood Combustion

The method of electrostatic precipitation is widely used on the industrial scale but so far in applying the method in small-scale combustion little improvement has taken place. As discussed in Chapter 2, the absence of small-scale ESPs is mainly due to lack of binding emission control legislation. Nevertheless, some effort have been made at least in Norway and Switzerland. The Swiss application, a simple tubular type ESP, that is compatible with wood fueled devices smaller than 35 kW has been reported to reach average efficiency up to 73 %. This application seems to have reached the point of commercialization by the patent owner Swiss Rüegg Cheminée AG. In it the problem of dust build up on insulator is solved by blowing air on it with a small fan, but the means for tube wall cleaning are not explained. Probably conventional Chimney sweeping is assumed. [9]

Recently in Finland there has been some progress in the area of small scale wood combustion particle capture, even outside the MiniDust project. European patent application was published in 13.08.2008 claiming rights for an invention that relates to a method and device for purifying flue gas containing particles, in which method the flue gas is cooled to below the condensation point of water vapor and the fine particles in the flue gas are bound mainly to drops and/or a liquid film, and further collected exploiting gravitational pull [21]. The invention is not an ESP but competes in the same league

of emission control for small wood-fired appliances. This technique might seem quite complex, involving a water circulation system along all the chimney length, to be adopted economically and without excessive challenge to small-scale devices and already-mounted chimneys.

3.3 The New ESP Configurations

As a part of the MiniDust project, electrostatic precipitation of particulate matter emissions of small-scale wood combustion was studied. Based on the results of the project two new ESP concepts have been introduced. One by a former researcher of the project and other by the author of this thesis. Both concepts, described more in detail in Appendixes C and D, are two-stage by type. Also in this paper, where possible conclusions are drawn based on simulations performed, and the two configurations are compared and evaluated.

3.3.1 The Helicoidal ESP

Ismo Talka worked as a researcher in the MiniDust project and has later suggested a new helicoidal ESP configuration to be applicable to particulate matter precipitation in small-scale. In his vision the flue gas is led through a flow channel consisting of two coaxial helixes and a tube. Through the inner, smaller helix negative potential is provided, whereas the outer, larger helix and the tube serve as collection surfaces. Further, the larger helix is intended to function as a transport screw to export the dust from the tube surfaces (see Figure 1 and Appendix D).

3.3.2 The Rotating Plate ESP

Based on the problems related to dust removal from the collector plates the writer of the thesis has come up with an idea for an ESP structure. The configuration consists of rotating plate electrodes mounted on a single shaft and a blade system to wipe the accumulated dust from the electrodes (see Fig. 2). The blade system is maintained fixed during the plate rotation. The power of the idea lies in the fact that in theory all the primary collection surfaces are kept clean by intermittent or continuous wiping. For easy maintenance the plate stack and the blade system can be designed in a fashion that they are easily and independently removed for seasonal cleaning or replacement.

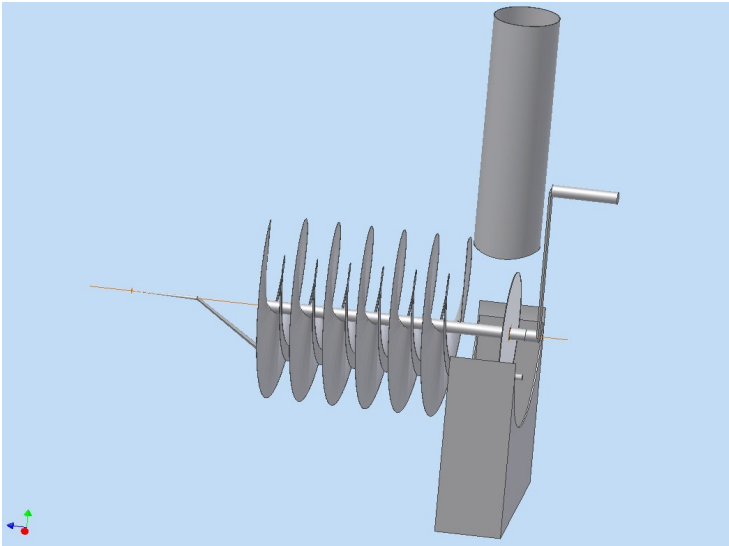

Figure 1: The helicoidal ESP configuration. Cylinder walls omitted. For more information see Appendix D.

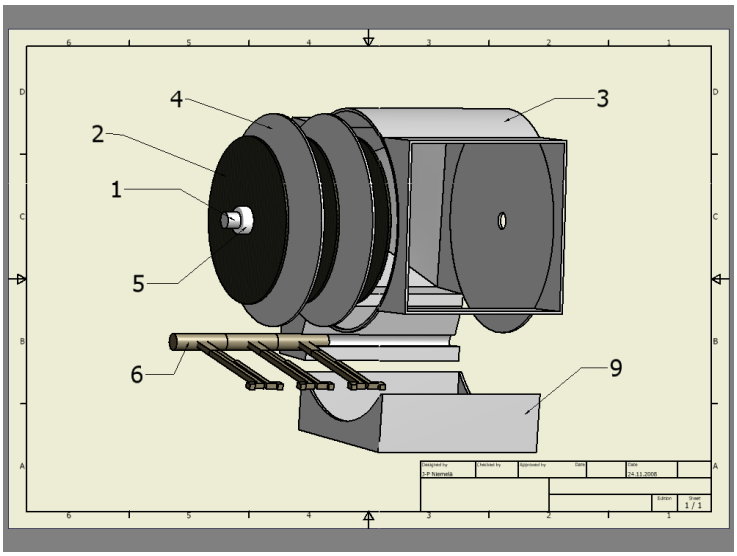

Figure 2: The rotating plate ESP configuration. For more information see Appendix C.

4 Electric Field Equations

Developing a mathematical model for electrostatic precipitators is a real multiphysics challenge. At first one has to define a geometry of a particular precipitator configuration considered, in which both the flue gas flow velocity field and electric field are to be calculated. Once the fields are generated, aerosol physics steps into the picture. Properties of particles suspended in fluid flow has to be known. If interested in grasping a realistic view, particle size statistics must be taken into account, that is justified in the case of wood fuel flue gases, for which the particle size distributions range over multiple orders of magnitude. In this chapter we start discussing the required physics by deriving the equations governing the electric fields in ESPs.

4.1 About Electrostatics

To generate the desired electrical conditions into our ESP geometry, we solve the Poisson equation for electric potential. The required field equations are derived from the very basics to grasp the essential phenomena related. We begin from Gauss' law, Eq. (1), which states that the flux of the electric field out of a closed surface S equals to total charge ρ_{tot} inside a volume V bounded by the surface S, *i.e.*, [6]

$$\int_S \vec{E} \cdot d\vec{S} = \frac{1}{\epsilon_0} \int_V \rho_{tot} dV. \tag{1}$$

Since we seek to formulate our problem as a differential equation, Eq. (1) is transformed by applying the Gauss' divergence theorem for electric field:

$$\int_S \vec{E} \cdot d\vec{S} = \int_V \nabla \cdot \vec{E} dV. \tag{2}$$

Now the integrands at the right hand sides of the equations (1) and (2) must equal yielding the differential form of the Gauss' law:

$$\nabla \cdot \vec{E} = \rho_{tot}/\epsilon_0. \tag{3}$$

Here, by ρ_{tot} we denote the total charge density including any polarization charges. [6]

4.1.1 Polarization

Our task becomes simpler if there is no need to know the polarization charge of the flue gas. Decomposition of the total charge density into the polarization charge density ρ_p and the free or space charge density ρ_s allows us, in the

following derivation, to manipulate the Poisson equation in such a way that only the space charge of a flue gas between the electrodes needs to be known. Therefore, the concept of polarization is discussed in this section.

Polarization is a phenomenon that occurs in an insulator when subjected to external electric field. As a result, the charge distributions of single atoms are distorted, giving arise to electric dipole moments defined as amount of distortion $\vec{a}$ multiplied by the total charge of electrons of the atom in question Ze. The net of the polarization charge density in uniform electric field is zero but at the boundaries of dielectric some surface charge appears, generating the, so called, depolarizing field having direction opposite to that of the external electric field, and thus reducing the net field strength inside the dielectric. To account the global effects of dipole moments, a vector quantity, polarization per unit volume, $\vec{P} = N\vec{p} = NZe\vec{a}$, where N stands for the number of atoms per unit volume, is introduced. [6]

To find out the relationship between polarization per unit volume and polarization charge density, we consider a cube of volume $\delta x \delta y \delta z$, chosen arbitrarily inside an electrically neutral dielectric material subjected to an electric field, allowed at first to vary only in x-direction. The size of the cube is taken big compared atomic scale and small compared to macroscopic characteristic dimension of the dielectric. Now let the polarization per unit volume have a value $\vec{P}(x)$ at the point x and $\vec{P}(x+\delta x)$ at the point $x+\delta x$. Then, by expanding $\vec{P}$ to first order, we obtain the charge entering the cube [6],

$$-\left(\vec{P}(x+\delta x) - \vec{P}(x)\right)\delta y \delta z = -\frac{\partial P_x}{\partial x}\delta x \delta y \delta z.$$

There were nothing particular in the choice of the x-direction for electric field and the above expression can be generalized to include the y and z-components as well. Thus, the total polarization charge acquired by the cube can be written

$$\rho_p dV = \left[-\frac{\partial P_x}{\partial x} - \frac{\partial P_y}{\partial y} - \frac{\partial P_z}{\partial z}\right]\delta x \delta y \delta z = \left[-\nabla \cdot \vec{P}\right] dV,$$

yielding an expression for polarization charge density [6]

$$\rho_p = -\nabla \cdot \vec{P}. \tag{4}$$

Because polarization in dielectrics arises in the presence of an electric field, one would intuitively assume that polarization per unit volume would be proportional to electric field. We can check whether this is so by considering a parallel plate capacitor in vacuum having plate distance d and plate area

A, with the corresponding surface charge q_{surf}. For such a capacitor the capacitance is given by

$$C_0 = \frac{\text{charge}}{\text{potential difference}} = \frac{Aq_{surf}}{E_0 d} = \frac{\epsilon_0 A}{d},$$

since, by applying Gauss' law, Eq. (1), to surface enclosing the capacitor plate, one obtains

$$\begin{aligned}
&\int_S \vec{E} \cdot dS = \frac{1}{\epsilon_0} \int_V q_{surf} dV \\
&\Leftrightarrow EA = \frac{1}{\epsilon_0} q_{surf} A \\
&\Leftrightarrow E = \frac{q_{surf}}{\epsilon_0}.
\end{aligned}$$

If instead of vacuum the capacitor is filled with dielectric material, the polarization charge of magnitude $\vec{P}A$ appears on the surface of the dielectric reducing the total charge density at immediate surroundings of the capacitor plate. Thus, the Gauss' law, Eq. (1), now yields

$$EA = \frac{1}{\epsilon_0} \left(q_{surf} - P \right) A \quad \Leftrightarrow \quad q_{surf} = \epsilon_0 E + P.$$

The depolarizing field in the presence of dielectric increases the capacitance compared to the capacitance in vacuum by the factor ϵ, called *relative permittivity* or *dielectric constant*. Mathematically formulating, one can thus write

$$C = \epsilon C_0 = \epsilon \frac{\epsilon_0 A}{d}. \tag{5}$$

On the other hand, for altered potential difference Ed and charge in the presence of the dielectric, the expression

$$C = \frac{Aq_{surf}}{Ed} = \frac{A}{Ed} \left(\epsilon_0 E + P \right) = \frac{A\epsilon_0}{d} \left(1 + \frac{P}{\epsilon_0 E} \right), \tag{6}$$

is valid. Comparing these two formulas, Eqs. (5) and (6), for capacitance, and generalizing to vector form we get

$$\epsilon = \left(1 + \frac{\vec{P}}{\epsilon_0 \vec{E}} \right).$$

This can be rewritten as follows:

$$\vec{P} = (\epsilon - 1)\,\epsilon_0 \vec{E}. \tag{7}$$

Here $\epsilon - 1 = \chi_E$ is a dimensionless constant of proportionality known as *electric susceptibility.* [6]

4.2 Poisson's Equation

Having introduced an expression for polarization, we are able come back to the derivation of our field equation. We start by writing the total charge density as a sum of the space charge density and the polarization charge density $\rho_{tot} = \rho_s + \rho_p$. Further, by substitution of Eq. (4) for polarization charge density into the Gauss' law, Eq. (1), we obtain

$$\nabla \cdot \vec{E} = (\rho_s + \rho_p)\,\frac{1}{\epsilon_0} \quad \Leftrightarrow \quad \nabla \cdot \vec{E} = \left(\rho_s - \nabla \cdot \vec{P}\right)\frac{1}{\epsilon_0}$$

and, by reorganizing the terms,

$$\nabla \cdot \left(\epsilon_0 \vec{E} + \vec{P}\right) = \rho_s. \tag{8}$$

Since it is practical to set the boundary conditions in terms of voltage, we prefer to write the above Eq. (8) for electric potential, instead of electric field. We recall that a vector field $\vec{E}$ can be written as a gradient of a scalar field, *i.e.*,

$$\vec{E} = -\nabla\phi, \tag{9}$$

using notation ϕ for a scalar electric potential field. Now combining equations (8) and (9)gives the result that

$$-\nabla \cdot \left(\epsilon_0 \nabla\phi - \vec{P}\right) = \rho_s. \tag{10}$$

This is the equation that the Comsol Electrostatics mode solves for potential ϕ. We can assure ourselves that this really is of the conventional form of the Poisson's equation for electric potential, by replacing $\vec{P}$ with Eq. (7), and furthermore, writing the electric field as a gradient of the potential as in Eq. (9):

$$
\begin{aligned}
&-\nabla\cdot\left(\epsilon_0\nabla\phi-\vec{P}\right)=\rho_s\\
&\Leftrightarrow -\nabla\cdot\left(\epsilon_0\nabla\phi-(\epsilon-1)\,\epsilon_0\vec{E}\right)=\rho_s\\
&\Leftrightarrow -\nabla\cdot\left(\epsilon_0\nabla\phi+(\epsilon-1)\,\epsilon_0\nabla\phi\right)=\rho_s\\
&\Leftrightarrow -\nabla\cdot\left(\epsilon\epsilon_0\nabla\phi\right)=\rho_s\\
&\Leftrightarrow -\nabla\cdot\nabla\phi=\frac{\rho_s}{\epsilon\epsilon_0},
\end{aligned}
$$

and recalling the vector identity $\nabla\cdot\nabla f=\nabla^2 f$, we obtain

$$
-\nabla^2\phi=\frac{\rho_s}{\epsilon\epsilon_0}. \tag{11}
$$

This certainly is a form of Poisson's equation, which is what we set out to obtain. Formulating the problem this way for electric potential, does not only have the advantage of straightforward boundary condition setting, but also that, that the necessity of knowing the polarization charge density ρ_p vanishes. Thus, to solve the problem, in addition to boundary conditions, we only need to know the two constants that depend only on the properties of the dielectric in question: the space charge density ρ_s and relative permittivity ϵ. [6]

4.3 Electric Displacement Vector

The phenomena on the surface layer of two materials might be of interest when trying to define the boundary conditions for the Poisson's equation. If the materials have different electrical properties, described by dielectric constants ϵ_1 and ϵ_2, respectively, the normal component of the electric field is not continuous because the flux of electric field is not equal through the opposite sides of closed surface enclosing the boundary layer containing polarization charge surface density. Nevertheless, this problem of discontinuity can be avoided by introducing a vector field called electric displacement, $\vec{D}$.

Once again, we start from the Gauss' law and write the total charge density as a sum of polarization and space charge density, then substituting in Eq. (4), and thus obtaining [6]

$$
\begin{aligned}
&\nabla \cdot \vec{E} = \frac{1}{\epsilon_0}\left(\rho_f + \rho_p\right) \\
&\Leftrightarrow \nabla \cdot \vec{E} = \frac{1}{\epsilon_0}\left(\rho_f - \nabla \cdot \vec{P}\right) \\
&\Leftrightarrow \nabla \cdot \left(\epsilon_0 \vec{E}\right) + \nabla \cdot \vec{P} = \rho_f \\
&\Leftrightarrow \nabla \cdot \left(\epsilon_0 \vec{E} + \vec{P}\right) = \rho_p.
\end{aligned}
$$

Now, by applying notation $\epsilon_0 \vec{E} + \vec{P} = \vec{D}$, we can write

$$\nabla \cdot \vec{D} = \rho_f. \tag{12}$$

By applying the Gauss' Divergence Theorem that is valid for any vector field, and the above Eq. (12), we obtain

$$\int_S \vec{D} \cdot dS = \int_V \nabla \cdot \vec{D} dV = \int_V \rho_f dV. \tag{13}$$

Because it is polarization charge density, not space charge density, that is present at the surface layer between two dielectric materials, the equation (13) yields

$$\vec{D}_1 \cdot \delta\vec{S}_1 + \vec{D}_2 \cdot \delta\vec{S}_2 = 0, \tag{14}$$

which is identical to

$$D_{1normal} = D_{2normal}. \tag{15}$$

The above equation (15) states that the normal component for electric displacement vector is continuous at the boundary of two dielectric materials. The problem of discontinuity of the electric field vector is thus solved. [6]

4.4 Boundary Conditions for the Poisson Equation

In an ESP setup the particulates are deviated with electric field generated by voltage applied. At the surface of the electrodes the electric potential boundary condition $\phi = \phi_0$ is used, whereas for flue gas inlet and outlet boundaries we apply zero charge boundary condition $\vec{n} \cdot \vec{D} = 0$, which specifies that the normal component of the electric displacement is zero. [3]

5 Flow Velocity Field Equations

Having derived the equation governing the electric field related phenomena, the Poisson's equation for electric potential (11), we are ready to discuss the concepts and problematics related to the fluid flow fields.

5.1 About Fluid Kinematics

In order to properly understand the equation of motion for fluids, in our case the Navier-Stokes equation for incompressible ones, it is necessary go back to fundamentals and follow the derivation step by step introducing concepts needed to be able to take the simplifying assumptions. Equation of motion will be written in terms of components of force, therefore involving dynamics. However, we start our derivation considering the effects of forces, *i.e.*, strains, and discuss about fluid kinematics.

Fluid particle is defined as an element of fluid of volume V_f characterized by it's size $a_f = V_f^{1/3}$. To be able to treat fluid as a continuous medium a_f must be very large relative to the mean free path of fluid λ and very small relative to the characteristic length L of the flow field geometry in question, *i.e.*, a_f must satisfy: $\lambda << a_f << L$. If $L \longrightarrow \lambda$ the problem to be solved reduces back to simple mechanics of colliding bodies. Approximating flue gas of wood combustion as air, mean free path around 0.1 μm can be assumed. For electrostatic precipitator geometries used, the characteristic length varies from few centimeters to about 10 cm implying that the continuity assumption is valid and safe. Under continuity assumption velocity of a fluid particle is defined as average velocity of the molecules inside the fluid particle. Fluid particle velocity is then independent of a_f, since $\lambda << a_f$. [4]

Velocity field $\vec{u}$ is defined by velocities of a set of fluid particles. When velocity fields are described distinction between Eulerian and Lagrangian approaches has to be made. In the Eulerian description a fixed fluid particle with a position vector $\vec{r}$ is considered. Thus at different instants of time, velocity $\vec{U} = \vec{U}(\vec{r}, t)$ describes the velocity of different fluid particle. When observer moves with the fluid particle we talk about Lagrangian description of fluid motion, thus the position vector of a fluid particle is also a function of time $\vec{r} = \vec{r}(t)$ and the related velocity field is written $\vec{u} = \vec{u}(\vec{r}(t), t)$, where $\vec{u}$ stands for the Lagrangian velocity to point out the distinction to capitalized Eulerian velocity $\vec{U}$. [4]

5.1.1 Acceleration Corresponding to a Velocity Field

Acceleration of a fluid particle can be derived considering a fluid particle in a position $\vec{r}_1$ at an instant of time t_1 which at slightly later instant of time $t_2 = t_1 + \delta t$ is found in position $\vec{r}_2 = \vec{r}_1 + \vec{u}\left(\vec{r}_1, t\right)\delta t + O\left(\delta t^2\right)$. Thus, the change in velocity $\delta\vec{u}$ can be expanded to first order [4]

$$\delta\vec{u} = \vec{u}\left(\vec{r}_2, t_2\right) - \vec{u}\left(\vec{r}_1, t_1\right) = \frac{\partial\vec{u}}{\partial t}\delta t + \frac{\partial\vec{u}}{\partial x}\delta x + \frac{\partial\vec{u}}{\partial y}\delta y + \frac{\partial\vec{u}}{\partial z}\delta z,$$

and further, taking the time derivative [4]

$$\begin{aligned}
\frac{d\vec{u}}{dt} &= \lim_{\delta t\to 0}\frac{\delta\vec{u}}{\delta t} \\
&= \lim_{\delta t\to 0}\left(\frac{\partial\vec{u}}{\partial t} + \frac{\partial\vec{u}}{\partial x}\frac{\delta x}{\delta t} + \frac{\partial\vec{u}}{\partial y}\frac{\delta y}{\delta t} + \frac{\partial\vec{u}}{\partial z}\frac{\delta z}{\delta t}\right) \\
&= \frac{\partial\vec{u}}{\partial t} + u_x\frac{\partial\vec{u}}{\partial x} + u_y\frac{\partial\vec{u}}{\partial y} + u_z\frac{\partial\vec{u}}{\partial z},
\end{aligned}$$

we obtain in vector form [4]

$$\frac{d\vec{u}}{dt} = \frac{\partial\vec{u}}{\partial t} + \left(\vec{u}\cdot\nabla\right)\vec{u}. \tag{16}$$

In equation (16), also known as the total derivative or convective derivative, the first term on the right hand side gives the change with respect to time and the second describes fluid particles acceleration due to it's position in a velocity field [4]. For stationary flow, such as is assumed in this paper, $\frac{\partial\vec{u}}{\partial t} = 0$, and equation (16) for convective derivative reduces to [4]

$$\frac{d\vec{u}}{dt} = \left(\vec{u}\cdot\nabla\right)\vec{u}. \tag{17}$$

5.1.2 The Equation of Continuity, i.e., A Local Equation for Conservation of Mass

Considering a mass balance inside a fixed volume we can write a local equation for conservation of mass, *i.e.*, the equation of continuity. If taking an arbitrary volume V to be bounded by a closed surface S and allowing fluid to freely traverse the volume, the rate of change of mass the volume contains is equal and opposite to the flux leaving the surface (see Figure 3). Therefore, mathematical formulation yields

$$\frac{dm}{dt} = \frac{d}{dt}\int_V \rho dV = -\int_S \rho\vec{u}\cdot\vec{n}dS, \tag{18}$$

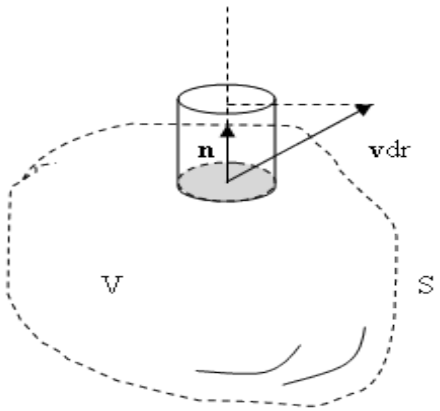

Figure 3: Mass balance of an arbitrary volume V bounded by closed surface S.

where $\vec{n}$ is outward normal vector of surface element dS. Now, applying the Gauss' divergence theorem

$$\int_S \vec{F} \cdot \vec{n} dS = \int_V \nabla \cdot \vec{F} dV, \tag{19}$$

to the right hand side term of equation (18) we obtain

$$\int_V \left[\frac{\partial \rho}{\partial t} + \nabla \cdot (\rho \vec{u}) \right] dV = 0,$$

for which the integrand must vanish for equality to hold, thus implying

$$\frac{\partial \rho}{\partial t} + \nabla \cdot (\rho \vec{u}) = 0. \tag{20}$$

Keeping in mind our purposes to model stationary flows with constant fluid density, we can write

$$\begin{aligned} &\frac{\partial \rho}{\partial t} + \nabla \cdot (\rho \vec{u}) = 0 \\ &\Leftrightarrow \frac{\partial \rho}{\partial t} + \rho \nabla \cdot \vec{u} + \vec{u} \cdot \nabla \rho = 0 \\ &\Rightarrow 0 + \rho \nabla \cdot \vec{u} + 0 = 0, \end{aligned}$$

finally obtaining the continuity equation,

$$\nabla \cdot \vec{u} = 0 \tag{21}$$

for incompressible flow. Above equation (21) states that divergence of a vector field $\vec{u}$ is zero, i.e., there is neither sources nor sinks inside the velocity field [4]. This is reasonable from the point of view of ESPs, since flow channels with well defined boundary inlets and outlets are studied. [4]

A rule of thumb for determining whether a fluid flow can be considered incompressible can be represented as inequality

$$U << U_s, \tag{22}$$

where U is a characteristic speed of the flow and U_s represents the speed of sound in a fluid considered [4]. In small-scale electrostatic precipitators the flow velocities should remain below 5 m/s and approximating the flue gas by air at NTP the inequality holds: $U << U_s \Leftrightarrow 5\ m/s << 343\ m/s$.

5.1.3 Velocity Gradient Tensor

In this section the strains in fluids are discussed by formulating an expression for the velocity gradient tensor. We start by considering two adjacent fluid particles located at points $\vec{r}$ and $\vec{r} + \vec{dr}$ with corresponding velocities $\vec{u}(\vec{r}, t)$ and $\vec{u} + \vec{du}$. Expanding the components du_i to first order, we obtain

$$du_i = \sum_{j=1}^{3} \left(\frac{\partial u_i}{\partial x_j} \right) dx_j. \tag{23}$$

In three dimensions, ordering for all $i = 1, 2, 3$ equations (23), as a group of equations and using matrix formalism, the quantities $\partial u_i / \partial x_j = g_{ij}$ are the elements of a second rank tensor forming a 3×3 square matrix [4]

$$[G] = \begin{bmatrix} \frac{\partial u_1}{\partial x_1} & \frac{\partial u_1}{\partial x_2} & \frac{\partial u_1}{\partial x_3} \\ \frac{\partial u_2}{\partial x_1} & \frac{\partial u_2}{\partial x_2} & \frac{\partial u_2}{\partial x_3} \\ \frac{\partial u_3}{\partial x_1} & \frac{\partial u_3}{\partial x_2} & \frac{\partial u_3}{\partial x_3} \end{bmatrix}. \tag{24}$$

Every real square matrix $[A]$ can be written as a sum of symmetric and antisymmetric matrix as follows [5]:

$$\begin{aligned} [A] &= \frac{1}{2}\left([A] + [A]^T\right) + \frac{1}{2}\left([A] - [A]^T\right) \\ \Rightarrow a_{ij} &= \frac{1}{2}\left(a_{ij} + a_{ji}\right) + \frac{1}{2}\left(a_{ij} - a_{ji}\right). \end{aligned}$$

For components of velocity gradient tensor the decomposition yields

$$
\begin{aligned}
&[G] = \frac{1}{2}\left([G] + [G]^T\right) + \frac{1}{2}\left([G] - [G]^T\right) \\
&\Rightarrow g_{ij} = \underbrace{\frac{1}{2}\left(\frac{\partial u_i}{\partial x_j} + \frac{\partial u_j}{\partial x_i}\right)}_{e_{ij}=symmetric} + \underbrace{\frac{1}{2}\left(\frac{\partial u_i}{\partial x_j} - \frac{\partial u_j}{\partial x_i}\right)}_{\omega_{ij}=antisymmetric} \\
&\Leftrightarrow g_{ij} = e_{ij} + \omega_{ij},
\end{aligned}
\tag{25}
$$

where $[G]^T$ is the transpose of $[G]$. The symmetric component e_{ij} of the velocity gradient tensor g_{ij} corresponds to deformations of a fluid element and antisymmetric term ω_{ij} describes its rotation. The diagonal elements e_{ll} of the symmetric term e_{ij} characterize the change in volume of a fluid particle. Further decomposition of the symmetric term as

$$
e_{ij} = \frac{1}{3}\delta_{ij}e_{ll} + \left[e_{ij} - \frac{1}{3}\delta_{ij}e_{ll}\right] = t_{ij} + d_{ij}, \tag{26}
$$

allows us to separate the deformations associated with volume dilations described by the diagonal tensor t_{ij} and deformations not related to change of volume characterized by the deviator tensor d_{ij}. By symbol δ_{ij} the Kronecker delta, being 1 if $i = j$ and 0 if $i \neq j$, is noted. Therefore, a component of the velocity gradient tensor can expressed as

$$
g_{ij} = t_{ij} + d_{ij} + \omega_{ij}. \tag{27}
$$

where then $t_{ij} = 0$ for incompressible flow. [4]

5.2 About Fluid Dynamics

In the previous section we derived an expression for strains in fluids in terms of the velocity gradient tensor. Strains, that is, deformations and solid body rotations of a fluid element, are caused by stresses. Stress is defined as force per unit area.

5.2.1 The Stress Tensor

If considering a surface element dS of fluid in rest, only forces normal to the element, that correspond to the conventional hydrostatic pressure, are present. Nevertheless, fluid motion gives a rise to forces tangential to the surface element due to viscosity. [4]

Let us now write an expression for the stress $\sigma_{\hat{n}}$ on an arbitrary surface dS with an unit normal vector $\hat{n} = (n_x, n_y, n_z)$. To do this we consider forces exerted on three, x-, y- and z-directed, edges of a tetrahedron with corresponding lengths dx, dy and dz, respectively (see Figure 4). The force $\vec{df}$ exerted on the surface dS spanned by $\vec{dx}$, $\vec{dy}$ and $\vec{dz}$ is divided to components $\sigma_{x\hat{n}}$, $\sigma_{y\hat{n}}$ and $\sigma_{z\hat{n}}$. By writing the force balance, for example, in x-direction we determine $\sigma_{x\hat{n}}$. The x-components of stress force on faces perpendicular to coordinate axes are

$$\begin{aligned} &(-\sigma_{xx}n_x)dS, \\ &(-\sigma_{xy}n_y)dS \quad \text{and} \\ &(-\sigma_{xz}n_z)dS, \end{aligned}$$

where the negative signs represent the opposite direction to the coordinate axes of the outward direction normal vectors of the faces. Thus, the net of all the x-directed stresses on the tetrahedron is

$$(\sigma_{x\hat{n}} - \sigma_{xx}n_x - \sigma_{xy}n_y - \sigma_{xz}n_z)dS.$$

Then, including the x-component of any volume force f_x per unit volume, Newton´s second law implies

$$(\sigma_{x\hat{n}} - \sigma_{xx}n_x - \sigma_{xy}n_y - \sigma_{xz}n_z)dS + f_x dV = \rho_f dV \frac{d^2x}{dt^2}.$$

Now, if $dV \to 0$, the two terms including dV do vanish. The dS-terms though remain, since dV approaches zero as $dS^{3/2}$. Therefore, equation (28) gives

$$\sigma_{x\hat{n}} = \sigma_{xx}n_x + \sigma_{xy}n_y + \sigma_{xz}n_z. \tag{28}$$

By cyclic permutation of the indexes it is possible to write expressions equal to Eq. (28) for $\sigma_{y\hat{n}}$ and $\sigma_{y\hat{n}}$ as well. Then, using matrix formalism to write the group of equations formed, we obtain

$$\begin{pmatrix} \sigma_{x\hat{n}} \\ \sigma_{y\hat{n}} \\ \sigma_{z\hat{n}} \end{pmatrix} = \begin{pmatrix} \sigma_{xx} & \sigma_{xy} & \sigma_{xz} \\ \sigma_{yx} & \sigma_{yy} & \sigma_{xz} \\ \sigma_{zx} & \sigma_{zy} & \sigma_{zz} \end{pmatrix} \begin{pmatrix} n_x \\ n_y \\ n_z \end{pmatrix}, \tag{29}$$

or more compactly,

$$\vec{\sigma}_{\hat{n}} = [\sigma] \cdot \hat{n}, \tag{30}$$

where $[\sigma]$ is the so called stress tensor. [4]

As for the strain tensor in the previous chapter, it is again reasonable to perform the decomposition to tensors having only diagonal or non-diagonal elements, respectively. The diagonal elements, i.e., the normal components of associated stress vectors correspond to familiar hydrostatic pressure. Therefore, we write

$$\sigma_{ij} = \sigma'_{ij} - p\delta_{ij},$$

where p is the hydrostatic pressure and δ_{ij} is the Kronecker delta. Negative sign of the pressure term indicates the compressive direction of hydrostatic pressure in fluids being opposite to outward normal direction. The symmetric tensor $\sigma'_{ij} = \sigma'_{ji}$ is related to strains of fluid elements and is generally called viscosity stress tensor, which is a function of symmetric part of the strain tensor e_{ij} defined in previous section(see equation (27)). For Newtonian fluids the dependence is linear, and can be expressed as

$$\sigma'_{ij} = 2Ae_{ij} + B\delta_{ij}e_{ll}.$$

Using the expression (26) used for e_{ij}, this can be equivalently written as

$$\sigma'_{ij} = \eta\left(2e_{ij} - \frac{2}{3}\delta_{ij}e_{ll}\right) + \xi(\delta_{ij}e_{ll}), \tag{31}$$

where η and ξ are the dynamic viscosity and the so called second viscosity, i.e., bulk viscosity, respectively. Now, because the diagonal components e_{ll} correspond to volume dilations, equation (31) reduces for incompressible fluids as [4]

$$\sigma'_{ij} = 2\eta e_{ij}. \tag{32}$$

This expression (32) of the viscosity stress tensor provides us the means to take the incompressibility assumption needed in the next section when formulating the equation of motion for stationary incompressible flow. [4]

5.3 The Navier-Stokes Equation

Using Newton's second law we equate both surface and volume forces to the rate of change of momentum of a volume of fluid V, which is made up of a given amount of matter remaining inside the volume, and moving along with the fluid. Mathematically formulating we write

$$\frac{d}{dt}\left(\int_V \rho_f \vec{u} dV\right) = \int_V \rho_f \vec{f} dV + \int_S [\sigma] \cdot \vec{n} dS. \tag{33}$$

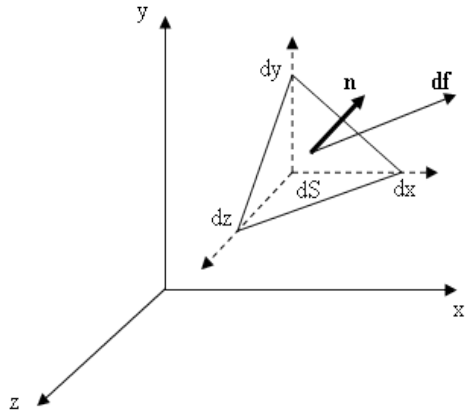

Figure 4: An arbitrary surface dS spanned by vectors $\vec{dx}$, $\vec{dy}$ and $\vec{dz}$.

The product $\rho_f dV$ represents the mass of the fluid element which is by definition constant for any element of fluid, because the matter inside the closed volume V can not cross the boundary enclosing it. Therefore, taking the time derivative only of the velocity in the integrand of the first term of Eq. (33) is sufficient. Furthermore, the second term on the right hand side in Eq. (33) can be transformed into a volume integral by applying the Gauss' divergence theorem, Eq. (19). Consequently we obtain

$$\int_V \rho_f \frac{d\vec{u}}{dt} dV = \int_V \rho_f \vec{f} dV + \int_V \nabla \cdot [\sigma] dV$$
$$\Leftrightarrow \int_V \left(\rho_f \frac{d\vec{u}}{dt} - \rho_f \vec{f} - \nabla \cdot [\sigma] \right) dV = 0,$$

for which the integrand must vanish, yielding

$$\rho_f \frac{d\vec{u}}{dt} = \rho_f \vec{f} + \nabla \cdot [\sigma]. \tag{34}$$

Then, using the familiar separation of the stress tensor, Eq. (31), to the terms corresponding to the viscous and pressure forces, Eq. (34) reforms as

$$\rho_f \frac{d\vec{u}}{dt} = \rho_f \vec{f} + \nabla \cdot [\sigma'] - \nabla p, \tag{35}$$

since

$$\nabla \cdot p\delta_{ij} = \left(\frac{\partial}{\partial x}, \frac{\partial}{\partial y}, \frac{\partial}{\partial z}\right) \begin{pmatrix} p & 0 & 0 \\ 0 & p & 0 \\ 0 & 0 & p \end{pmatrix} = \left(\frac{\partial p}{\partial x}, \frac{\partial p}{\partial y}, \frac{\partial p}{\partial z}\right) = \nabla p.$$

In the first term of Eq. (35) we have the total or convective derivative which can be decomposed as we did in Section 5.1.1:

$$\rho_f \frac{\partial \vec{u}}{\partial t} + \rho_f \left(\vec{u} \cdot \nabla\right) \vec{u} = \rho_f \vec{f} + \nabla \cdot [\sigma'] - \nabla p. \tag{36}$$

This is the general equation of motion for any fluid since no assumptions on the form of stress tensor have been taken. [4]

We are though seeking to find an equation to describe the motion of incompressible Newtonian fluid, because incompressibility assumption was, in Section 5.1.2, pointed out to be a safe and justified. To approximate fluid flow as Newtonian in Section 5.2.1 we assumed linear dependence between the viscous tress tensor and the strains (see Eqs. (31)-(32)). Now, substituting the viscous stress tensor in the above equation (36) with Eq. (31) we obtain for i^{th} component

$$\{\nabla \cdot [\sigma']\}_i = \frac{\partial \sigma'_{ij}}{\partial x_j} = \eta \frac{\partial^2 u_i}{\partial x_j \partial x_i} + \left(\xi + \frac{\eta}{3}\right) \frac{\partial}{\partial x_i} \left(\frac{\partial u_l}{\partial x_l}\right),$$

which gives in vector form

$$\nabla \cdot [\sigma'] = \eta \nabla^2 \vec{u} + \left(\xi + \frac{\eta}{3}\right) \nabla \left(\nabla \cdot \vec{u}\right).$$

For incompressible flows the continuity condition, Eq. (21), implies $\nabla \cdot \vec{u} = 0$, and thus we are allowed to write

$$\nabla \cdot [\sigma'] = \eta \nabla^2 \vec{u},$$

and equation of motion for Newtonian incompressible fluids, called the Navier-Stokes equation, is finally obtained [4]

$$\rho_f \frac{\partial \vec{u}}{\partial t} + \rho_f \left(\vec{u} \cdot \nabla\right) \vec{u} = \rho_f \vec{f} - \nabla p + \eta \nabla^2 \vec{u}. \tag{37}$$

This is the equation of motion for fluids employed in all the simulations performed in this paper.

5.4 Boundary conditions for the Navier-Stokes Equation

To describe the boundary phenomena in an ESP we have to set three type of conditions: the inlet, the outlet and the solid stationary wall boundary.

The solid wall case is very straightforward. Fluid can not penetrate into a solid, thus implying that at the boundary layer the normal components of the solid and the fluid velocity must equal [4]:

$$\vec{u}_{solid} \cdot \vec{n} = \vec{u}_{fluid} \cdot \vec{n}. \tag{38}$$

For real fluids, i.e., for fluids with viscosity, tangential slipping would result infinite energy dissipation. This leads to the fact that the tangential components of the velocities of the fluid and the boundary must also equal [4]:

$$\vec{u}_{solid} \cdot \vec{\tau} = \vec{u}_{fluid} \cdot \vec{\tau}. \tag{39}$$

Now Eqs. (38) and (39) are satisfied only for equal velocities for a solid and a fluid [4]

$$\vec{u}_{solid} = \vec{u}_{fluid}.$$

In an ESP the solid boundary walls will not move resulting zero fluid velocity at the boundary wall

$$\vec{u}_{fluid} = 0. \tag{40}$$

Eq. (40) is frequently referred to as the no-slip boundary condition at the solid wall.

At the inlet we apply either normal flow condition or a parabolic flow profile anticipating the form of the profile caused by zero velocity at wall surfaces. The parabolic profile is discussed in more detail in Section 6.3.

At the outlet we assume normal stress combined with normal velocity condition. Let us take the outlet boundary to be described by its outward direction normal vector $\hat{n}$. Thus, the normal stress requirement can be taken into account projecting all the stress forces at the boundary to the negative direction of boundary normal vector $-\hat{n}$. We can therefore start from Eq. (30), the expression for $\hat{n}$ directed stress, including the general expression for the stress tensor $[\sigma]$:

$$\vec{\sigma}_{\hat{n}} = [\sigma] \cdot \hat{n}. \tag{41}$$

As mentioned previously, and expressed in Eq. (31), the stress tensor components σ_{ij} can be decomposed as

$$\sigma_{ij} = \sigma'_{ij} - p\delta_{ij}. \tag{42}$$

For incompressible Newtonian fluid the symmetric tensor σ'_{ij} can be written combining Eqs. (32) and (25)

$$\sigma'_{ij} = 2\eta e_{ij} = \eta \left(\frac{\partial u_i}{\partial x_j} + \frac{\partial u_j}{\partial x_i} \right). \tag{43}$$

Therefore for the components of the stress tensor, by applying Eqs. (42) and (43), it is possible to write

$$\sigma_{ij} = \eta \left(\frac{\partial u_i}{\partial x_j} + \frac{\partial u_j}{\partial x_i} \right) - p\delta_{ij}. \tag{44}$$

The $-\hat{n}$-directed stress $-\vec{\sigma}_{\hat{n}}$ can then be expressed as

$$\left\{ -\eta \begin{pmatrix} \frac{\partial u_1}{\partial x_1} & \frac{\partial u_1}{\partial x_2} & \frac{\partial u_1}{\partial x_3} \\ \frac{\partial u_2}{\partial x_1} & \frac{\partial u_2}{\partial x_2} & \frac{\partial u_2}{\partial x_3} \\ \frac{\partial u_3}{\partial x_1} & \frac{\partial u_3}{\partial x_2} & \frac{\partial u_3}{\partial x_3} \end{pmatrix} - \eta \begin{pmatrix} \frac{\partial u_1}{\partial x_1} & \frac{\partial u_2}{\partial x_1} & \frac{\partial u_3}{\partial x_1} \\ \frac{\partial u_1}{\partial x_2} & \frac{\partial u_2}{\partial x_2} & \frac{\partial u_3}{\partial x_2} \\ \frac{\partial u_1}{\partial x_3} & \frac{\partial u_2}{\partial x_3} & \frac{\partial u_3}{\partial x_3} \end{pmatrix} + \begin{pmatrix} p & 0 & 0 \\ 0 & p & 0 \\ 0 & 0 & p \end{pmatrix} \right\} \cdot \begin{pmatrix} n_1 \\ n_2 \\ n_3 \end{pmatrix},$$

which reduces to

$$-\eta \begin{pmatrix} \nabla u_1 \\ \nabla u_2 \\ \nabla u_3 \end{pmatrix} \cdot \begin{pmatrix} n_1 \\ n_2 \\ n_3 \end{pmatrix} - \eta \begin{pmatrix} \nabla u_1 & \nabla u_2 & \nabla u_3 \end{pmatrix} \cdot \begin{pmatrix} n_1 \\ n_2 \\ n_3 \end{pmatrix} + \begin{pmatrix} p & 0 & 0 \\ 0 & p & 0 \\ 0 & 0 & p \end{pmatrix} \cdot \begin{pmatrix} n_1 \\ n_2 \\ n_3 \end{pmatrix}.$$

Further, since taking gradient of a scalar components s_i of a vector function s is a linear operation $\nabla s = \nabla (s_1, s_2, s_2) = (\nabla s_1, \nabla s_2, \nabla s_2)$, we obtain

$$-\vec{\sigma}_{\hat{n}} = -2\eta \nabla u \cdot \hat{n} + p \cdot \hat{n}. \tag{45}$$

Now, the first term on the right hand side of the Eq. (45) includes an alternative expression for $\hat{n}$-directional derivative of the function $\vec{u}$, provided that the partial derivatives exist and are continuous at all the points of the boundary. In addition, since hydrostatic pressure p is a scalar quantity having a scalar value at a given point, we formulate the normal stress condition at the boundary

$$\vec{\sigma}_{\hat{n}} = p - 2\eta \frac{\partial u}{\partial n}. \tag{46}$$

And if combined with normal velocity condition, $u \cdot \tau = 0$, followed by notation $u =: u_n$, Eq. (46) can be written, to obtain the same form as in Comsol's boundary setting mode,

$$\vec{\sigma}_{\hat{n}} = p - 2\eta \frac{\partial u_n}{\partial n}. \tag{47}$$

This implies, for example, for laminar flow in xy-plane through y-directed outlet, and for constant x-directed mean flow velocity $V_{mean}$and zero pressure applied at the boundary

$$\vec{\sigma}_{\hat{n}} = p - 2\eta \frac{\partial u_n}{\partial n} = p - 2\eta \frac{\partial V_{mean}}{\partial x} = 0 - 0 = 0.$$

6 Fluid Properties of Flue Gas of Wood Combustion

6.1 Viscosity

Viscosity η is the constant of proportionality relating the shear stress and shear strain, frequently referred also as to fluid friction. Alternatively viscosity can be understood as the coefficient describing the transfer of momentum from regions of higher velocity to those of lower velocity [4]. Viscosity is relatively independent of pressure, suggesting that underpressure in a flue pipe has no impact on it [1]. However, the temperature dependence of viscosity has importance, and for an ideal gas it can be described with [11][1]

$$\eta = \eta_r \frac{T_r + S}{T + S} \left(\frac{T}{T_r} \right)^{3/2}, \tag{48}$$

where η_r, S and T_r are the reference viscosity, the Sutherland interpolation constant and the reference temperature, respectively. For pure air, $\eta_r = 18.203 \cdot 10^{-6}\ Pa \cdot s$ at $T_r = 293.15\ K$, whereas Sutherland constant equals to 110.4 K, provided that temperature lies between 80 and 2000 K. For flue gases of small-scale wood combustion, temperatures usually remain well below 473 K. To depict the dependence, in Figure 5 viscosity is plotted as a function of temperature, pointing out the fact that the temperature rise from room temperature up to 500 K is followed by approximate viscosity increase of 56 %, that indeed, has to be taken into account. According to Ref. [1] for the densest produceable smokes the pure air assumption, compared to the two-phase consideration of an aerosol, only yields an error of 0.025 %. Thus, in this paper, it is sufficient to take the pure air assumption, and further, in the following sections, viscosity $2.3069 \cdot 10^{-5}\ Pa \cdot s$ corresponding to temperature of $403.15\ K = 130\ ^oC$, obtained from Minidust measurements, is assumed.

6.2 The Reynolds Number

To estimate the nature of a flow, in a tube or around an obstacle such as an aerosol particle, is usually of interest. Widely used tool for predicting whether the flow is laminar or turbulent is the dimensionless Reynolds number. It

[1] Ref. [11] refers to "K. Willike and P. Baron, *Aerosol Measurements - Principles, techniques and applications*, New York: John Wiley & Sons, 1993." as the source of the Eq. (48).

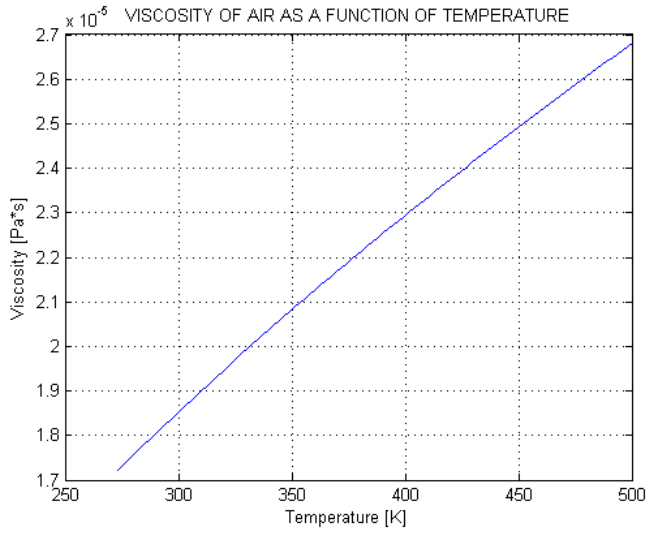

Figure 5: Temperature dependence of viscosity of air suggested by equation (48).

is the ratio of inertial forces to frictional ones acting on each element of the fluid [1]:

$$Re = \frac{F_I}{F_f} = \frac{\rho U L}{\eta}. \tag{49}$$

From the above equation (49) it is essential to notice that Reynolds number increases with increasing flow velocity and decreases with growing viscosity. As pointed out in Figure 5, viscosity of a fluid depends on its temperature, implying that increase in temperature causes Reynolds number to drop. For a flow in a pipe $Re < 2000$ indicates laminar flow, whereas $Re > 4000$ predicts flow to be turbulent [1].

The effects of temperature and flow velocity changes on Reynolds number are illustrated in Figure 6. Temperature was used as a parameter with values 20, 130 and 200 ^oC, respectively. Dimension characteristic to flow tube was fixed to 0.05 m, equal to probable plate distance in rotating plate precipitator and slightly reduced pressure 100 kPa was applied. Taking a look at Figure 6 an important conclusion can be drawn, that is, for air flow at 130 ^oC, below flow velocities of approximately 1.36 m/s, laminar behavior is expected. Thus, if possible, it would be wise to remain below the limit of 1.36 m/s in order to maintain easier predictability of the flow.

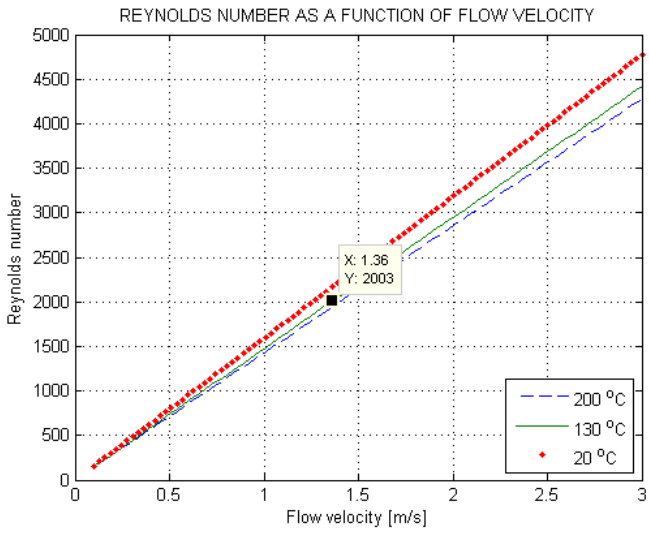

Figure 6: Reynolds number as a function of velocity of the flow at room temperature 20 ^oC, at probable ESP temperature 130 ^oC and at possible upper limit of 200 ^oC.

6.3 Flow Velocity Profile And Analysis Of The Nature Of The Flow Based on Reynolds Number

The fact that the flow velocity of a fluid at the collector plate surface equals to the plate velocity, that is, zero, implies a somewhat parabolic velocity profile for laminar, low Reynolds number flows. Our modeling tool, Comsol 3.4, provides an in-built parabolic velocity profile in its Incompressible Navier-Stokes mode, requiring mean velocity as an input. The profile is of the following form [3]:

$$u_{x,in}(y) = u_{mean} 6s(1-s), \tag{50}$$

with s as a linear scaling factor:

$$s = \frac{y - y_1}{y_2 - y_1}, \tag{51}$$

where y_1 and y_2 correspond to the coordinates of the edge points of the calculation domain's fluid flow inlet. This profile for the flow velocity, Eq. (50), as expected, fulfills the no slip boundary condition, $u_x(y_1) = u_x(y_2) = 0$, for fixed collector plates:

$$s(y = y_1) = \frac{y_1 - y_1}{y_2 - y_1} = 0 \Rightarrow u_x(y_1) = 0$$
$$s(y = y_2) = \frac{y_2 - y_1}{y_2 - y_1} = 1 \Rightarrow 1 - s = 0 \Rightarrow u_x(y_2) = 0.$$

In the MiniDust measurements, for a 20 kW pellet burner, flue gas volume flow $\frac{dV}{dt}$ was observed to be approximately 170 $l/min = 0.01166\ m^3/s$. If the fluid velocity has only the x-component, perpendicular to cross sectional area A of the flow channel, we can write

$$\frac{dV}{dt} = \frac{dx}{dt}A \quad \Rightarrow \quad \frac{dx}{dt} = \frac{\frac{dV}{dt}}{A}.$$

Therefore, assuming rectangular flow channel shape, for precipitator of feasible size with cross sectional area $A = (0.30 \times 0.30)\, m^2$, can be written as

$$\frac{dx}{dt} = \frac{0.01166\ m^3/s}{(0.30 \times 0.30)\ \ m^2} = 0.129556\ m/s = u_{mean} =: u_x.$$

For velocity profile in Eq. (50) symmetrical with respect to x-axis, i.e., for plate type ESP with plates positioned at y_1 and $y_2 = -y_1$ parallel to x-axis, flow velocity experiences its maximum at $y = 0$. Then, $u_x(y)_{max} = u_x(0)$ implies

$$s = \frac{y - y_1}{y_2 - y_1} = \frac{0 - y_1}{-2y_1} = \frac{1}{2},$$

and consequently

$$u_x(y)_{max} = u_x(0) = \frac{3}{2}U_x.$$

In our particular case, the maximum velocity would then be

$$u_x(y)_{max} = u_x(0) = \frac{3}{2}u_x = \frac{3}{2}0.129556\ m/s = 0.194333\ m/s.$$

Velocity of 0.19 m/s yields, as can also be seen from the Figure 6, Reynolds number safely below the limit of 2000, that is, $Re \approx 360$. The cross sectional area of the flow channel for helicoidal configuration can be approximated to be around $0.10 \times 0.15\ m^2$, for 0.15 m outer radius, 0.10 m corresponding to characteristic dimension of the flow channel. Thus, following similar procedure as above, one obtains for maximum velocity in helicoidal flow channel: 1.17 m/s. This gives $Re \approx 4400$, which is even above the turbulence limit $Re = 4000$.

To conclude, we note that in the helicoidal precipitator the channel length gained, is compensated with reduced cross sectional area leading to turbulent flow, and thus more chaotic operating conditions, whereas for rotating plate precipitator the flow velocity remains well below the turbulence limit implying more steady conditions. Furthermore, it would be intuitive that less turbulent flow with lower velocity would cause less re-entrainment. This would be an argument in favor of the rotating plate ESP.

6.4 The Mean Free Path Of A Gas

In the sections describing fluid kinematics and fluid dynamics it was pointed out that gases can be safely treated as continuum relative to characteristic dimension of the flow channels of any ESP. Nevertheless, when one needs to study migration of fine and ultra-fine particles suspended in gas, the continuum hypothesis is no longer self-evident. When the size of small particles approaches the distance between adjacent gas molecules, gas must be considered as a collection of rapidly moving molecules randomly colliding with the particles. This is described with the concept of mean free path, defined as the average distance traveled by a molecule between successive molecule-molecule collisions. It can be expressed as [1]

$$\lambda = \frac{1}{\sqrt{2}\pi n d_m^2}, \tag{52}$$

where n and d_m are molecular concentration with units $1/m^3$ and the collision diameter of the molecule, defined as the distance between the centers of two molecules at the instant of collision, respectively. For air the collision diameter is 3.7Å. Furthermore, for air, molecular concentration can be calculated dividing Avogadro's number N_A by the molar volume of air V_m, which is a function of temperature in a process with negligible pressure drop. Thus, to include temperature as a parameter, the ideal gas law is employed reformulating equation (52) for the mean free path:

$$\lambda = \frac{1}{\sqrt{2}\pi \frac{N_A}{V_m} d_m^2} = \frac{RT}{\sqrt{2}\pi N_A p d_m^2}. \tag{53}$$

The mean free path of a gas depends only on temperature and pressure, and for air at 20 ^oC and 1 atm it equals to 0.066 μm. For comparison, again for air at NTP, molecular diameter and molecular spacing are 0.00037 μm and 0.004 μm, respectively. [1]

7 Particle Properties of Flue Gas from Wood Combustion

To model ESP performance it is essential to know or somehow approximate the properties of particles suspended in combustion gas.

The most important factor is the particle size which practically explains the level of the charge acquired by the particulates, and thus the particles' electrical mobility that is essential in determining the particle trajectories in an ESP. The other thing to be noted is the particle shape, though this is less important for fine particles for which the assumption of sphericality is more valid than for larger particulates. Evolution of particle size and shape respectively might take place by means of agglomeration and coagulation. However, these intriguing phenomena are out side the scope of this paper.

Properties of particulates that have influence on electrical phenomena in an ESP are particle cohesivity, resistivity, and electric permittivity of the particles. Cohesivity and resistivity mostly relate to dust layer behavior on the collector and electric permittivity is of importance when particle charging is considered. Unfortunately, information on wood combustor originated particulates' resistivities and other physical properties seems not to exist directly, only discussion of the elemental analysis, as in Refs. [19] and [26], can be found. The published information concerning fly ash resistivities corresponds almost exclusively to coal combustion flue gases, on which the discussion in this section is based.

7.1 Particles' Size And Shape

According to Ref. [2] the particles between 0.1 μm and 1 μm in diameter are solid particles formed by either sublimation of solid phase material or condensation of a vapor phase condition. Most of these particles have at some stage been in liquid or molten phase, and consequently surface tension tends to force the particles to obtain a spherical shape. Equally, the particles below 0.1 μm are stated to be spherical in shape.

Indeed, for small-scale wood combustion, as found out in MiniDust measurements, and in Refs. [8] and [19], especially for wood pellet burning devices the particles around 0.1 μm are the ones with most relevance, since there is a peak observed in the particle size distribution at the surroundings of the said particle size 0.1 μm. Consequently, assuming spherical particle shape becomes reasonably justified, and particles' size is simply described by a single parameter, their diameter d_p.

7.1.1 The Particle Size Distribution

The best fit to aerosol particle size distribution is obtained by applying lognormal distribution. There is no theoretical background from which this could be deduced, but it has proved its validity in experiments carried along the history of aerosol science. As expected, from the name of the distribution, the property distributed normally is the logarithm of the particle diameter, not the particle diameter itself. Furthermore, the characteristic parameters of lognormal distribution are the $\ln(CMD)$ and $\ln(GSD)$, respectively, where CMD and GSD are the Count Median Diameter and Geometric Standard Deviation of the conventional normal distribution. Mathematically formulating, the lognormal probability density distribution is written as [1]

$$df = \frac{1}{\sqrt{2\pi}\ln(GSD)} \exp\left[-\frac{(\ln(d_p) - \ln(CMD))^2}{2\,(\ln(GSD))^2}\right] d\,(\ln(d_p))\,. \tag{54}$$

It is more convenient to express the frequency function in terms of d_p than $\ln(d_p)$. Therefore, by substituting into equation (54) the result of the differentiation $d\,(\ln(d_p)) = d\,(d_p)\,/d_p$, one obtains

$$df = \frac{1}{\sqrt{2\pi}d_p\ln(GSD)} \exp\left[-\frac{(\ln(d_p) - \ln(CMD))^2}{2\,(\ln(GSD))^2}\right] d\,(d_p)\,. \tag{55}$$

Because for normal distribution 95 % of the particles fall within the size range $d_{mean} \pm 2\sigma$, where σ is the standard deviation, lognormally distributed particulate, for it's part, is found within the interval $exp\,[\ln(CMD) \pm 2\ln(GSD)]$ with said certainty of 95 percentages. This implies the corresponding lower and upper size range limits of CMD/GSD^2 and $CMD \cdot GSD^2$, respectively. The form of lognormal size distribution is illustrated in Figure 7, plotting the probability density as a function of both the particle diameter and the natural logarithm of the diameter. Logarithmic plot really implies the familiar bell shaped Gaussian curve, whereas the elongated tail to the right of the peak is seen to be characteristic of the linear scale plot.

7.1.2 The Cunningham Slip Correction Factor

It follows from the existence of submicron particles that the smallest particles are approaching the mean free path of the gas molecules, arising the need for introduction of a correction term to avoid the error due to continuum hypothesis. Therefore, we employ the Cunningham correction factor [1]

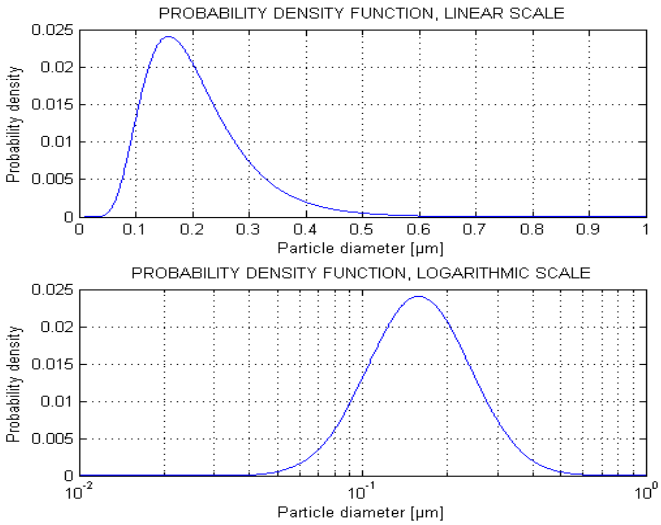

Figure 7: Probability density function plotted against the particle diameter (above) and the logarithm of the particle diameter (below). Plot realized for data obtained from MiniDust measurements with corresponding $CMD \approx 0.15$ and $GSD \approx \exp(0.53)$.

$$C_u = 1 + 1.246\frac{2\lambda}{d_p} + 0.42\frac{2\lambda}{d_p}\exp\left(-0.87\frac{d_p}{2\lambda}\right), \tag{56}$$

suggesting, as seen in the Figure 8, that slipping becomes significant for particles smaller than 10 μm in diameter. This leads to the conclusion that in the case of wood pellet combustion aerosols, the discontinuity of flue gases must be, indeed, taken into account.

7.2 Cohesivity and Resistivity of the Particles

Having deviated the particles on to the collector electrodes we want them not to get re-entrained. Thus, cohesivity plays an important role in ESP performance optimization. Particles are held to themselves and the collector by combination of electrical and mechanical Van-Der-Vaals forces. For particle electrical resistivities greater than 10 Ωcm, the electrical forces are dominant compared to the mechanical ones, which though, are of more importance for low resistivity dusts. [2]

The electrical resistivity of the particles is determined by the bulk volume conductivity and surface conduction. The first relates to particles' elemental content, whereas the latter is due to adsorbed surface layer. Suitable resistivity for dust particles lies between 10^{10} Ωcm and 10^{11} Ωcm, and for

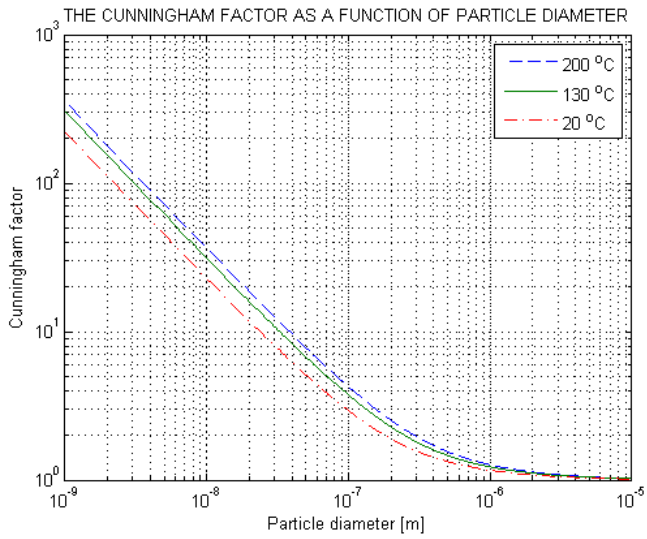

Figure 8: The Cunningham factor as a function of particle diameter. The influence of temperature on mean free path is pointed out plotting equation (56) at three temperatures.

temperatures between 100 ^oC and 200 ^oC, according to Ref. [2], resistivity should stay in between said limits, thanks to sufficient moisture content due to relatively low temperature. For high resistivity dusts, that is for resistivities around 10^{13} Ωcm, a disadvantageous effect of reverse ionization can reduce ESP performance: as dust accumulates on a collector, voltage difference starts to develop across the dust layer finally reaching a threshold, after which, charge carriers of reversed polarity are emitted [2]. The phenomenon is frequently referred to as back-corona effect, and is suggested to take place at locations that receive peak corona ion bursts [7, 25]. Consequently, one might suppose that the reverse ionization would be of less importance for two-stage precipitators, whose collectors are not mounted opposite to corona discharge wires. Re-entrainmet, for its part, is a problem for low resistivity dusts. The particles that arrive to the collector lose their charge so quickly that they are attached on the surface layer on as neutral particles that are easily entrained back into the flow [2, 24].

7.3 Particle Charging

In an ESP the charging of particles takes place typically as a combination of two mechanisms, field charging and diffusion charging. Field charging employs external electric field driving ions to collide with particles suspended in the background gas, whereas, in diffusion charging ions are transported to

the surface of particles by Brownian motion.[1]

In a two-stage ESP, if collection stage contains no ion source, such as corona wire, charging of the particles takes place practically solely in a charging stage, previous to the said collection stage, by diffusion charging. Wood combustion aerosol size distributions range over wide interval of particle diameters, even below 0.1 μm limit. Particle size thus approaches the mean free path of the background gas, i.e. $a \approx \lambda$, and we refer to transition region where neither continuum hypothesis nor kinetic theory of gases can be assumed. The transition region theories of today for particle diffusion charging seem to be approximative extensions from either continuum theories or kinetic theory of gases [27].

The widely used particle charging model giving reasonably good correspondence to experimental data, the Cochet model, combines both field and diffusion charging [2]:

$$Q_{sat} = \left[\left(1 + 2\frac{\lambda}{d_p}\right)^2 + \left(\frac{2}{1 + 2\frac{\lambda}{d_p}}\right)\left(\frac{\epsilon_r - 1}{\epsilon_r + 2}\right) \right] \pi \epsilon_0 d_p^2 E. \tag{57}$$

However, in the absence of ions in the external field area, such a model is no longer valid and one must seek diffusion charging theories. One commonly applied diffusion charging formula is expressed as

$$n = \frac{d_p kT}{2e^2} \ln\left(1 + \frac{\pi d_p c_i e^2 N_i t}{2kT}\right), \tag{58}$$

but it is said to be accurate only to within a factor of 2 for particles between $0.1 - 2\ \mu m$ and for $N_i t > 10^6\ s/cm^3$ [1]. Since the accuracy of the Eq. (58) is not too good, and above all because the size distribution of wood combustion aerosol extends both below and above its validity limits, a more precise model is needed However, there is no unique diffusion charging theory covering the whole range of aerosol particle sizes, which reaches from the macroscopic size scale, ($\lambda_i << a$), over the transition regime, ($\lambda_i \approx a$), to the free molecular zone, ($a << \lambda_i$) [27, 29]. Here, by a we denote the particle radius and λ_i is the mean free path of the ions being approximately 15 nm at 300 K [27, 29].

We start the discussion of our diffusion charging theory from the continuum diffusion mobility equation (59) that yields the flux of ions crossing a spherical surfaces of radius r [27]:

$$J(r) = -4\pi r^2 \left[D_i \frac{dN_i}{dr} - Z_i N_i E(r) \right], \tag{59}$$

where Z_i and D_i are the diffusion coefficient and the electrical mobility of the ions, respectively. In Ref. [27] it is stated that the above equation (59)

has been solved by various authors independently, obtaining the ion flux on a particle of given size

$$J_n = \frac{dn}{dt} = \frac{4\pi D_i N_i}{\int_a^\infty (1/r^2) \exp(\Phi(r)/kT)\, dr}, \tag{60}$$

where $\Phi(r)$ is the ion-particle interaction potential written as [27, 29, 31]

$$\Phi(r) = \int_r^\infty F dr = K_E \left[\frac{ne^2}{r} - \gamma \frac{a^3 e^2}{2r^2 (r^2 - a^2)} \right], \tag{61}$$

in which $K_E = 1/(4\pi\epsilon_0)$, is a factor needed in SI unit system and $\gamma = (\epsilon - 1)/(\epsilon + 1)$ corrects the second term for non-ideal conductors. The first term at the right side of the Eq. (61) corresponds to the familiar Coulomb force, whereas the second one represents the image force [27, 29, 31].

Image force is the attractive force between an ion and the charge distribution of an aerosol particle induced by the ion and can be neglected when $\epsilon_r \longrightarrow 1$, as one notices by taking a look at the γ-factor [33]. In Ref. [27] it is argued that image force must be taken into account for particles smaller than few hundred nanometers. Exclusion of the image force term vanishes the singularity at the particle surface observed in the integrand of the equation (60), and an expression, thus valid in the continuum regime, is easily obtained for evaluation of average charge carried by an aerosol particle [27]:

$$J(n) = \frac{dn}{dt} = K_E \frac{4\pi D_i N_i n e^2}{kT \left[\exp\left(K_E \frac{ne^2}{akT} \right) - 1 \right]} \tag{62}$$

It is expected that equation (62) gives better results than equation (58). However, keeping in mind the size range of wood combustion aerosols involving particles of order of few hundred nanometers the necessity of inclusion of the image force must be underlined.

7.3.1 The Limiting-Sphere Theory

To account for the image force effect for small aerosol particles Fuchs' limiting-sphere theory is employed. In Ref. [28] experimental results are presented and found to agree well with the limiting-sphere theory for conducting particles, $0.01 - 0.3\ \mu m$ in diameter. Similarly, experimental data for $0.004 - 0.075\ \mu m$ particulates, both conducting and dielectric ones, is reported to fit the theory of Fuchs and adviced to be favored over free molecular theory approximations, such as Ref. [32] and further ones, for particles larger than $0.01\ \mu m$. Furthermore, in Ref. [27], in addition to listing various authors reporting results supporting the Fuchs' theory, a confirmation against

Monte-Carlo simulation is presented for particle size range $0.005 - 1\ \mu m$. Limiting-sphere theory is a modification to macroscopic diffusion-mobility equation, which means that for $a >> \lambda_i$ the Fuchs law should approach the continuum theory and application of the theory to be safe also for particles larger than the ones in the above mentioned articles. Therefore, it should be justified to expect the limiting-sphere theory to be the best theory available for particles bigger than $0.01\ \mu m$ in diameter.

In the theory Fuchs two major consideration are included: the image force effect and the jump-wise change in ion concentration at the surface of the particle at the moment of every recharging. If the concentration jump was neglected one would have to put $N_i = 0$ at surface of the particle. However, to include the jump the particle is surrounded by a concentric sphere with radius $\delta = a + \lambda'$, where δ is called the limiting-sphere radius, and λ' is the mean distance from the surface of the particle at which the ions collide for the last time with gas molecules before reaching the particle. The limiting-sphere radius is expressed as [31]

$$\delta = \frac{a^3}{\lambda_i^2}\left[\frac{(1+\lambda_i/a)^5}{5} - \frac{(1+\lambda_i^2/a^2)(1+\lambda_i/a)^3}{3} + \frac{2}{15}\left(1+\lambda_i^2/a^2\right)^{5/2}\right], \quad (63)$$

where λ_i is the mean free path of the ions. Now, outside the limiting sphere the ion diffusion is treated with macroscopic diffusion laws, equation (60), whereas inside the sphere the ions are taken to travel freely without any collision except that with the particle. However, the probability of an ion emerging into the limiting-sphere to collide with the particle does not obviously equal to unity.[31]

The collision probabilities α are found by minimizing equation

$$b^2 = r^2\left[1 + \frac{2}{3kT}\left(\Phi(\delta) - \Phi(r)\right)\right], \quad (64)$$

with respect to the collision parameter b, *i.e*, taking the derivative

$$\frac{db^2}{dr} = 0 \quad (65)$$

and allowing only solutions for which $a < r_m \leq \delta$ [34]. In Eq. (64) Φ is the ion-particle interaction potential described by Eq. (61). By substituting the appropriate r_m's into equation (64):

$$b_m^2 = r_m^2\left[1 + \frac{2}{3kT}\left(\Phi(\delta) - \Phi(r_m)\right)\right], \quad (66)$$

one obtains the minimum collision parameter b_m. If b^2 has no minimum between a and δ, the collision probability goes to unity, i.e, $\alpha = 1$ and all the ions emerging into limiting sphere reach the particle surface. When the minimum exists, only the particles for whom $b < b_m$ reach the particle and the collision probability is expressed as [31]

$$\alpha = \left(\frac{b_m}{\delta}\right)^2. \tag{67}$$

Fuchs presents a table of α-values that have been criticized, for example in Ref. [29], for unrealistic values for ion properties. Furthermore, in Ref. [30] it is argued that Fuchs' statement, $\alpha = 1$ for attractive encounters, is not valid. Even though this not of importance in unipolar environment, it is advisory to refer in Ref. [30] for tabulated α-parameters, calculated with more realistic ion properties.

Finally, equating the two fluxes, the one given by the macroscopic diffusion-mobility theory and the other described by means of thermal motion and ion-particle interaction, at the limiting-sphere, the flux of ions on a particle of given size is obtained [31]:

$$J_n = \frac{4\pi a D_i N_i}{\left[\left(4D_i a\right) / \left(\alpha c_i \delta^2\right)\right] \exp\left(\Phi\left(\delta\right) / \left(kT\right)\right) + \Psi}, \tag{68}$$

where

$$\Psi = a \int_{\delta}^{\infty} \left(1/r^2\right) \exp\left(\Phi\left(r\right) / kT\right) dr.$$

If one wishes to employ equation (68) to predict the average charge acquired by a particle under given $N_i t$-conditions, it is necessary to maintain the number of elementary charges, n, as a variable and integration of the integrand in the denominator might be difficult. However, if J_n is calculated for one constant $n = \{0, 1, 2, ...\}$ at a time, numerical integration becomes possible. This gives the motivation to apply the source-and-sink theory presented in section 7.3.3.

7.3.2 Ion Properties

To find out the flux of ions to an aerosol particle, as expressed by equation (68), the ion properties, diffusion constant D_i, the mean free path λ_i, the mean thermal speed c_i and the mass m_i, have to be known. Knowing only the mass and the electrical mobility Z_i enables us to calculate the remaining properties using the equations (69), (70) and (71). Pui, in Ref. [29], refers

to his earlier work[2] stating the hydrated protons $H^+(H_2O)_6$ to be the most abundant ionic species produced in positive corona chargers. In the case of the hydrated protons the mass and electrical mobility become 109 AMU and 1.4 $cm^2/(Vs)$, respectively [29]. In Ref. [29] there is tabulated data from various authors supporting the results of Pui, at least when compared against the ionic mass used by Fuchs, $m_i = 29\ AMU$.

Now, knowing the electrical mobility of the ions allows us to calculate the diffusion coefficient for the ions by Einstein's equation [29, 1]

$$D_i = \frac{kTZ_i}{n_i e}, \tag{69}$$

where n_i is the charge number of the ions, equal to unity for hydrated protons. The mean thermal speed is given by the conventional kinetic theory equation as [29, 1]

$$c_i = \left(\frac{8kT}{\pi m_i}\right)^{1/2}. \tag{70}$$

In Ref. [27] various formulas to calculate the mean free path of the ions is reported, but the one obtained applying the Maxwell-Chapmann-Enskog theory of molecular diffusion is stated to be utilized by most works in aerosol science, as is done and given in Ref. [29] as

$$\lambda_i = \frac{D_i}{(1+\epsilon_{im})\,\frac{3\pi c_i}{8\sqrt{8}}\left(\frac{m_i+m_m}{m_m}\right)^{1/2}}. \tag{71}$$

Here ϵ_{im} is a small correction factor being 0.132 and 0.016 for hard spheres of extremely unequal and equal masses, respectively [29]. Molecular weight m_m for dry and saturated air are 28.9 AMU and 28.7 AMU, respectively [1]. We deduce that $m_m = 109\ AMU$ and $m_i = 29\ AMU$ are unequal enough to be considered extremely unequal, and consequently $\epsilon_{im} = 0.132$ is used in Eq. (71) from now on in this paper.

7.3.3 The Source-and-Sink Method

It was noted in the end of the section 7.3.1 that getting approximative results for charge level on aerosol particles through equation (68) was not possible due to difficult integral when the number of elementary charges carried by the particle, n, was maintained as a variable. However, for constant n numerical integration is enabled, and the steady-state ion flux is linked to time

[2]Pui, D., 1976, *Experimental study of diffusion charging*, Ph.D. Thesis, University Of Minnesota, Department of Mechanical Engineering

evolution of the charge distribution on the particles employing the combination coefficients $\beta_n = J_n/N_i$, where J_n is written as in equation (68) and N_i is the ion concentration.

The evolution of the charge distribution on monodisperse particles is obtained by solving simultaneously the following infinite group of differential equations [27, 28, 29][3]:

$$\begin{cases} \frac{dN_0}{dt} = -\beta_0 N_0 N_i \\ \frac{dN_1}{dt} = \beta_0 N_0 N_i - \beta_1 N_1 N_i \\ \vdots \\ \frac{dN_j}{dt} = \beta_{j-1} N_{j-1} N_i - \beta_j N_j N_i, \end{cases} \tag{72}$$

where N_n is the number fraction of particles carrying n elemental charges and N_i is the concentration of unipolar ions in the background gas. The stochastic birth-death process, described by the above set of equations (72) is solved with initial conditions $N_0 = 1$ and $N_n = 0$ for $n = 1, 2, 3, ..., j$ at $t = 0$ corresponding to the situation in which all the particles are expected to carry zero units of charge at the beginning of the charging process.

The positive terms in the equations (72) describe the rate of increase in concentration of particles carrying n elemental charges from collision between an ion and a particle carrying $n - 1$ charges, whereas, correspondingly, the negative terms represent the decrease in concentration of particles carrying n charges from a collision between an ion and a particle already carrying n units of charge. [29]

Although in theory the number of equations should be infinite, in practice it is enough to set the number of equations big compared to the expected average charge of a particle of given size. The source-and-sink method enables calculation of evolution of charge distribution on monodisperse particles and evaluation of average charge carried by particulates immersed in a gas with ion concentration N_i at a given moment of exposure time t. [27, 28, 29]

To convince the reader about the validity of the above theory, the results plotted in Figs. 5 and 6 in Ref. [27] are reproduced in Figures 9 and 10. Furthermore, for larger particles comparison can be made against results based on numerical solution by Liu and Pui (1977) presented in [1]: $Q_p(4\ \mu m) = 158e$ and $Q_p(10\ \mu m) = 395e$, at $N_i t = 10^{13}\ s/m^3$ and expectedly at 300 K. Corresponding values obtained with Source-and-Sink theory are $Q_p(4\ \mu m) = 163e$ and $Q_p(10\ \mu m) = 403e$. Comparison of the results gives us reason to believe that the equation set (72) is properly formulated and

[3][27, 28, 29] all refer to the article: Boisdron, K., Brock, J., 1970, *on the stochastic nature of the acquisition of electrical charge and radioactivity by aerosol particles*, Atmospheric Environment, 4; as the original source of the source-and-sink method

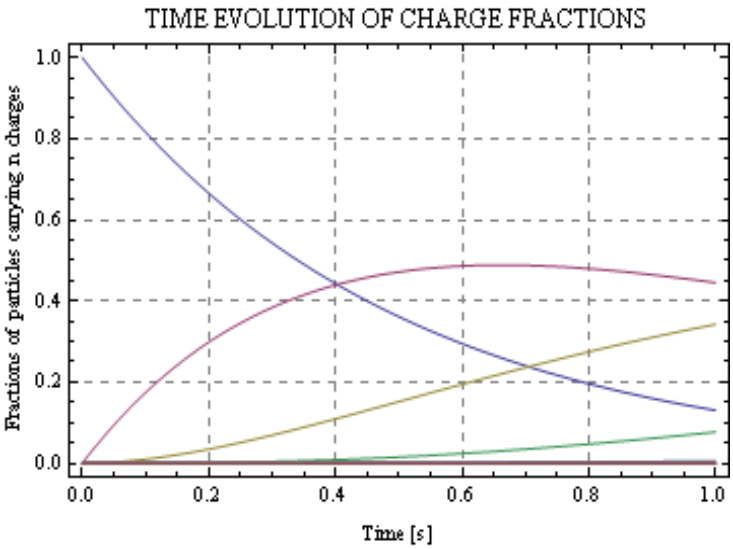

Figure 9: Time evolution of charge fractions on monodispersed 0.1 μm, $e_r = \infty$ particles at 300 K, $p = 1$ bar and $N_i = 10^{12}$ $1/m^3$. Reading from top to bottom, before the curves cross, the fractions plotted are N_0, N_1, N_2, N_3 and N_4.

realized in Mathematica and that further results, based on Source-and-Sink theory, presented in this paper are reliable.

Having validated the Source-and-Sink method against reported results, we compare it to equation (58) to justify the need for such a complicated set of equations as those formulated above. The average number of elementary charges acquired by aerosol particles as a function of particle diameter, by both the methods, are plotted in Figure 11

Looking Figure 11 shows that between the diameter interval $0.001-10$ μm the difference between the charge levels proposed by the theories compared approaches one order of magnitude, a significant figure, and further applying of equation (58) is no longer justified, since, as mentioned above, the Source-and-Sink theory has been tested successfully against experimental results and Monte-Carlo simulation.

It should also be noted that average charge is not really a reasonable physical quantity when single particles are considered, because charge on a particle can only occur as multiples of the charge of electron. As a consequence in further calculations the number of charges carried by a particle is rounded down to closest integer for $n > 1$, whereas for $n < 1$ we round up to unity. This has to be done to obtain realistic particle migration velocities and trajectories in an electric field, especially for small particles.

It is important to keep in mind however that to have the average charge

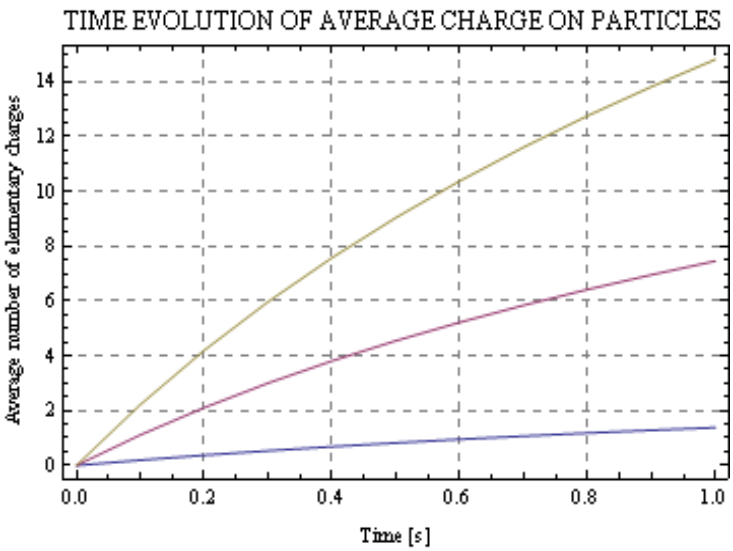

Figure 10: Time evolution of average number of elementary charges on $e_r = \infty$ particles at $300K$, $p = 1\ bar$ and $N_i = 10^{12}\ 1/m^3$. Reading from top to bottom the curves correspond to 1 μm, 0.5 μm and 0.1 μm particles.

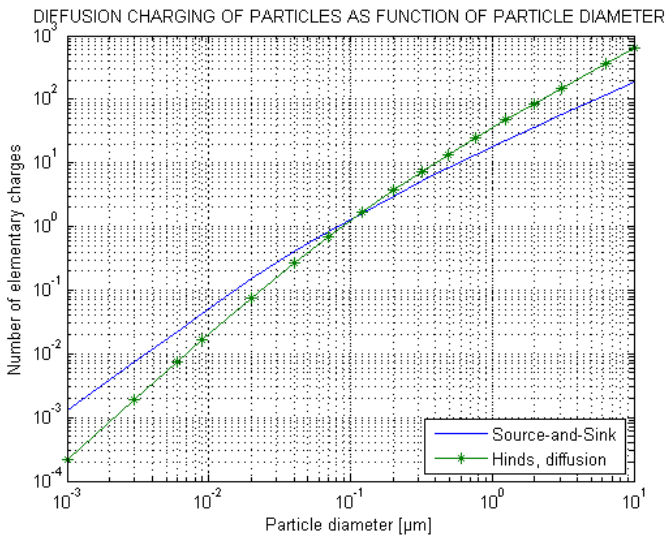

Figure 11: Average number of elementary charges acquired by diffusion charging at $T = 130\ ^oC$ and $N_i t = 10^{12}\ s/m^3$ based on Source-and-Sink theory and equation (58).

number below unity, a considerable fraction of particles must carry zero charge. This is observed in Figure 12 where the charge distribution on monodispersed 0.02 μm particles is plotted, illustrating the fact that more than 80 % of the said 0.02 μm particulates do not carry a one extra elemental charge at $N_i t = 10^{12}\ s/m^3$. This leads to inevitable leakage in an ESP. However, for particles having average charge number well above unity the situation is no longer as serious as illustrated in Figure 13 for 0.3 μm particles, for whom the zero charge number fraction practically vanishes. In addition, Figure 13 roughly demonstrates the fact that charge on monodisperse aerosol particles is normally distributed, as also mentioned in [1, 27].

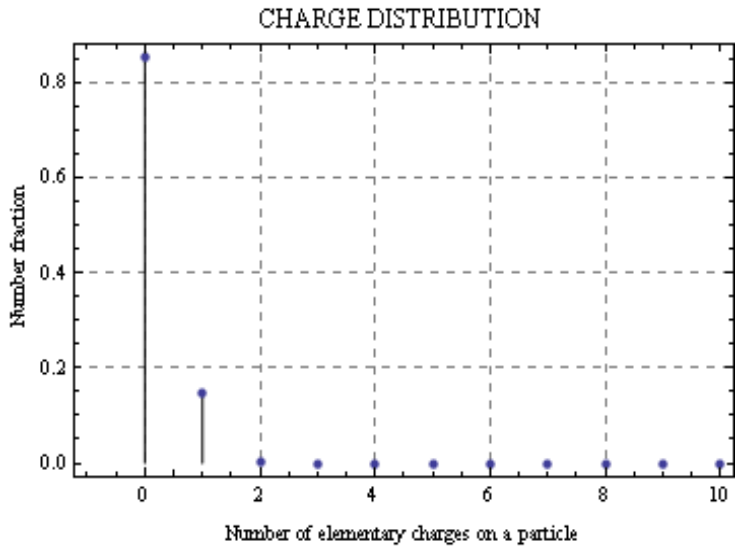

Figure 12: Charge distribution on monodisperse 0.02 μm particles acquired by diffusion charging at $T = 130\ ^oC$ and $N_i t = 10^{12}\ s/m^3$, as predicted by the Source-and-Sink theory.

7.4 Particle Equation Of Motion

In order to model particle trajectories in an ESP, one has to define the equation of motion for a particle. Intuitively, the forces exerted on a particle in an ESP are electric, drag and inertial forces. To determine the relative importance of the drag and the inertial forces, we employ particle Reynolds number.

For values valid for a small-scale ESP, such as 1 μm particle diameter, the flow and the particle velocity difference $U = 1\ m/s$, air viscosity $\eta = 1.8 \cdot 10^{-5}\ Pa \cdot s$ and density 1.3 kg/m^3,

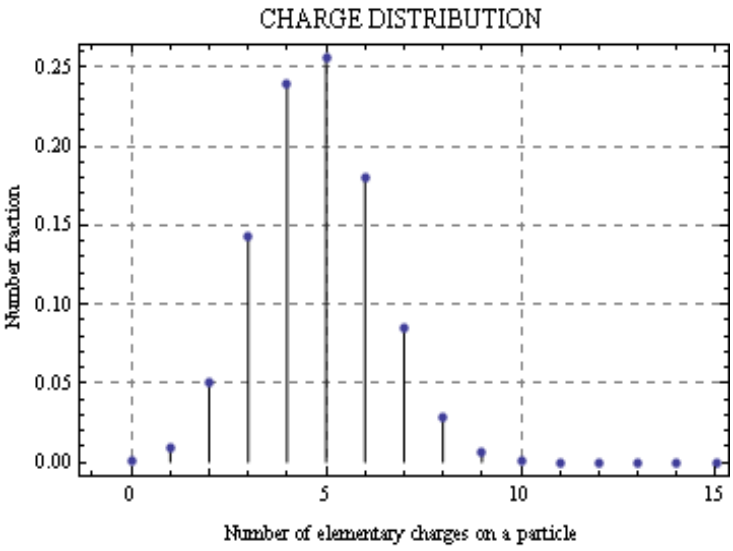

Figure 13: Charge distribution on monodisperse 0.3 μm particles acquired by diffusion charging at $T = 130\ ^oC$ and $N_i t = 10^{12}\ s/m^3$, as predicted by the Source-and-Sink theory.

$$R_e = \frac{\rho U L}{\eta} \approx 0.07 << 1.$$

This implies, according to Ref. [1], that flow around a particle, even relatively large one for a wood pellet fly ash particle, is laminar and that the drag force exerted on it is described by the Stokes law. The Stokes law is a solution of Navier-Stokes equation (37), obtained assuming inertial forces to be negligible compared to the viscous ones, incompressibility of the fluid, sufficient distance from the walls, constant motion, and that the particle is a rigid sphere on whose surface the fluid velocity is zero. Taking also into account the 'slipping' occurring on the surface of the particles whose size is approaching the mean free path of the gas, the drag force, modified with Cunninham slip correction factor (see Eq. (56)), is written according to Stokes as [1]

$$F_D = \frac{3\pi\eta\left(\vec{u}_p - \vec{u}\right) d_p}{C_u}. \tag{73}$$

When the electric force that an electric field exerts on a particle is described in familiar fashion, multiplying the particle charge Q_p by the electric field $\vec{E}$, we obtain the equation of motion for a charged particle carried by fluid flow:

$$Q_p\vec{E} + 3\pi\eta d_p\left(\vec{u}_p - \vec{u}\right)/C_u = m_p\frac{d\vec{u}_p}{dt}. \tag{74}$$

7.5 Particle Migration

The particle motion in an ESP results from the forces acting on it. Neglecting the force of gravity and the inertial forces, the electric force $\vec{F}_{el}$ and the drag force $\vec{F}_D$ are the ones present in the precipitation stage. Assuming the flow velocity to have only a plate wise component, we can write the equation of motion, Eq. (74) of a particle, carrying electric charge Q_p, in the direction perpendicular to the plate electrodes as

$$\frac{dw}{dt} + \frac{3\pi\eta d_p}{m_p(C_u)}w = \frac{Q_{sat}}{m_p}E, \tag{75}$$

where w is the particle migration velocity. Equation (75) is a linear differential equation of first degree, whose solution is generally known. Therefore, taking $w(t=0)=0$ as the initial condition the migration velocity of a flue gas particle can be written as [2]

$$w(t) = w_{th}\left[1 - exp\left(-\frac{t}{\tau_p}\right)\right] \tag{76}$$

where

$$\tau_p = \frac{m_p(C_u)}{3\pi\eta d_p} = \frac{\rho_{pa}d_p^2}{18\eta}(C_u) \tag{77}$$

and

$$w_{th} = \frac{Q_{sat}E}{3\pi\eta d_p}(C_u). \tag{78}$$

Here m_p and ρ_{pa} are the particle mass and density respectively, whereas τ_p is the relaxation time, characterizing the dynamic behavior of the particle. w_{th} is the steady state velocity of the particle, i.e, its theoretical migration velocity. Therefore, after infinite time $w(t) = w_{th}$. [2]

Evaluation of particle mass is not a straightforward task. The composition of particles might vary remarkably and the density is normally evaluated as a bulk property. In Ref. [11] some information about fly ash densities of wood combustion is compiled. Including the reference, that the fly ash densities built up on the surface of flue gas pipes of wood pellet burners would be between $380-400\ kg/m^3$. As mentioned, these refer to bulk numbers and

'real' density of a single particle is presumably higher. In future, we consequently apply particle density $\rho_{pa} = 450\ kg/m^3$. Taking $\rho_{pa} = 450\ kg/m^3$, compared to the bulk densities $380 - 400\ kg/m^3$, increases the mass and thus inertia of the particles, leading to underestimated acceleration, and further underestimation of ESP performance, as intended, provided that the overestimation of density is sufficient.

Particle emissions of wood combustion are mainly of submicron particulates. Employing Eq. (76) one can calculate that all the particles smaller than $10\ \mu m$ reach their steady state velocity after only $1\ ms$, i.e., $w(1\ ms) \approx w_{th}$. This is a time interval vanishingly small compared to the particles' residence time between the electrodes. Therefore, we can safely assume theoretical migration velocity for particle velocity component perpendicular to the plates. This is true even for charge levels calculated from Source-and-Sink theory for diffusion charging only.

In Figure 14 theoretical migration velocity is plotted against particle diameter for combined charging as predicted by Cochet equation (57) and for pure diffusion charging as obtained with Source-and-Sink theory. Electric field is set at $400\ kV/m$ and diffusion charging is realized for two common values $10^{12}\ s/m^3$ and $10^{13}\ s/m^3$ for $N_i t$-product, the most important parameter when it comes to diffusion charging [27, 1, 35]. It is observed that migration velocities predicted by the Source-and-Sink theory are generally lower compared to those yielded by Cochet model. This is explained by higher charge levels obtained assuming combined field and diffusion charging and possible inaccuracy of the analytical Cochet model compared to the numerical solution of the Source-and-Sink theory.

For combined charging, one notices from Figure 14 that there is a minimum velocity experienced around $0.4\ \mu m$. This is because for the particles smaller than the ones in the region $0.1 - 0.8\ \mu m$, the reduction in charge carrying ability, being only weak function of electric field, is compensated by decreased fluid friction experienced, whereas the particles larger than the minimum have the advantage of charge increase proportional to the square of the electric field outweighing the fluid friction, that is only linearly proportional to the particle diameter.

However, when the influence of field charging is taken to vanish, one alarmingly discovers that for particles larger than $0.1\ \mu m$, for whom field charging is of increasing importance, provided sufficient ion density, the theoretical migration velocity keeps on decreasing moderately, contrary to the case of combined charging. This implies poorer ESP performance and is thus a cause for concern.

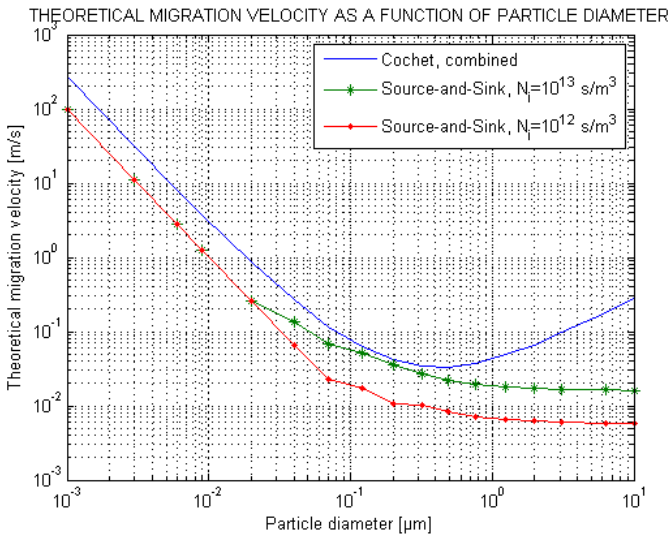

Figure 14: Theoretical migration velocity as a function of particle diameter for $e_r = 1.5$ particles at 130 ^{o}C.

7.6 Collection Efficiency

The quality of various devices is determined by their efficiency, and when talking about ESPs we refer to their collection efficiency. When dust precipitation is concerned, we are usually dealing with polydisperse aerosols. This makes consideration of particle size-dependent characteristics inevitable. Maybe the best way to take into account the particle size dependency of particle separation is to illustrate the process with grade efficiency curve, i.e., by plotting the collection efficiency per a size class, a particle diameter interval, as a function of the mean diameter correspondent to the size class. For infinitesimal size classes we can express the two simplest ways to determine the collection efficiency, by the laminar model [2]

$$\eta_{laminar} = \frac{w_{th}L}{Us}, \tag{79}$$

and the Deutsch-Anderson (DA) model [2]

$$\eta_{De} = 1 - \exp\left(-\frac{w_{th}L}{Us}\right). \tag{80}$$

By laminarity, here we mean that there is no remixing force, such as turbulent force, present to compete against Coulomb force driving the particles towards the collectors. In Deutsch-Anderson model, turbulent behavior is taken into account, assuming that at any point down stream from the

inlet, the particulates not yet collected are evenly distributed between the electrodes. [2]

In Figure 15 the DA efficiencies are plotted for two electric field strengths, 600 kV/m and 400 kV/m, assuming combined charging as predicted by Cochet equation (57) and diffusion charging, as yielded by the Source-and-Sink theory, at $N_i t = 10^{13}\ s/m^3$ and $N_i t = 10^{12}\ s/m^3$. Consequently, the fierce impact that the electrical conditions, ion concentration and residence time corresponding to diffusion charging, have on ESP performance are illustrated. It is noted that the form of theoretical migration velocity curve (see Figure (14) is almost directly transferred to efficiency characterization, underlining the importance of particles' size dependency in charge carrying ability and fluid friction experienced. As was noticed in the previous section 7.5 vanishingly small field charging regime leads, as a consequence of reduced charge levels, to considerable decrease in migration velocity for particles larger than 0.1 μm. This has severe effects on ESP performance as, Figure 15 clearly shows: the DA-efficiency for larger than 1 μm particles is unable to exceed 70 %-value, even at $E = 600\ kV/m$ and $N_i t = 10^{13}\ s/m^3$. Fortunately, particles this large, $d_p > 1\ \mu m$, are not found too frequently in small-scale wood combustion flue gases [8, 11]. For particles smaller than 0.1 μm relatively good efficiencies, approaching the 90 %-limit, are obtained at $N_i t = 10^{13}\ s/m^3$ and at $E = 400\ kV/m$, whereas at $N_i t = 10^{12}\ s/m^3$ neighter of the electric field values gives acceptable efficiencies.

Furthermore, the laminar and turbulent efficiencies are compared in Figure 16 at $N_i t = 10^{13}\ s/m^3$ for electric field strengths $E = 400\ kV/m$ and $E = 600\ kV/m$. As expected, laminar flow implies higher efficiencies due to lack of remixing force resisting the Coulomb force originated particle migration towards the collectors.

7.7 Influence of Space Charge

7.7.1 Turbulent Space Charge Profile

As flue gas flow proceeds between the electrodes, particles tend to escape from the flow and get deposited on the collectors. If plate wise reduction is assumed to be exponential, and the concentration to remain constant in direction perpendicular to the plates, the model corresponds to turbulent flow and the deposition is somewhat similar to stirred settling.

Consider a cross-sectional area Ls at the inlet of a precipitators plate-to-plate space (see Figure 17). As the collection process proceeds, after elapsed time dt, a number fraction dc/c of the particles, corresponding to the negative of the ratio of the areas Lds/Ls, will have escaped from the cross-sectional

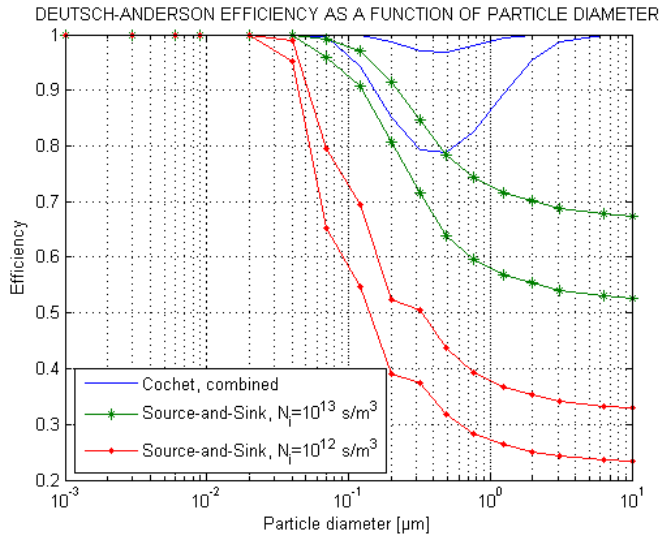

Figure 15: Deutsch-Anderson efficiency as function of particle diameter at 130 ^oC and $N_it = 10^{13}$ s/m^3 for $e_r = 1.5$, $U = 0.13$ m/s and $L = 30$ cm. The upper curves correspond to 600 kV/m and the lower ones to 400 kV/m.

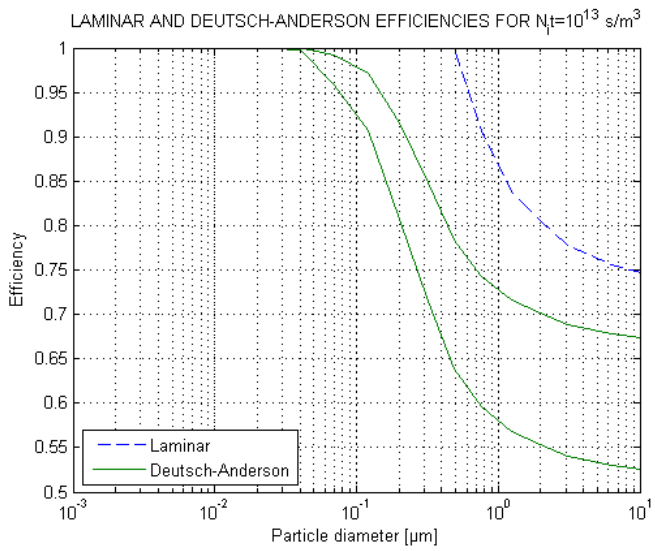

Figure 16: Laminar and Deutsch-Anderson efficiencies as function of particle diameter at 130 ^oC and $N_it = 10^{13}$ s/m^3 for $e_r = 1.5$, $U = 0.13$ m/s and $L = 30$ cm. The upper curves correspond to 600 kV/m and the lower ones to 400 kV/m.

space and deposited on the collector. Mathematically formulating we obtain

$$\frac{dc}{c} = -\frac{Lds}{Ls} = -\frac{w_{th}dt}{s}.$$

The time dt required for collection of the fraction dc/c, equals, in plate wise direction, the distance traveled by the particulates dx, divided by the mean velocity of the flow to x-direction, noted by U. Therefore

$$\begin{aligned} \frac{dc}{c} &= -\frac{w_{th}dx}{sU} \\ &\Rightarrow c = c_0 \exp\left(-\frac{w_{th}x}{sU}\right). \end{aligned}$$

Now, for the particles that are taken to be equal in size d_i, the particle space charge q_i is obtained multiplying the particle number concentration c_i by charge carried by a single particle $Q_p(d_i)$:

$$q_i = Q_p\left(d_i\right) c_i \exp\left(-\frac{w_{th}\left(d_i\right) x}{sU}\right). \tag{81}$$

The Eq. (81) is now of such a form that it enables us to calculate the total space charge, carried by the particulates suspended in a flue gas flow, by summing over the $i = \{1, 2, ..., n\}$ size classes. In MiniDust laboratory tests an Electrical Low Pressure Impactor (ELPI) was used to determine the size distribution of the flue gas particulates. Since the ELPI used classified the particles to 12 size fractions, Eq. (81) is applied for $n = 12$ in this paper.

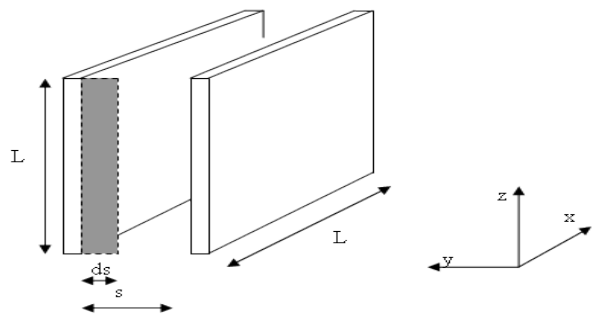

Figure 17: Some plate type ESP dimensions.

7.7.2 Laminar Space Charge Profile

For turbulent flows we assumed concentration gradient to be zero in direction perpendicular to the plates, which is not valid for laminar flows, in absence of turbulent dispersion. Instead, the concentration is taken either to remain at its constant inlet value or to be zero. When traveling in plate-to-plate space the particles are assumed to move as bulk matter, so as deposition proceeds a triangular[4] concentration domain is formed getting more and more narrow towards the outlet end of the plate with polarity opposite to that of the particles. Outside of the domain the space charge is zero (see Figure 18).

Now suppose that a particle, with diameter d_i, carrying charge $Q_p(d_i)$, arrives to the inlet of the plates with horizontal average velocity U, independent of y, the way that to get collected it has to travel the maximum vertical distance s. There is a homogeneous electric force field between the plates that the particle senses, immediately obtaining the maximum vertical velocity, that is, the theoretical migration velocity w_{th}. Let then t_s be the time spent by the particle to travel the distance s. Now t_s equals to t_{x_i}, the time spent to travel the horizontal distance x_i, when the particle reaches its point of capture on a collector (see Figure 18). Therefore, the particle trajectory for given size class d_i, provides the spatial limiting curve of zero concentration for monodispersed particulates, d_i in diameter:

$$y(x) - y_0 = \frac{s}{x_i}(x - x_0) = \frac{s}{x_i}x, \tag{82}$$

when taking for simplicity $x_0 = 0$. Now, $t_s = t_{x_i}$ implies

$$\frac{s}{w_{th}(d_i)} = \frac{x_i}{U},$$

and by solving for x_i:

$$x_i = \frac{U}{w_{th}(d_i)}s. \tag{83}$$

Then, substituting equation (83) into (82) results

$$y(x) = y_0 + \frac{w_{th}(d_i)}{U}x, \tag{84}$$

where $w_{th}(d_i)$ is calculated for particle d_i in diameter using equations (48) - (78) as demonstrated in Sections 6.1 - 7.5. Therefore, the space charge profile for laminar flow can be expressed as

[4] if particle trajectory is approximated by straight line. Actually the slope varies due to parabolic velocity profile as seen further in the simulation results.

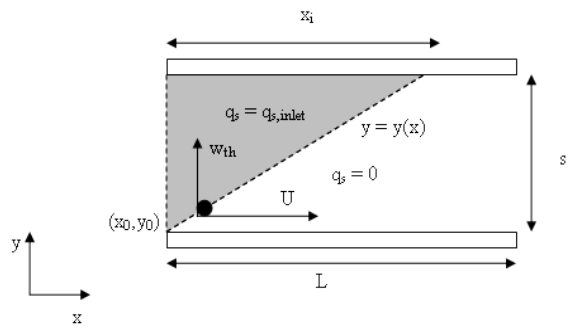

Figure 18: Particle migration and space charge profile under laminar conditions.

$$q_{s,inlet}\left(d_i\right) = \begin{cases} q_{s,inlet}\left(d_i\right) & \text{when} \quad y \geq y(x) \\ 0 & \text{when} \quad y < y(x) \end{cases} \tag{85}$$

The above derivation is valid for monodisperse aerosol characterized by the diameter d_i of its particles. Nevertheless we are interested in studying aerosols composed of various particle sizes. The substantial difference of life times of particles of different sizes in an ESP is taken into account by labeling multiple triangular subdomains corresponding to the degree of polydispersion. The space charge of each subdomain is then determined by taking the sum of the space charges correspondent to size fractions present at the subdomain.

Say, that we have for example a polydisperse aerosol with three distinguishable particle size classes characterized by their diameter d_1, d_2 and d_3. Let then the migration velocities related to be $w_{th}(d_1) > w_{th}(d_2) > w_{th}(d_3)$, thus implying $x_1 < x_2 < x_3$. We therefore conclude that the space charge densities of subdomains 1, 2 and 3 must be $q_1 + q_2 + q_3$, $q_2 + q_3$ and q_3, respectively, as illustrated in Figure 19. Deduction can be generalized for n-disperse case, particularly for 12 channel ELPI, used in MiniDust measurements.

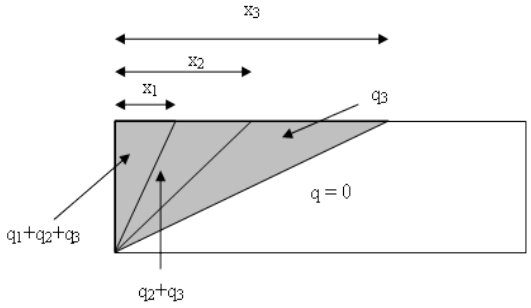

Figure 19: Subdomains of laminar space charge model. Example for three distinguishable particle size classes.

8 Overview of the Model

The constructed model supplies the means for particle trajectory analysis for charged particles in overlapping gas flow velocity and electric fields.

The Set Of Fundamental Equations

The flow velocity field between the ESP plates is generated solving the Navier-Stokes equation (37),

$$\rho_f \frac{\partial \vec{u}}{\partial t} + \rho_f \left(\vec{u} \cdot \nabla\right) \vec{u} = \rho_f \vec{f} - \nabla p + \eta \nabla^2 \vec{u},$$

whereas, to apply the required electrical conditions, the Poisson equation for electric potential, Eq. (11),

$$-\nabla^2 \phi = \frac{\rho_s}{\epsilon \epsilon_0},$$

is solved. To calculate the trajectory of a fly ash particle, carrying charge Q_p, and subjected to the electric and flow fields, the equation of motion written as

$$Q_p \vec{E} + 3\pi\eta d_p \left(\vec{u}_p - \vec{u}\right) / Cu = m_p \frac{d\vec{u}_p}{dt},$$

is employed, where

$$Q_p \vec{E} = \vec{F}_{el},$$

the electric force, and

$$3\pi\eta d_p \left(\vec{u}_p - \vec{u}\right) / Cu = \vec{F}_D,$$

the Stokes drag force. Furthermore, the particle charge Q_p is obtained either by the Source-and-Sink theory presented and discussed in section 7.3.3, thus neglecting field charging, or by Cochet combined charging equation, Eq. (57).

The Required Input

The above listed formulas form the group of fundamental equations of the model. To produce velocity field $\vec{u}$ as an output, the Navier Stokes equation requires gas viscosity η and density ρ as an input. To solve the Poisson equation for the electric potential $\Delta\phi$, the space charge density ρ_s and relative permittivity $e_{r,gas}$ of the gas have to be known. The space charge density is taken to constitute solely of the particles suspended in the gas, therefore ignoring the gas ion contribution. For particle equation of motion the mass m_p

and the charge Q_p carried by the particle to be traced are fed in. These input parameters are calculated following the procedures and equations introduced in Sections 6 and 7.

The Boundary Conditions

In addition to the conditions and properties of the gas and the particles, the conditions governing the boundary phenomena have to be defined. For the flow velocity a parabolic profile is applied at the inlet of the plate-to-plate space, whereas at the outlet the zero normal stress and normal flow conditions are applied. At the solid wall boundaries, no slip condition is utilized, thus setting zero flow velocity at the the electrode surfaces. The electrical boundary conditions are set by means of voltage difference. The electrodes are set at wanted potentials, whereas at the inlet and the outlet the zero charge/symmetry condition is used, specifying that the normal component of the electric displacement equals to zero.

9 Simulations, Results and Discussion

As a result of the MiniDust project and groundwork done by the present writer, two new suggestions for an ESP configuration, primarily designed for small-scale wood combustion devices, have emerged. Based on simulation results the two configurations are compared by means of particle trajectory analysis. For rotating plate precipitator the results are compared to and verified by the predictions suggested by the laminar model for precipitation efficiency, Eq. (79), since the Reynolds number for gas flow indicates that the nature of the flow is laminar (see Section 6.2). For both configurations, simplified 3D geometries are also constructed. Furthermore, for the plate type ESP, the space charge effects are studied. All the simulations are performed using commercial Comsol Multiphysics 3.4 FEM-based software, employing the Incompressible Static Navier-Stokes and Electrostatics Modes.

Due to the diversity of physical phenomena involved, various simplifying assumptions are made. The agglomeration and re-entrainment of the particles are not taken into account and dust build up on the collectors is neglected. In addition, the flow of the flue gas entering the ESP is expected to be distributed equally between all the plate-to-plate spaces. We also assume zero space charge except in Section 9.2 where we specially devote to discussing the space charge related phenomena.

As found out in Section 7.6, the collection efficiency curve experiences a minimum around 0.4 μm, thus making the particles 0.4 μm in diameter the most interesting when combined saturation charging is assumed. For flue gas charged only by diffusion, the efficiency curve is always degressive and thus we concentrate on 0.1 μm particles describing the behavior around the probable mode of the particle size distribution curve for small-scale wood combustion flue gas. Furthermore, the consequences of low diffusion charge levels on larger particles is illustrated by 1 μm particle trajectories.

However, there is a problem in modeling of the trajectories of such a small particles. The memory and time consumption due to need for additional calculation steps increases due to which solutions might not be reached. The problem can be avoided by introducing a concept of 'equivalent velocity', discussed in detail in Appendix E.

9.1 Comparison of the Proposed ESP Configurations

To obtain better comparability, for both ESP configurations it is approximated that the precipitation stage occupies a space equal to the volume of a cube with edge length 0.3 m. The resulting mean flow velocities are estimated as was described in Section 6.3. Further, the simulations are performed by

utilizing the equivalence velocity principle described in Appendix E. Due to the discrepancy in the polarity of the electrodes in the two ESP cases, for rotating plate ESP the particles are assumed to be positively charged, whereas, the particulates arriving to the helicoidal precipitator are taken to carry negative charge. For simplicity we take negative ions to have the properties of positive ions, described in section 7.3.2, except that the charge is naturally opposite to that of positive ions.

9.1.1 The Rotating Plate ESP, 2D

The simplest way to model the rotating plate ESP (see Figure 2), described briefly in Section 3.3.2 and more in detail in Appendix C, is to reduce the consideration to inter-electrode space between one pair of plates. Assuming total cross-sectional area of $0.3 \times 0.3\ m^2$, implies, as justified in Section 6.3, the mean velocity $U_{mean} = 0.129556\ m/s$.

We are now ready to start the simulation and begin by modeling the trajectories of $0.4\ \mu m$ particles assuming combined saturation charging according to Cochet equation (57).

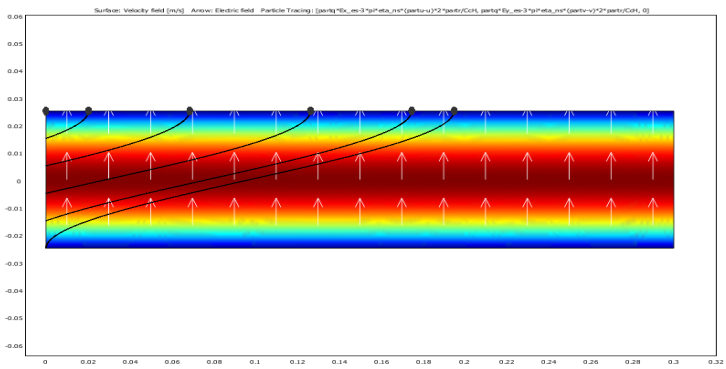

Figure 20: Particle tracing in the rotating plate ESP for $d_p = 0.4\ \mu m$ assuming combined charging yielding $Q_p = 27e$. Surface plot illustrates the velocity field with $U_{mean} \approx 0.13\ m/s$ and $U_{max} \approx 0.19\ m/s$, where red corresponds to maximum and blue to zero velocity. By the arrow plot the electric field direction is depicted. Simulation input parameters where $T = 130\ ^oC$, $p = 100\ kPa$, $e_r = 1.5$, $e_{r,air} = 1$, $U_{in,mean} = 0.129556\ m/s$, $\rho_{pa} = 450\ kg/m^3$, $s = 0.05\ m$ and $\Delta\phi = 20\ kV$.

As seen in the Figure 20, where the flow velocity field is illustrated by the surface plot and the arrow plot depicts the electric field, the particle trajectories are drawn as expected: the slope of the trajectory curves is steeper at blue area, close to the walls, where the flow velocity is lower, and flatter at red area, around the plate-to-plate centerline, where the flow

velocity is higher. Furthermore, simulation shows good correspondence with the prediction of the laminar model, Eq. (79). By solving for L, for $d_p = 0.4\ \mu m$, equation (79) implies plate length 0.195 m to be required for 100 % precipitation. This corresponds to x-coordinate of the end point of the lowest simulated 0.4 μm particle trajectory in the Figure 20. By reading from the Figure 20 we observe that the simulation predicts exactly the same result, 0.195 m, for needed plate length.

For comparison, in Figure 21 the trajectories of particles 0.4 μm in diameter are plotted taking the particulates to be charged only by diffusion charging as given by Source-and-Sink theory at $N_i t = 10^{12}\ s/m^3$. Taking a look at Figure 21 one observes that more than half of the 0.4 μm particles are not precipitated. This is expected, since the number of elementary charges carried by a particles proposed by Source-and-Sink theory is only 6, whereas for combined saturation charge the corresponding figure is 27.

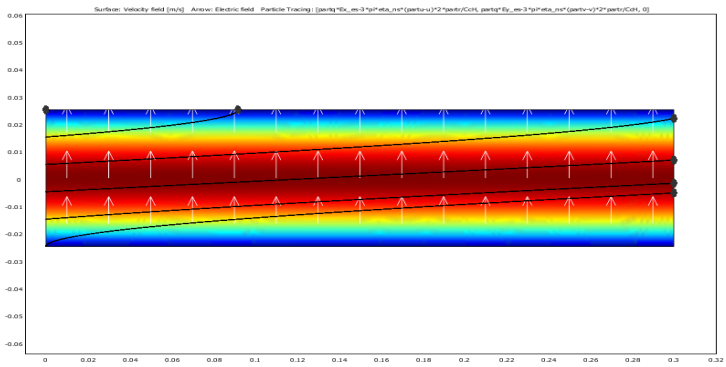

Figure 21: Particle tracing in the rotating plate ESP for $d_p = 0.4\ \mu m$, for which diffusion charging at $N_i t = 10^{12}\ s/m^3$ yields $Q_p = 6e$. Surface plot illustrates the velocity field with $U_{mean} \approx 0.13\ m/s$ and $U_{max} \approx 0.19\ m/s$, where red corresponds to maximum and blue to zero velocity. By the arrow plot the electric field direction is depicted. Simulation input parameters where $T = 130\ ^oC$, $N_i t = 10^{12}\ s/m^3$, $p = 100\ kPa$, $e_r = 1.5$, $e_{r,air} = 1$, $U_{in,mean} = 0.129556\ m/s$, $\rho_{pa} = 450\ kg/m^3$, $s = 0.05\ m$ and $\Delta\phi = 20\ kV$.

Let us then model the path lines for particles 0.1 μm in diameter, corresponding approximately to the mode of typical particle size distribution. Plot of 0.1 μm particle trajectories in Figure 22 points out that the conditions $N_i t = 10^{12}\ s/m^3$ are by no means sufficient for efficient particle precipitation, as was expected observing the Figure 15; a large fraction, almost a half, is not being captured.

Since the precipitation at $N_i t = 10^{12}\ s/m^3$ is insufficient, we raise the condition up to $N_i t = 10^{13}\ s/m^3$. The condition change implies an increase

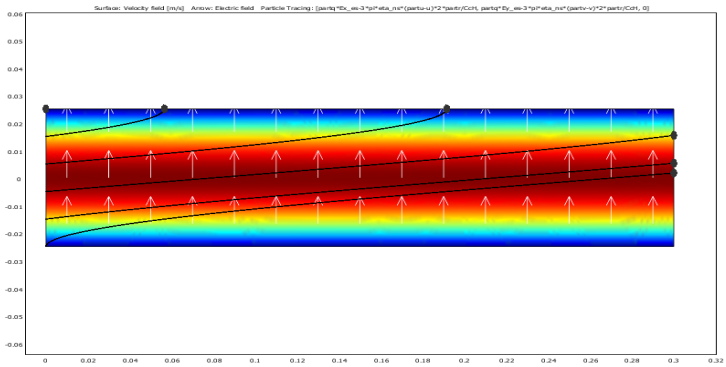

Figure 22: Particle tracing in the rotating plate ESP for $d_p = 0.1\ \mu m$, for which diffusion charging at $N_i t = 10^{12}\ s/m^3$ yields $Q_p = 1e$. Surface plot illustrates the velocity field with $U_{mean} \approx 0.13\ m/s$ and $U_{max} \approx 0.19\ m/s$, where red corresponds to maximum and blue to zero velocity. By the arrow plot the electric field direction is depicted. Simulation input parameters where $T = 130\ ^oC$, $p = 100\ kPa$, $e_r = 1.5$, $e_{r,air} = 1$, $U_{in,mean} = 0.129556\ m/s$, $\rho_{pa} = 450\ kg/m^3$, $s = 0.05\ m$ and $\Delta\phi = 20\ kV$.

in charge level from $1e$ to $4e$ for $0.1\ \mu m$ particulates. The corresponding path lines are illustrated in Figure 23 suggesting that ion concentration residence time product $N_i t = 10^{13}\ s/m^3$ provides sufficient charging environment for successful precipitation around the size distribution mode. The plate length required for 100 % collection can be compared to result given by Eq. (79), again obtaining equal result, $0.136m$, with both the methods. However, for larger particles the charge level acquired even at $N_i t = 10^{13}\ s/m^3$ is not high enough. This is demonstrated in Figure 24 for particulates $1\ \mu m$ in diameter. One finds that particles with the longest distance to travel in the inter-electrode-space no longer reach the collector, as intended. Fortunately, the particles as large as $1\ \mu m$ are quite rare in small-scale wood combustion flue gases, implying that $N_i t = 10^{13}\ s/m^3$ charging condition might actually lead to satisfactory precipitation. In addition, as a consequence of excellent correspondence with laminar model, we conclude that our simulations should give reliable results, at least for laminar flows, as is further confirmed in Figure 25 where collection length needed (as solved from Eq. (79)) is plotted against particle diameter for Cochet combined charging (57) and for $N_i t = 10^{12}\ s/m^3$ and $N_i t = 10^{13}\ s/m^3$ diffusion charging.

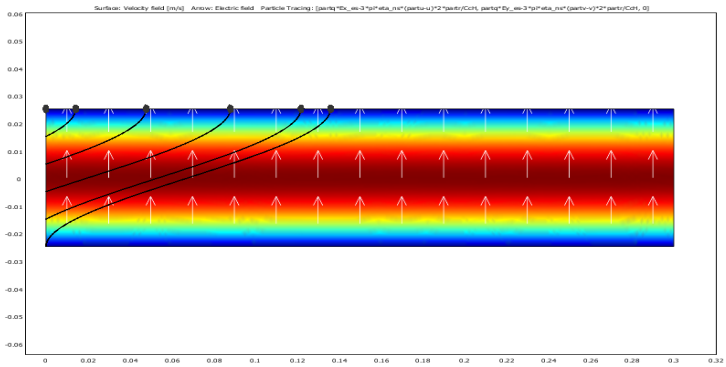

Figure 23: Particle tracing in the rotating plate ESP for $d_p = 0.1\ \mu m$, for which diffusion charging at $N_i t = 10^{13}\ s/m^3$ yields $Q_p = 4e$. Surface plot illustrates the velocity field with $U_{mean} \approx 0.13\ m/s$ and $U_{max} \approx 0.19\ m/s$, where red corresponds to maximum and blue to zero velocity. By the arrow plot the electric field direction is depicted. Simulation input parameters where $T = 130\ ^oC$, $p = 100\ kPa$, $e_r = 1.5$, $e_{r,air} = 1$, $U_{in,mean} = 0.129556\ m/s$, $\rho_{pa} = 450\ kg/m^3$, $s = 0.05\ m$ and $\Delta\phi = 20\ kV$.

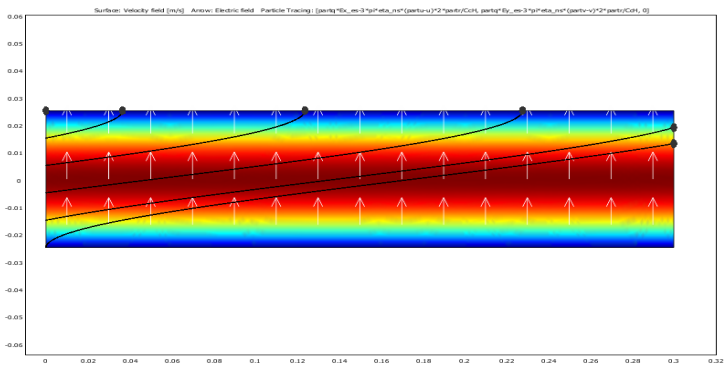

Figure 24: Particle tracing in the rotating plate ESP for $d_p = 1\ \mu m$, for which diffusion charging at $N_i t = 10^{13}\ s/m^3$ yields $Q_p = 50e$. Surface plot illustrates the velocity field with $U_{mean} \approx 0.13\ m/s$ and $U_{max} \approx 0.19\ m/s$, where red corresponds to maximum and blue to zero velocity. By the arrow plot the electric field direction is depicted. Simulation input parameters where $T = 130\ ^oC$, $p = 100\ kPa$, $e_r = 1.5$, $e_{r,air} = 1$, $U_{in,mean} = 0.129556\ m/s$, $\rho_{pa} = 450\ kg/m^3$, $s = 0.05\ m$ and $\Delta\phi = 20\ kV$.

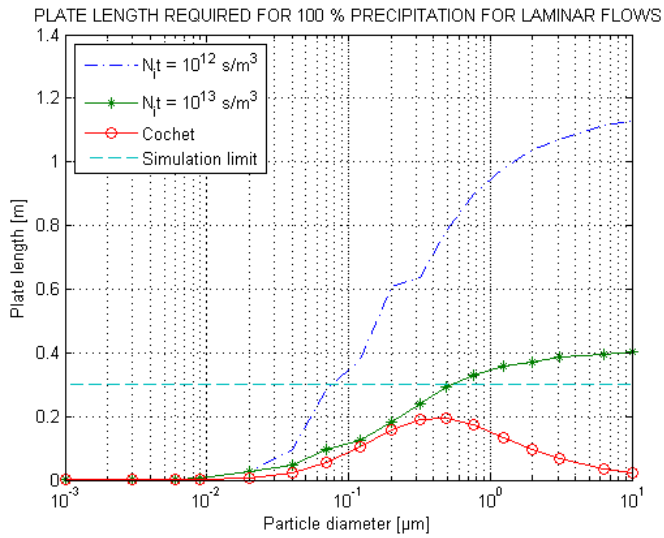

Figure 25: The maximum collection length under various charging conditions.

9.1.2 The Rotating Plate ESP, 3D

In the three-dimensional case for the rotating plate ESP we consider the conditions between two round plates, mounted on an axle, and a pair of wiper blades in contact with the plates (see Fig. 26). The calculation domain is the meshed area in Figure 26, whereas the hollow spaces correspond to the axle and the blades, respectively.

The total inlet area is now reduced to $0.3 \times 0.2\ m^2$, giving $0.19\ m/s$ for the mean velocity, that is set at the inlet as normal flow velocity. Therefore, in 3D the parabolic velocity profile used in 2D is not employed. As a consequence of the slightly higher mean velocity, the plate wise distances traveled by the particulates are increased, as seen from the simulation results depicted in Figures 27 and 28, for 0.1 μm particles.

The collection length required is around 0.17 m depending on the inlet position, when it was 0.14 m in 2D. This is interpreted to be mostly due to the raise in the mean velocity. Further, we observe from the Figure 28 that behind the axle there is low velocity region formed, which was, though, expected.

Most importantly the presence of the wiper blades does not disturb the velocity field too much, as can be determined by observing that the gas flow field is nearly similar at both the bladed and non-bladed sides of the axle, as depicted in Figure 28. Consequently, the idea of the rotating plate ESP, based on the information provided by this 3D model, seems feasible.

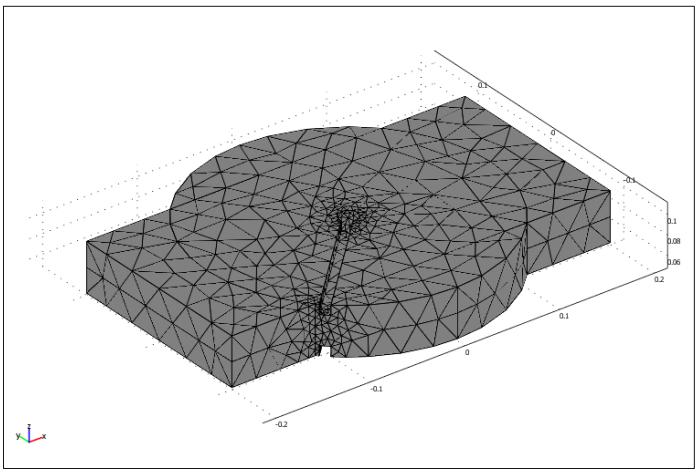

Figure 26: Illustration of simplified 3D model of rotating plate ESP with calculation domain meshed.

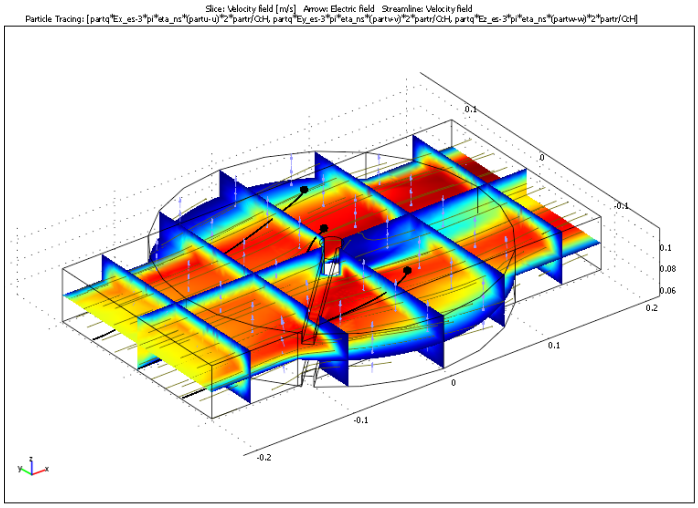

Figure 27: Particle tracing in the rotating plate ESP for $d_p = 0.1\ \mu m$. Slice plot illustrates the velocity field with $U_{mean} \approx 0.19\ m/s$ and $U_{max} \approx 0.34\ m/s$, where red corresponds to maximum velocity and blue to zero. By the arrow plot the direction of the electric field is depicted. Simulation input parameters where $T = 130\ ^oC$, $N_it = 10^{13}\ s/m^3$, $p = 100\ kPa$, $e_r = 1.5$, $e_{r,air} = 1$, $U_{in} = 0.19\ m/s$, $\rho_{pa} = 450\ kg/m^3$, $s = 0.05\ m$ and $\Delta\phi = 20\ kV$.

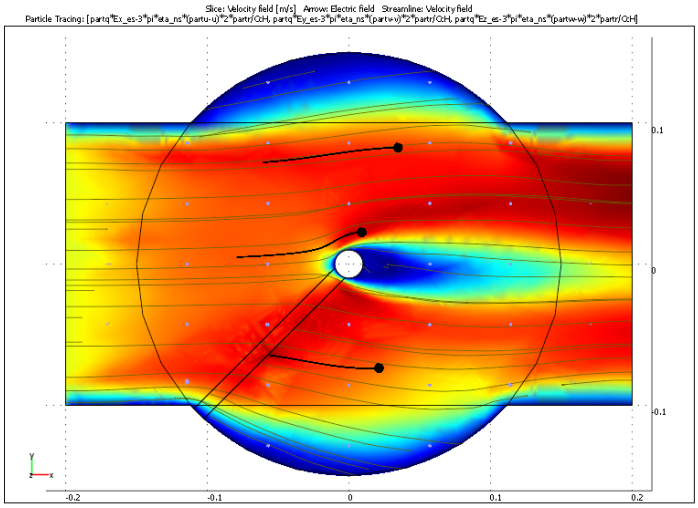

Figure 28: Particle tracing in the rotating plate ESP for $d_p = 0.1\ \mu m$. Top view of the Figure 27. Simulation input parameters where $T = 130\ ^oC$, $N_it = 10^{13}\ s/m^3$, $p = 100\ kPa$, $e_r = 1.5$, $e_{r,air} = 1$, $U_{in} = 0.19\ m/s$, $\rho_{pa} = 450\ kg/m^3$, $s = 0.05\ m$ and $\Delta\phi = 20\ kV$.

9.1.3 The Helicoidal Type ESP, 2D

Maybe the simplest way to get a realistic grasp of modeling helicoidal geometry would be to apply a flow on 2D helicoid surface in three dimensional space. Unfortunately Comsol does not support flows on such surfaces and less convenient approach must be found out. In this paper the flow fields inside the coaxial cross sections are not actually simulated but the initial condition of parabolic radial velocity profile is assumed to hold in time. This allows for particle trajectory modeling of multiple rounds in plane, however, neglecting the probable distortion of the velocity field due to inertia of the fluid particles in the central field and the vicinity of the outlet might cause some error.

The helicoidal ESP comprises of two helicoids mounted within each other (see Figure 1). The wider and grounded one forms a part of the flow channel walls and is not seen in the cross-sectional view illustrated in Figure 29, whereas the more narrow one at negative potential, is the observed, not meshed, band inside the meshed area. Modeling of the helicoidal geometry in 2D is thus performed simulating the particle trajectories in an imaginary cross-section of the helix projected to a plane. When projected to a plane, the narrow helix divides the flow channel into two regions, and as a consequence we divide the calculation domain into two individual cases, and model the

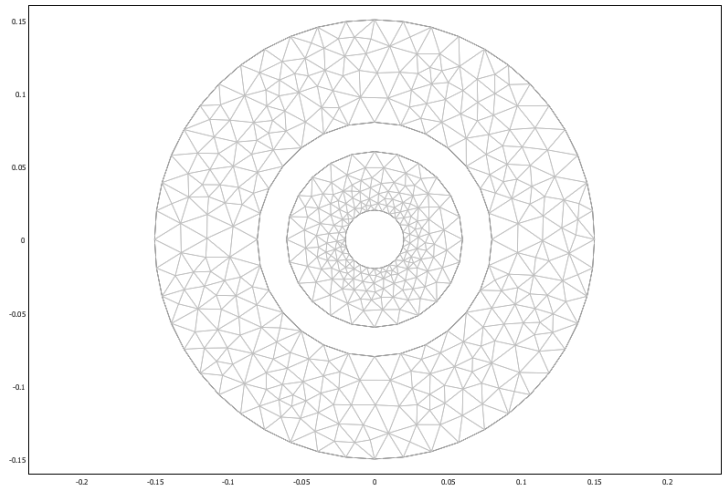

Figure 29: Approximate Cross-sectional view of the helicoidal ESP projected to a 2D plane. The meshed calculation domain is further split into inner and outer region divided by the narrow helix.

inner and outer side of the narrow helix separately.

Approximate volume assumption of $\pi \cdot (0.15\ m)^2 \cdot 0.3\ m$ is realized by an obvious choice for wider helicoid outer radius of 0.15 m and height of 0.3 m, for three round flow channel. This gives for an approximate cross-sectional area of the flow channel $A \approx (0.15 \times 0.10)\ m^2 \approx 0.015\ m^2$, implying $U_{mean} = 0.777\ m/s$.

We now simulate the trajectories for 0.1 μm and 1 μm particles, at $N_i t = 10^{13}\ s/m^3$, inside and outside of the narrow helix. Taking a look at Figures 30 and 31 one observes that in the inner region the 0.1 μm particles get collected after approximately two rounds and one quadrant, whereas the particulates 1 μm in diameter require more than six rounds to end up captured. The behavior is similar to that observed in the rectangular flow field; the 0.1 μm particles around the mode of the particle size distribution get collected acceptably, but for the larger 1 μm particles serious leakage occurs.

In the outer region the 0.1 μm particles get collected as in the inner region, that is, two rounds and one quadrant is required for their capture (see Figure 32). However, for larger particles the helicoidal ESP suffers from particle escape in the outer region as well, as depicted in Figure 33.

Furthermore, in Figure 34 we show that the centrifugal force plays insignificant role in small-scale wood combustion flue gas precipitation. Figure

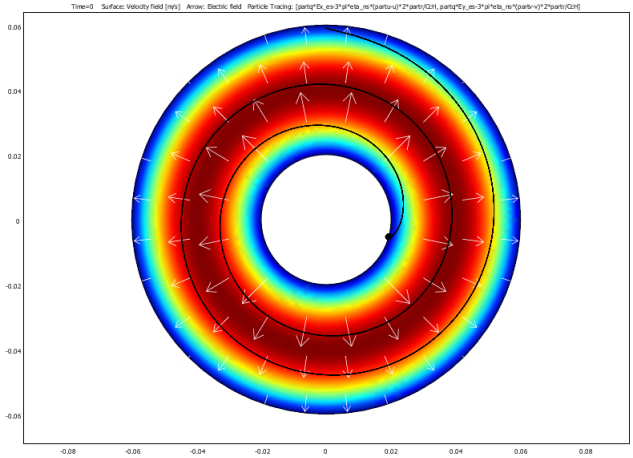

Figure 30: Particle tracing for $d_p = 0.1\ \mu m$ in the helicoidal ESPs inner region. Surface plot illustrates the velocity field with $U_{mean} \approx 0.78\ m/s$ and $U_{max} \approx 1.17\ m/s$, where red corresponds to maximum and blue to zero velocity. By the arrow plot the electric field is depicted. Simulation input parameters where $T = 130\ ^oC$, $N_it = 10^{13}\ s/m^3$, $p = 100\ kPa$, $e_r = 1.5$, $e_{r,air} = 1$, $U_{in,mean} = 0.78\ m/s$, $\rho_{pa} = 450\ kg/m^3$, $s = 0.05\ m$ and $\Delta\phi = 20\ kV$.

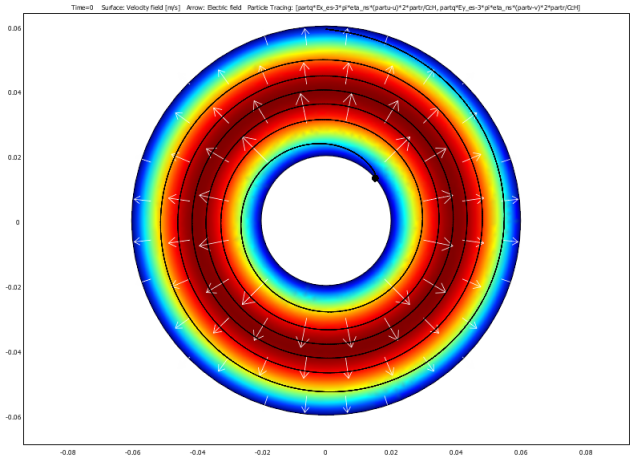

Figure 31: Particle tracing for $d_p = 1\ \mu m$ in the helicoidal ESPs inner region. Surface plot illustrates the velocity field with $U_{mean} \approx 0.78\ m/s$ and $U_{max} \approx 1.17\ m/s$, red corresponding to maximum and blue to zero velocity. By the arrow plot the electric field is depicted. Simulation input parameters where $T = 130\ ^oC$, $N_it = 10^{13}\ s/m^3$, $p = 100\ kPa$, $e_r = 1.5$, $e_{r,air} = 1$, $U_{in,mean} = 0.78\ m/s$, $\rho_{pa} = 450\ kg/m^3$, $s = 0.05\ m$ and $\Delta\phi = 20\ kV$.

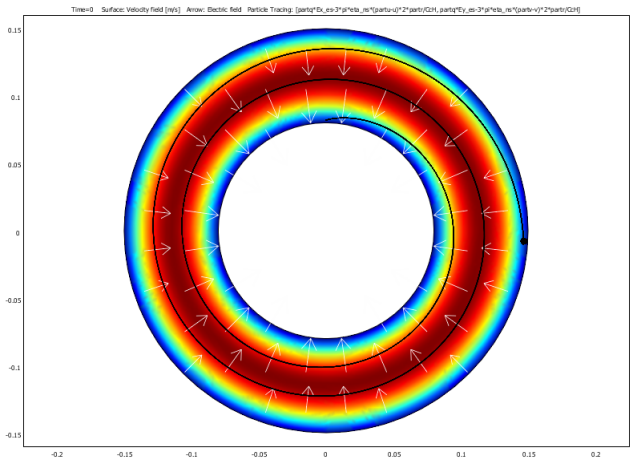

Figure 32: Particle tracing for $d_p = 0.1\ \mu m$ in the helicoidal ESPs outer region. Surface plot illustrates the velocity field with $U_{mean} \approx 0.78\ m/s$ and $U_{max} \approx 1.17\ m/s$, red corresponding to maximum and blue to zero velocity. By the arrow plot the electric field is depicted. Simulation input parameters where $T = 130\ ^oC$, $N_it = 10^{13}\ s/m^3$, $p = 100\ kPa$, $e_r = 1.5$, $e_{r,air} = 1$, $U_{in,mean} = 0.78\ m/s$, $\rho_{pa} = 450\ kg/m^3$, $s = 0.05\ m$ and $\Delta\phi = 20\ kV$.

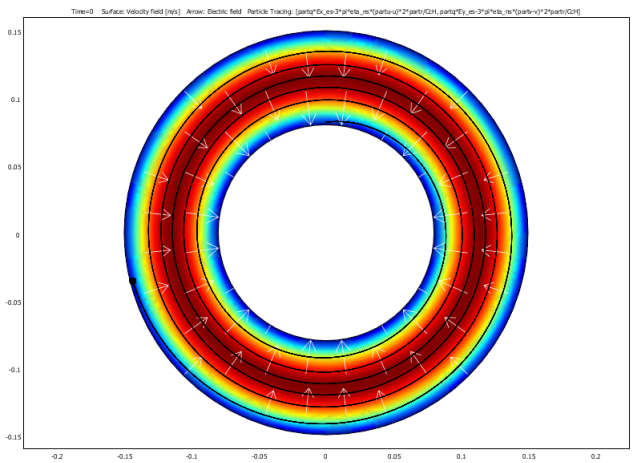

Figure 33: Particle tracing for $d_p = 1\ \mu m$ in the helicoidal ESPs outer region. Surface plot illustrates the velocity field with $U_{mean} \approx 0.78\ m/s$ and $U_{max} \approx 1.17\ m/s$, red corresponding to maximum and blue to zero velocity. By the arrow plot the electric field is depicted. Simulation input parameters where $T = 130\ ^oC$, $N_it = 10^{13}\ s/m^3$, $p = 100\ kPa$, $e_r = 1.5$, $e_{r,air} = 1$, $U_{in,mean} = 0.78\ m/s$, $\rho_{pa} = 450\ kg/m^3$, $s = 0.05\ m$ and $\Delta\phi = 20\ kV$.

34 well illustrates that even for particles 10 μm in diameter the centrifugal force is still approximately one order of magnitude smaller than the electrical force at $E \in [9.1, 2.1] \cdot 100\ kV/m$ and $N_i t = 10^{13}\ s/m^3$. Majority of the said flue gas particulates are smaller than 1 μm [11, 8]. This confirmes the result of the simulations, *i.e.*, the helicoidal ESP does not suffer from efficiency decrease due to the centrifugal force with opposite direction to that of the electrical force.

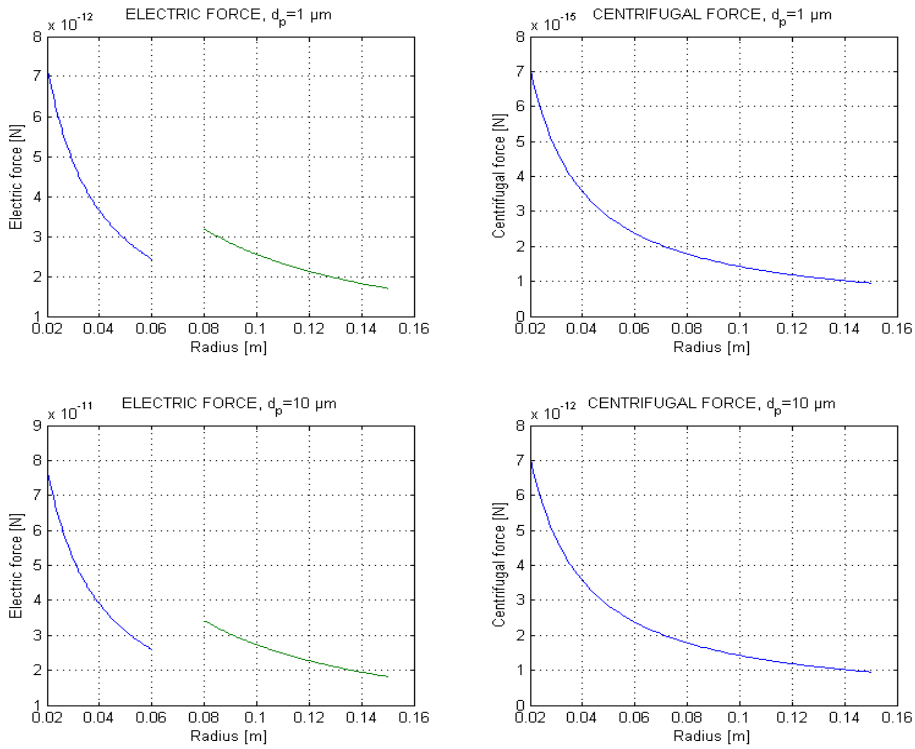

Figure 34: Electric force compared to centrifugal force for 1 μm and 10 μm particles, with corresponding charge levels $50e$ and $535e$, density 450 kg/m^3 at $E \in [9.1, 2.1] \cdot 100\ kV/m$. The gaps in the left hand side curves correspond to the space occupied by the narrow helicoid (in 2D projection consideration).

9.1.4 The Helicoidal Type ESP, 3D

For helicoidal ESP, 3D model was constructed as in the case of the rotating plate ESP. The simplified geometry illustrated in Figure 35 was created with a CAD tool, Autodesk Inventor 2009, and imported to COMSOL. The calculation domain is the meshed area seen in Figure 35.

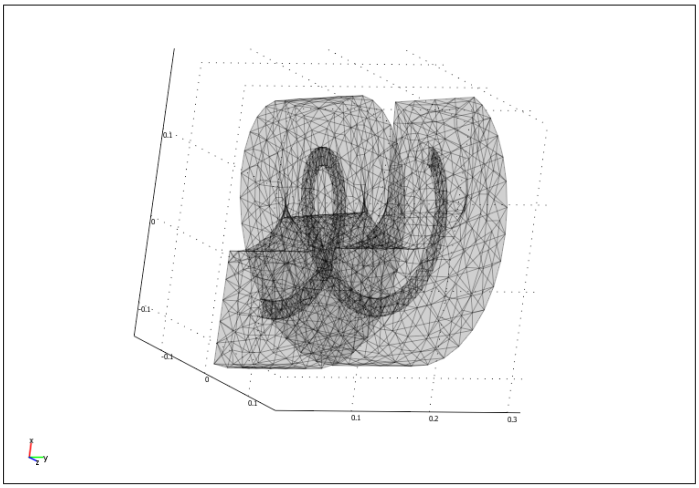

Figure 35: Part of the flow channel of the helicoidal ESP in 3D. The calculational domain is seen meshed.

Unfortunately, due to the dense mesh required, the number of degrees of freedom increases and consequently the available memory was not sufficient. Therefore, no results can be presented for the model of the 3D helicoid.

9.2 Influence of the Space Charge Density

9.2.1 Constant Space Charge Density

The influence of space charge on ESP performance is studied considering only the contribution of the particles, not that of the gas ions which is taken to be negligible due their high migration velocity and lack of sources in the plate-to-plate space. Particle space charge density $\rho_{p,i}$ is calculated by simply multiplying the particle number density $c(d_i)$ and particle charge $Q_p(d_i)$ corresponding to i^{th} ELPI interval. Therefore the total space charge density was obtained by summation over all the channels i:

$$\rho_s = \sum_i Q_p(d_i) \cdot c_i. \tag{86}$$

Particle size distribution, plotted in Figure 37, is based on the experimental data from the MiniDust ELPI measurements corresponding to 'bad' combustion conditions. The time interval $t \in [13.10.04 - 14.09.59]$, from the illustrated concentration chart depicted in Figure 36, was chosen to exclude the highest concentration peak, probably corresponding to lab equipment

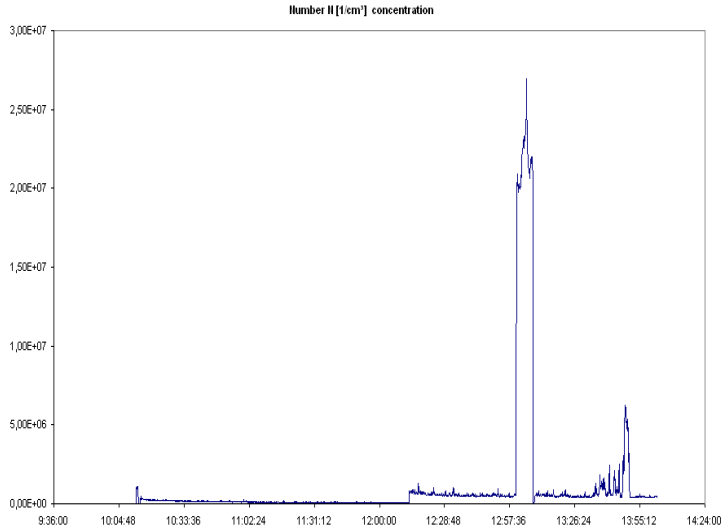

Figure 36: Number concentration chart

adjustments or cleaning, including though, the smaller fluctuations observed at right hand side tail of the plot. Furthermore, the space charge density distribution, illustrated also in Figure 37, is calculated assuming diffusion charging as yielded by the Source-and-Sink theory, at $N_i t = 10^{13}\ s/m^3$ and $T = 130\ ^oC$. It is to be noted that in Figure 37 the y-axis values are normalized by the length of the ELPI channel widths.

Evaluating the particle space charge as a sum over the diameter intervals corresponding to 12 ELPI channels, for number density vector[5] c_i with correspondent channel mean diameter vector[6] d_i, we thus obtain for total particle space charge density

$$\rho_s = \sum_{i=1}^{12} Q_p(d_i) \cdot c_i = 7.15 \cdot 10^{-7}\ C/m^3.$$

Introducing the obtained space charge[7] $\rho_s = 7.15 * 10^{-7}\ C/m^3$ to the Poisson's equation (11), it is now possible to provide the first estimate of the effect of the space charge on the particle trajectories in an ESP.

The result presented in Figure 38 describes the fact that the space charge densities of order $10^{-7}\ C/m^3$ have practically no impact on particle migration

[5] $c_i = [2.82 \cdot 10^{10}\ 4.83 \cdot 10^{10}\ 1.63 \cdot 10^{11}\ 2.76 \cdot 10^{11}\ 1.6 \cdot 10^{11}\ 4.91 \cdot 10^{10}\ 8.1 \cdot 10^{9}\ 6.94 \cdot 10^{8}\ 2.46 \cdot 10^{8}\ 1.04 \cdot 10^{8}\ 6.38 \cdot 10^{7}\ 2.44 \cdot 10^{7}]\ \#/m^3$

[6] $d_i = [0.02\ 0.04\ 0.07\ 0.12\ 0.2\ 0.32\ 0.49\ 0.76\ 1.23\ 1.96\ 3.1\ 6.32]\ \mu m$

[7] Assuming combined saturation charge would yield $\rho_s = 1.0447 * 10^{-6}\ C/m^3$

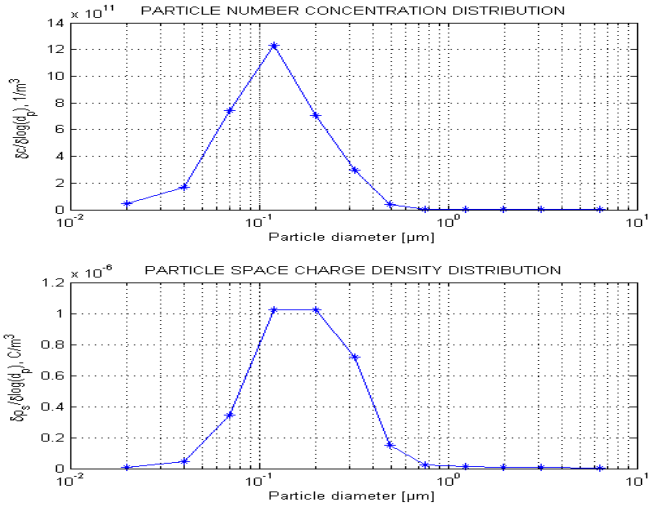

Figure 37: Particle number density and space charge density distributions. Number density and particle charge correspond to MiniDust data and average charges obtained with the Source-and-Sink method, respectively.

in the domain studied (for comparison, see Figure 23). This can be explained by the modest size of the electric field fluctuations $4.02 \cdot 10^5 - 3.98 \cdot 10^5\ V/m$, caused by the space charge and being only approximately 1 % of the primary electric field strength $4 \cdot 10^5\ V/m$ induced by the applied potential difference.

An intuitive guess would be that the magnitude of the electric field strength fluctuation caused by inter electrode space charge should be of the same order of magnitude than the primary field strength. Since above only about 1 % fluctuation was obtained, we guess that a more significant impact is caused by employing $\rho_s = 7.15 \cdot 10^{-5}\ C/m^3$, that is two orders of magnitude higher than in the case shown in Figure 38.

From Figure 39 it can be seen that the increase of space charge density up to $\rho_s = 7.15 \cdot 10^{-5}\ C/m^3$, corresponding to peak number concentrations of about $10^{13}\ 1/m^3$, i.e., similar to those reported in [19] and [11] for small scale wood combustion, causes small but not too significant changes to the required collection distances.

By increasing the space charge density once more, now up to $5 \cdot 7.15 \cdot 10^{-5}\ C/m^3 \approx 3.6 \cdot 10^{-4}\ C/m^3$, an interesting and essential phenomenon is seen. As depicted in Figure 40, the inter-electrode electric field of strength 400 kV/m becomes partially overshadowed by the electric field generated by the space charge, leading to change of direction of the field near the grounded plate. As a consequence, particles introduced into the flow below this limit

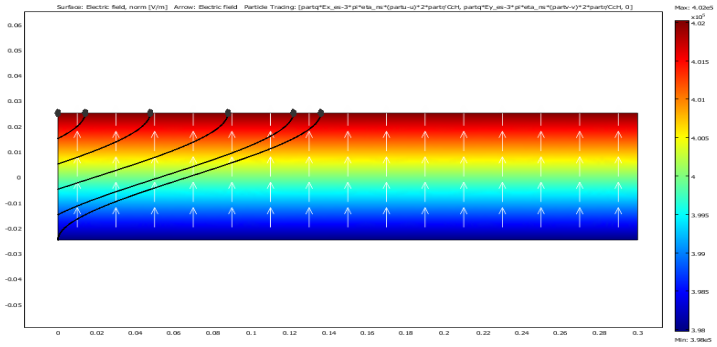

Figure 38: Particle tracing in a plate type ESP for $d_p = 0.1\ \mu m$. Electric field strength and direction are illustrated by the surface plot and the arrow plot, respectively. Simulation input parameters where $\rho_s = 7.15{\cdot}10^{-7}\ C/m^3$, $N_it = 10^{13}\ s/m^3$, $T = 130\ ^oC$, $p = 100\ kPa$, $e_r = 1.5$, $e_{r,air} = 1$, $U_{in,mean} = 0.129556\ m/s$, $\rho_{pa} = 450\ kg/m^3$, $s = 0.05\ m$ and $\Delta\phi = 20\ kV$.

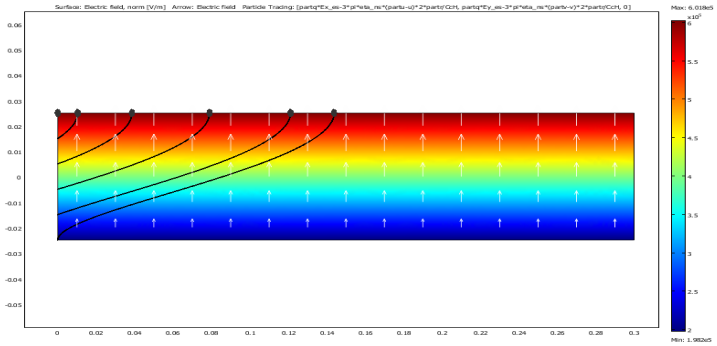

Figure 39: Particle tracing in a plate type ESP for $d_p = 0.1\ \mu m$. Electric field strength and direction are illustrated by the surface plot and the arrow plot, respectively. Simulation input parameters where $\rho_s = 7.15{\cdot}10^{-5}\ C/m^3$, $N_it = 10^{13}\ s/m^3$, $T = 130\ ^oC$, $p = 100\ kPa$, $e_r = 1.5$, $e_{r,air} = 1$, $U_{in,mean} = 0.129556\ m/s$, $\rho_{pa} = 450\ kg/m^3$, $s = 0.05\ m$ and $\Delta\phi = 20\ kV$.

of change of the field direction can not overcome the potential barrier created and end up 'reversely collected'. Here reverse collection appears as an artificial phenomenon due 'stick to boundary' condition set for particle tracing – In a real ESP the situation would be more complicated. The particle trajectories are also shifted above the limit of field direction change. The particles, and thus the space charge, are of positive polarity. Therefore, on one hand, the particles released into the flow above the plate-to-plate centerline, sense more space charge originated repulsion from below than from above, thus increasing the net upwards force, and the plate length required for collection reduces. On the other hand, though, the particles released below the centerline, and above the limit of the field direction change, sense more repulsion from above, and consequently, more collection length is needed. Therefore, we conclude that the effect of sufficiently high space charge densities have negative impact on ESP performance.

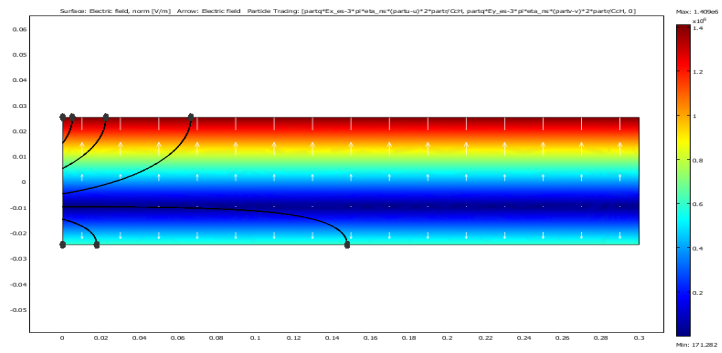

Figure 40: Particle tracing in a plate type ESP for $d_p = 0.1\ \mu m$. Electric field strength and direction are illustrated by the surface plot and the arrow plot, respectively. Simulation input parameters where $\rho_s = 3.75 \cdot 10^{-4}\ C/m^3$, $N_i t = 10^{13}\ s/m^3$, $T = 130\ ^oC$, $p = 100\ kPa$, $e_r = 1.5$, $e_{r,air} = 1$, $U_{in,mean} = 0.129556\ m/s$, $\rho_{pa} = 450\ kg/m^3$, $s = 0.05\ m$ and $\Delta\phi = 20\ kV$.

9.2.2 Turbulent Space Charge Profile

To mimic the case of turbulent flow conditions we employ the model of exponential reduction, Eq. (81), that assumes the aerosol to be composed of particles from the 12 size classes corresponding to the ELPI channels.

The particle trajectories, as seen in Figure 41, point out the fact that the space charge densities of magnitude $\rho_s = 7.15 \cdot 10^{-7}\ C/m^3$, corresponding to the MiniDust measurements, have practically no impact on particle migration

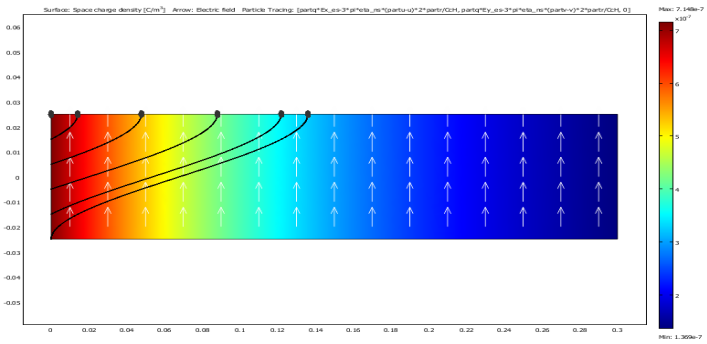

Figure 41: Particle tracing in a plate type ESP for $d_p = 0.1\ \mu m$. Space charge density and electric field direction are illustrated by the surface plot and the arrow plot, respectively. Simulation input parameters where $\rho_{s,inlet} = 7.15 * 10^{-7}\ C/m^3$, $L = 0.3\ m$, $N_it = 10^{13}\ s/m^3$, $T = 130\ ^oC$, $p = 100\ kPa$, $e_r = 1.5$, $e_{r,air} = 1$, $U_{in,mean} = 0.129556\ m/s$, $\rho_{pa} = 450\ kg/m^3$, $s = 0.05\ m$ and $\Delta\phi = 20\ kV$.

in an ESP when model of exponential reduction is applied, as was expected from the constant profile results seen in Figure 38.

To obtain better comparability to the constant profile results, space charge density is raised up to $\rho_{s,inlet} = 3.75 * 10^{-4}\ C/m^3$. It is observed from Figure 42 that we again arrive to such high densities that the limit of reversed electric field direction appears. Now, though, by comparison of results presented in Figures 42 and 40, we notice that the limit of change of field direction bends downwards for exponential profile, thus reducing the area of the zone of reversed electric field. This leads to conclusion that employing the exponential profile implies better ESP performance as can be found out by comparison of the particle trajectories as well. Since particle collection from the flow indeed takes place, the exponential model ought to be more realistic than the model assuming constant profile, that leads us to underestimate the performance of the ESP.

9.2.3 Laminar Space Charge Profile

As was done for the exponential profile in the previous section, corresponding to turbulent flow conditions, in this section as well, we employ for the laminar flow space charge composed of 12 size classes corresponding to the 12 ELPI channels, thus taking into account the particle size dependence of the migration characteristics.

As noticed for constant and exponential profiles, space charge densities of magnitude of $\rho_{s,inlet} = 7.15 \cdot 10^{-7}\ C/m^3$ have no impact on ESP perfor-

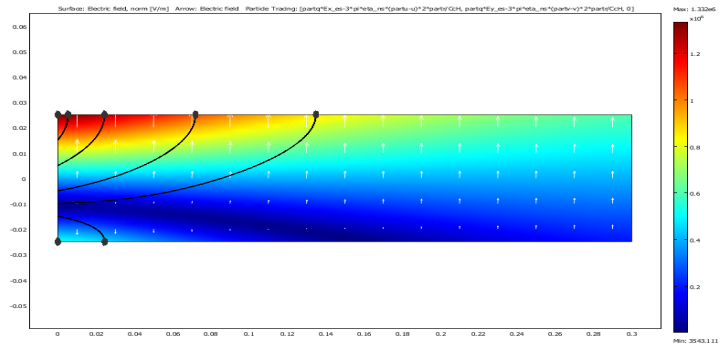

Figure 42: Particle tracing in a plate type ESP for $d_p = 0.1\ \mu m$. Electric field strength and direction are illustrated by the surface plot and the arrow plot, respectively. Simulation input parameters where $\rho_{s,inlet} = 3.75 * 10^{-4}\ C/m^3$, $N_it = 10^{13}\ s/m^3$, $T = 130\ ^oC$, $p = 100\ kPa$, $e_r = 1.5$, $e_{r,air} = 1$, $U_{in,mean} = 0.129556\ m/s$, $\rho_{pa} = 450\ kg/m^3$, $s = 0.05\ m$ and $\Delta\phi = 20\ kV$.

mance, as confirmed again in Figure 43. Further, by the surface plot the space charge profile, fractioned to 12 subdomains, demonstrates descending behavior towards the outlet and the grounded plate. Outside of the area occupied by the 12 fractions the space charge density is zero independent of y.

Again, when the space charge density inlet value is increased up to $\rho_{s,inlet} = 3.75 * 10^{-4}\ C/m^3$, we observe that the limit of field direction change appears. Now comparing Figures 44 and 42, one finds out that the said limit is not that bended for laminar than for exponential profile, but the area of reversed field reduces. The shorter life time of the particles in the plate-to-plate space (compared to the turbulent flow) implies reduced space charge residence area leading to reduced area of reversed electric field.

However, an important observation is made. As the flow proceeds plate wise the zero space charge domain begins to form. This means for any particle that it senses less space charge originated repulsion from below than from above compared to the situation in which the space charge density in direction perpendicular to the plates was evenly distributed. It follows that a flow with turbulent mixing is more advantageous than laminar flow if only space charge effect is considered. The phenomenon is the best illustrated by the trajectories of the particles released to the flow as third from the lower plate in Figures 42 and 44.

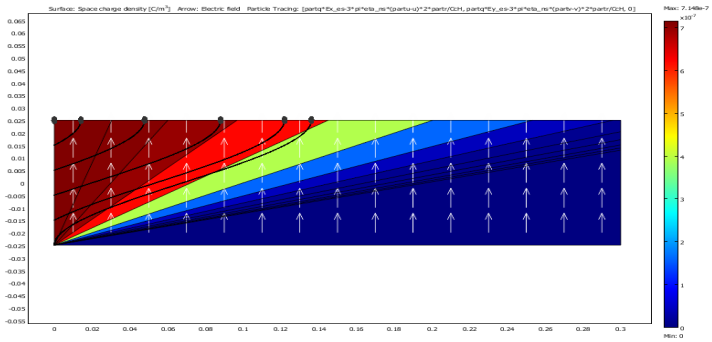

Figure 43: Particle tracing in a plate type ESP for $d_p = 0.1\ \mu m$. Space charge density and electric field direction are illustrated by the surface plot and the arrow plot, respectively. Simulation input parameters where $\rho_{s,inlet} = 7.15 * 10^{-7}\ C/m^3$, $N_it = 10^{13}\ s/m^3$, $T = 130\ ^oC$, $p = 100\ kPa$, $e_r = 1.5$, $e_{r,air} = 1$, $U_{in,mean} = 0.129556\ m/s$, $\rho_{pa} = 450\ kg/m^3$, $s = 0.05\ m$ and $\Delta\phi = 20\ kV$.

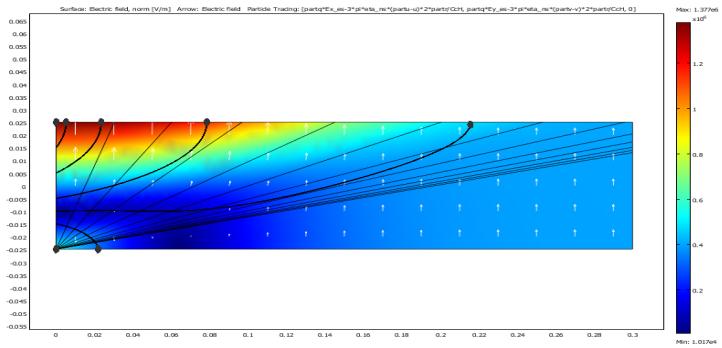

Figure 44: Particle tracing in a plate type ESP for $d_p = 0.1\ \mu m$. Electric field strength and electric field direction are illustrated by the surface plot and the arrow plot, respectively. Simulation input parameters where $\rho_{s,inlet} = 3.75 * 10^{-4}\ C/m^3$, $T = 130\ ^oC$, $p = 100\ kPa$, $e_r = 1.5$, $e_{r,air} = 1$, $U_{in,mean} = 0.129556\ m/s$, $\rho_{pa} = 450\ kg/m^3$, $s = 0.05\ m$ and $\Delta\phi = 20\ kV$.

10 Conclusions

The goal of this thesis was to develop a mathematical model for two-stage electrostatic precipitators, to be especially applied to small-scale wood combustion flue gas after treatment. Utilizing Comsol 3.4 commercial software, fluid dynamics was modeled employing the incompressible Navier-Stokes equation, whereas the electric field was solved from Poisson equation for electric potential. Finally, the particle trajectory analysis in the said overlapping gas velocity and electric field was used to to draw the conclusions.

An ESP for which the model is valid was taken to comprise of two separate stages, the first for particle charging and the second for particle precipitation. It was of interest to discover whether it would be reasonable to build an ESP with no ion source in the precipitation stage. The said omitting of an ion source would be a simplification probably implying ion escape to the collectors at the immediate vicinity of the precipitation stage inlet leading to disappearance of the contribution of field charging. Consequently, particle charging was studied assuming, firstly and primarily diffusion charging, and secondly combined charging. Due to lack of a proper analytical particle diffusion charging theory for transition regime, $d_p \approx \lambda$, the numerically solvable Source-and-Sink method was employed.

The results obtained using the Source-and-Sink theory underline that for particles smaller than 0.1 μm the fraction of particles carrying no charge at all is of increasing importance at $N_i t = 10^{12}\ s/m^3$. In addition, accompanied separately with both analytical equations and the simulations, the theory yields that the particle charge levels at $N_i t = 10^{12}\ s/m^3$ become too low for satisfactory precipitation for particles bigger than 0.1 μm, while at $N_i t = 10^{13}\ s/m^3$ small-scale precipitation requirements are met decently at least up to 1 μm. The too low charge levels of larger particles was expected since diffusion charging is known to dominate for particles smaller than 0.1 μm, whereas for $d_p > 1\ \mu m$ field charging is the predominant method. Assuming combined charging up to saturation implies relatively good precipitation for all the particle sizes, yet some problems might be encountered around the 0.4 μm electrical mobility minimum.

In the flow velocity region studied, i.e., $U_{mean} < 1\ m/s$, the simulation results demonstrate excellent correspondence to the prediction for the plate length required for particle capture by analytical laminar collection efficiency equation. For 0.1 μm particles, characterizing the mode of a typical particle size distribution, the plate length required for collection was found to be 0.14 m at $N_i t = 10^{13}\ s/m^3$, $T = 130\ ^oC$ and $E = 400\ kV/m$ for flow velocity 0.13 m/s, corresponding to 0.012 m^3/s. Such a collection distance implies dimensions indeed feasible for small combustion appliances.

The importance of the space charge originated electric field deformation was studied for constant profile and exponential and laminar evolution. The space charge density $\rho_s = 7.15 \cdot 10^{-7}\ C/m^3$ corresponding to total particle number concentration $c = 7.34 \cdot 10^{11}\ 1/m^3$, obtained from MiniDust data, was found to have no impact on ESP performance independent of the profile applied. Furthermore, the hypothetical increase in space charge density yielded slight increase in required collection length for $\rho_s \approx 10^{-5}\ C/m^3$, whereas for $\rho_s \approx 10^{-4}\ C/m^3$ a reversed electric field domain and potential barrier, that the particles can not overcome, is established. The relative perturbation is naturally dependent of the external electric field applied, which in our case was 400 kV/m.

For $\rho_s \approx 10^{-4}\ C/m^3$, implementing the constant profile was noticed to be the most valid for the worst case scenario assessments, while the exponential plate wise reduction gave the best precipitation results. For significant space charge densities the evolution of the particle trajectories and the charge cloud created by the particles themselves is simultaneous, or rather the same thing, and was not taken into account in the scope of this thesis. Consequently, the results by no means can interpreted rigorously, yet supposedly they can be taken to possess some indicative value.

The proposed helical ESP structure was studied modeling the particle trajectories in geometry constructed projecting the structure's cross section into a 2D plane. Particular difference in precipitation behavior compared to a plate type ESP was not found out, though higher flow velocities in helical configuration might imply more turbulent flows leading to increased re-entrainment. The most important factor in the dimensioning of an ESP is therefore supposedly its volume, not the length of the precipitation channel, provided that the gas spreads evenly to every between-the-plates domain.

For both the configurations proposed simple 3D geometries were constructed mainly to demonstrate the wider applicability of the mathematical model. The modest hardware that was available limited the simulation to these simple examples requiring calculation time of order of hours. For simulations in larger geometries the memory available was not sufficient. For the rotating plate type ESP 3D model the results suggested that the wiper blades did not interfere the gas flow excessively.

The particle properties, density and dielectric constant, were not evaluated with high precision due to probable lack of experimental results in the literature. Better estimates would be nice to know but maybe not necessary. The dielectric constant only appears in the factor $\kappa = (\epsilon_r - 1)/(\epsilon_r + 1)$ of the image potential term not important for particles bigger than 0.1 μm. This means that the significance of exact knowing of the dielectric constant is really only important if it is expected that $\epsilon_r \rightarrow 1$ and particles are small

enough. Particle density for its part influences on particle mass. However, for spherical particles the relationship between mass and density is linear, and is somewhat overshadowed by the proportionality to the cubic of the particle diameter. Thus, since it is well known that the inertial effects can be neglected at least up to 10 μm, diameter is really the parameter to describe to particle behavior. Consequently, when it comes to the further considerations on the theme of this thesis, including the phenomena and unidealizations such as coagulation, turbulence and dust layer build up might be of interest.

To conclude, based on the ideal case physical phenomena simulated, building an ESP for small-scale combustion appliances seems feasible. The possible problems that will be encountered thus supposedly relate to practical issues such as maintenance and rapping.

References

[1] W.C. Hinds, *Aerosol Technology: Properties, behavior, and measurement of airborne particles*. USA: John Wiley & Sons, 1982.

[2] K.R. Parker, Ed., *Applied Electrostatic Precipitation*. London: Blackie Academic & Professional, 1997.

[3] COMSOL Technical Staff, *COMSOL Multiphysics User's Guide*, Version 3.4, 2007.

[4] E. Guyon, J-P. Hulin, L. Petit and C.D. Mitescu, *Physical Hydrodynamics*, English ed. New York: Oxford University Press, 2001.

[5] M. Lehto, *Fysiikan matemaattiset perusteet 2*, Laitosraportti 1/2001. Jyväskylä: Fysiikan laitos, Jyväskylän yliopisto, 2001.

[6] I.S. Grant and W.R. Philips, *Electromagnetism*, 2nd ed. England: John Wiley & Sons, 1990.

[7] K. Parker and N. Plaks, *Electrostatic Precipitator (ESP) Training manual*, EPA-600/R-04/072, United States Environmental Protection Agency, July 2004.

[8] J. Tissari, *et al.*, "Puun pienpolton pienhiukkaspäästöt," Kuopion yliopiston ympäristötieteiden laitosten monistesarja, Kuopion yliopisto, Ympäristötieteiden laitos, Kuopio, Finland, 2004.

[9] Rüegg Cheminée AG, [Online]. Available: `http://www.ruegg-cheminee.com/ww/it/pub/prodotti/filtro_antiparticolato/risultato.htm#page_top`. [Accessed: 23.03.2008].

[10] R.O. Salonen, A. Pennanen and T. Paukku, ed, "Pienhiukkasten vaikutus terveyteen," Tuloksia ja päätelmiä teknologiaohjelmasta FINE Pienhiukkaset - Teknologia, ympäristö ja terveys, Finland, 2006.

[11] I. Talka, "Pienpolton hiukkasten sähköinen suodattaminen", Master's Thesis, Jyväskylän yliopisto, Fysiikan laitos, Jyväskylä, Finland, 2006.

[12] I. Salma, I. Balásházy, W. Hofmann and G. Záray, "Effect of physical exertion on the deposition of urban aerosols in the human respiratory system," *Journal of Aerosol Science*, vol. 33, pp. 983-997, July 2002.

[13] Comission of the European Communities, "Communication from the Comission to the Council and the European parliament, Thematic Strategy on air pollution," 21.9.2005. [Online]. Available: http://eur-lex.europa.eu/LexUriServ/site/en/com/2005/com2005_0446en01.pdf. [Accessed: 12.02.2008].

[14] Council of the European Union, "Information note," 15.3.2006. [Online]. Available: http://ec.europa.eu/environment/air/cafe/pdf/council_concl_them_strategy.pdf. [Accessed: 12.02.2008].

[15] Comission of the Europen Communities, "Proposal for a Directive of the European Parliament and of the Council on ambient air quality and cleaner air for Europe," 21.9.2005. [Online]. Available http://ec.europa.eu/environment/air/cafe/pdf/com_2005_447_en.pdf. [Accessed: 13.2.2008].

[16] Comission of the European Communities, "Comission Staff Working Paper, Annex to: The Communication on Thematic Strategy on Air Pollution and The Directive on 'Ambient Air Quality and Cleaner Air for Europe', Impact Assessment," 21.9.2005. [Online]. Available: http://ec.europa.eu/environment/air/cafe/pdf/ia_report_en050921_final.pdf. [Accessed: 15.02.2008].

[17] Comission of the European Communities, "Citizen's summary, EU climate and energy package," [Online]. Available: http://ec.europa.eu/climateaction/docs/climate-energy_summary_en.pdf. [Accessed: 03.02.2009].

[18] World Health Organization, "Air Quality Guidelines, Global Update 2005," [Online]. Available: http://www.euro.who.int/Document/E90038.pdf. [Accessed: 21.02.2008].

[19] L.S. Johansson, B. Leckner, L. Gustavsson, D. Cooper, C. Tullin and A. Potter, "Emission characteristics of modern and old-type residential boilers fired with wood logs and wood pellets," *Atmospheric Environment*, vol. 38, pp. 4183-4195, Aug. 2004.

[20] W.Peukert and C. Wadenpohl, "Industrial separation of fine particles with difficult dust properties," *Powder Technology*, vol. 118, pp. 136-148, Aug. 2001.

[21] S. Penttinen, "Method and device for purifying flue gas containing fine particles," European Patent Application EP 1 955 755 A2, August 13, 2008.

[22] L. Cañadas, B. Navarrete and L. Salvador, "Theoretical modeling of electrostatic precipitators performance (PRELEC code)," *Journal of Electrostatics*, vol. 34, pp. 335-353, May 1995.

[23] G. Skodras, S.P. Kaldis, D. Sofialidis, O. Faltsi, P. Grammelis and G.P. Sakellaropoulos, "Particulate removal via electrostatic precipitators - CFD simulation," *Fuel Processing Technology*, vol. 87, pp. 623-631, July 2006.

[24] Y. Zhuang, Y.J. Kim, T.G. Lee and P. Biswas, "Experimental and theoretical studies of ultra-fine particle behavior in electrostatic precipitators," *Journal of Electrostatics*, vol. 48, pp. 245-260, March 2000.

[25] A. Jaworek, T. Czech, E. Rajch and M. Lackowski, "Laboratory studies of back-discharge in fly ash," *Journal of Electrostatics*, vol. 64, pp. 326-337, May 2006.

[26] E. Hedberg, *et al.*, "Chemical and physical characterization of emissions from birch wood combustion in a wood stove," *Atmospheric Environmental*, vol. 36, pp. 4823-4837, Oct. 2002.

[27] G. Biskos, E. Mastorakos and N. Collings, "Monte-Carlo simulation of unipolar diffusion charging for spherical and non-spherical particles," *Journal of Aerosol Science*, vol. 35, pp. 707-730, June 2004.

[28] G. Biskos, K. Reavell and N. Collings, "Unipolar diffusion charging of aerosol particles in the transition regime," *Journal of Aerosol Science*, vol. 36, pp. 247-265, Feb. 2005.

[29] D.Y.H Pui, S. Fruin and P.H. McMurry, "Unipolar diffusion charging of ultrafine aerosols," *Aerosol Science and Technology*, vol. 8, pp. 173-187, 1988.

[30] W.A. Hoppel and G.M. Frick, "Ion-aerosol attachment coefficients and the steady-state charge distribution on aerosols in a bipolar ion environment," *Aerosol Science and Technology*, vol. 5, pp. 1-21, Jan. 1986.

[31] N.A. Fuchs, "On the stationary charge distribution on aerosol particles in a bipolar ionic atmosphere," *Geofisica pura e aplicata*, vol. 56, pp. 185-193, 1963.

[32] J. Gentry and J.R Brock, "Unipolar diffusion charging of small aerosol particles," *The Journal of Chemical Physics*, vol. 47, pp. 64-69, July 1967.

[33] J. Brock, 1970, "Unipolar diffusion charging of aerosols and image force," *Journal of Colloid and Interface Science*, vol. 33, p. 473, 1970.

[34] A. Manquard, "Unipolar field and diffusion charging in the transition regime - part 1: A 2-D limiting-sphere model," *Aerosol Science and Technology*, vol. 41, pp. 597-610, June 2007.

[35] A. Laitinen, A. Rostedt, M. Lemmetty and J. Keskinen, "Sähkösuodattimen esivarausjärjestelmä," Tampereen teknillinen yliopisto, Fysiikan laitos, Aerosolifysiikan laboratorio, Tampere, Finland, Loppuraportti 308/31/03, 2003.

A Appendix, Particulate Matter Deposition in the Human Organism

In Figure 45 information about fine particle deposition in a human organism is provided in order to be able to compare its particle size dependence to that of the collection efficiency of an ESP. Reviewing Figures 7 and 15 one finds the somewhat consoling fact that, around 0.4 μm where the particle size distribution approaches its maximum and collection efficiency has its minimum for combined charging, the total deposition into human organism, for its part, has a minimum.

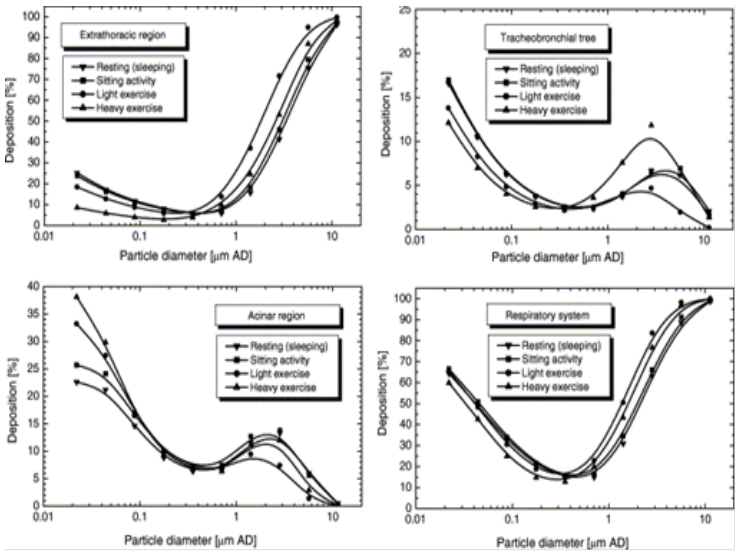

Figure 45: Deposition in the extrathoracic, tracheobronchial and acinar regions, and in the total respiratory system as function of the aerodynamic diameter computed for an adult male under resting (sleeping), sitting activity, light exercise and heavy exercise breathing conditions. [12]

B Appendix, Health Impact Of Particulate Matter Exposure

To justify and better illustrate the statements of Chapter 2, tabulated data on health hazards of particulate matter exposure is supplied.

Table 1: Health impacts caused by PM2.5 exposure [10]. (Edited and translated).

Assessed health hazard	**EU25**	**Finland**
Premature deaths	347 900	1 270
Life years lost	3 618 700	13 840
Deaths (0-1 y)	677	2
Chronic brochitis (27y ->)	163 800	620
Hospital entranses due to respiratory and cardiovascular diseases (0-100 y)	100 300	383
Days of use of medication for respiratory diseases(5-14 y)	4 218 500	11 310
Days of use of medication for respiratory diseases (20 y ->)	27 741 700	104 450
Days with symptoms in lower respiratory system (5-14 y)	192 756 400	778 870
Days with imperfect working ability (15-64 y)	347 687 000	1 323 390
Economical losses	268-781 billion euros per annum	1-2 billion euros per annum

C Appendix, The Structure of the Rotating Plate ESP

Numbering of the ESP components

0. Flue gas inlet
1. Rotating axle
2. Collector plate, negative potential
3. Hood of the precipitator, grounded
4. Grounded plate
5. Insulator, on which the collector plate is mounted
6. Axle of the blade system
7. The blade system
8. Hopper
9. Support structure for the blade system

The Structure of Rotating Plate ESP

The precipitator described below is two-stage by type and the flue gas particulates are assumed to arrive to the precipitation stage positively charged, implying that the collector electrode has to be connected to negative potential. Thus positive corona charger is assumed to be used in charging stage. Compared to negative corona the positive one has the advantages of substantially reduced ozone emissions and the possibility to ground all the parts of the precipitator excluding the negative collector plates.

The precipitator consists essentially of at least one rotating collector plate 2, connected to a rotating axle 1, which both are enclosed with a grounded hood 3. If more than one collector plate is present, then grounded rotating electrodes 4, connected to the same rotating axle, are also utilized. Cleaning of the plates is realized rotating the plates connected to axle such a way that mechanical contact is applied between a fixed bade system 7. The dust is then removed to a hopper 8, taking advantage of gravity. The appearance of the precipitator is sketched in Figures 46 and 47, in the latter especially illustrating the easy and independent removal of the plate stack and the blade system.

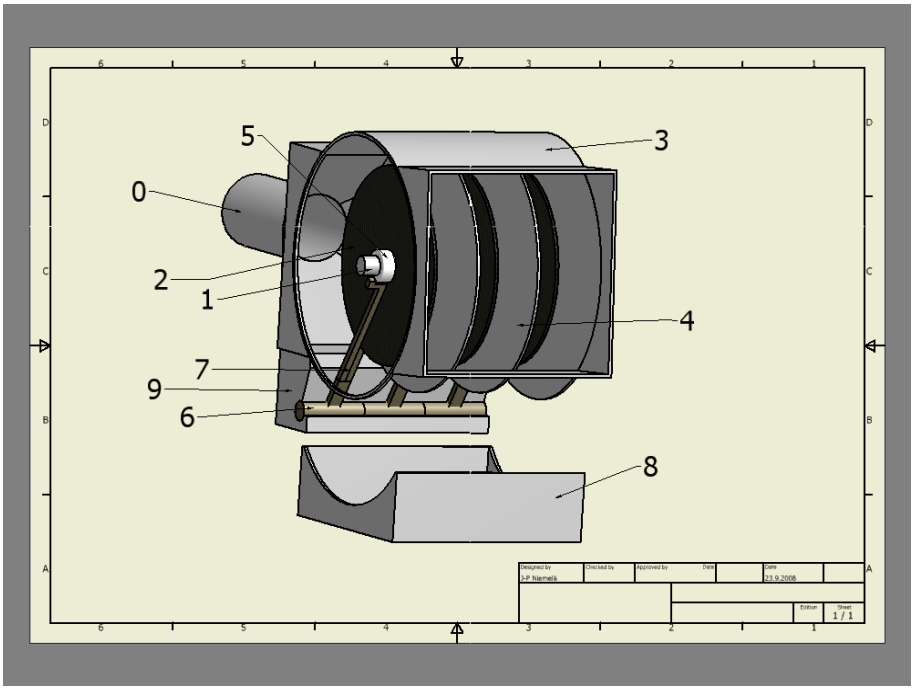

Figure 46: The structure of the rotating plate ESP.

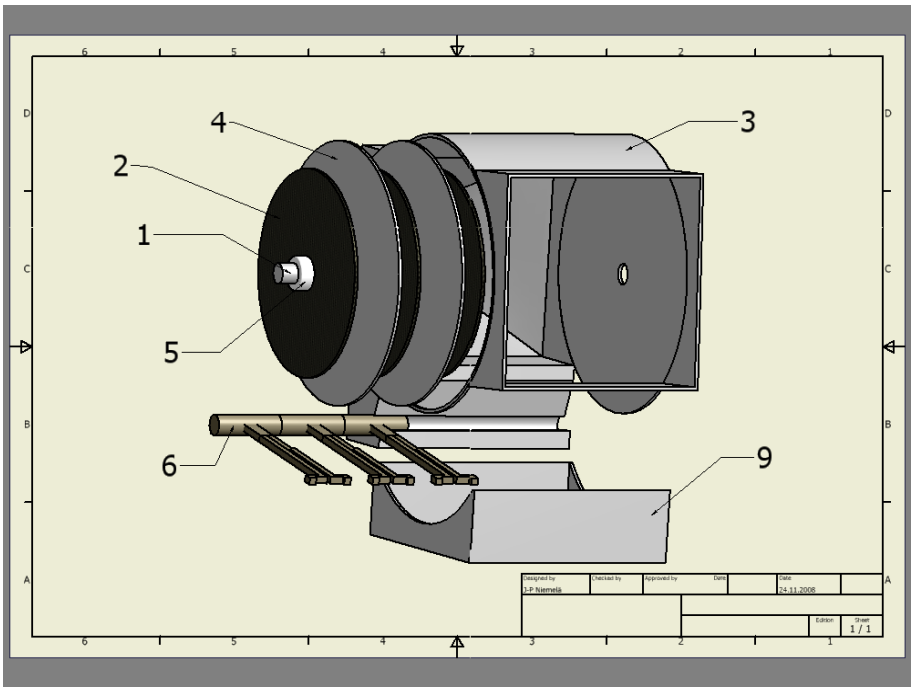

Figure 47: The structure of the rotating plate ESP - easy removal of the blade system and the plate stack.

D Appendix, The Structure of the Helicoidal ESP

Figures 49 and 48 are provided to illustrate the invention of Ismo Talka. Flue gas is fed through a flow channel consisting of two coaxial helixes and a tube. Through the inner, smaller helix negative potential is provided, whereas the outer, larger helix and the tube serve as collection surfaces. Furthermore, the larger helix is intended to function as a transport screw to export the dust from the tube surfaces into a hopper.

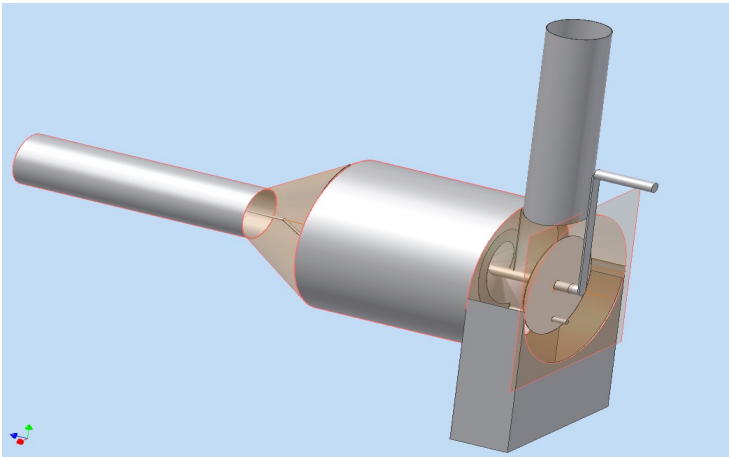

Figure 48: The helicoidal ESP configuration.

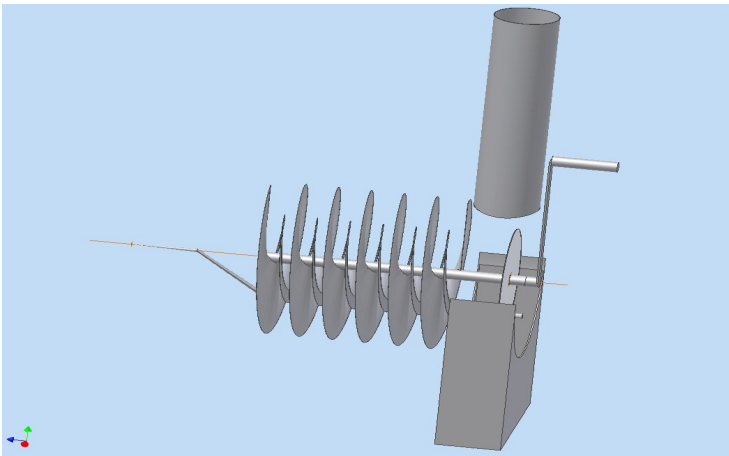

Figure 49: The helicoidal ESP configuration - the inlet tube and the cylinder walls stripped.

E Appendix, Resolving the Problems in Below-$1\mu m$ Particle Tracing with 'the Equivalence Velocity Principle'

Particle tracing exhibits for particles small enough, that is, for particles below 1 μm in diameter, about the problem of memory and time consumption due to need for additional calculation steps.

The problem can be avoided by introducing a concept of 'equivalent velocity'. By applying 'the equivalent velocity principle' we can obtain equal trajectories for particles of different sizes. We take d_1 and V_{mean1} to be the particle diameter small enough to cause problems for trajectory modeling and the mean fluid velocity in the precipitator domain, respectively, whereas d_2 and V_{mean2} stand for the diameter and the fluid velocity for which the modeling is easily feasible. These two cases are set equal in the sense of Deuch-Anderson collection efficiency, Eq. (80), further substituting in the equations presented in Chapter 6 and noting for a moment the exponential power term by C we write:

$$
\begin{aligned}
\eta_{DA1}\left(d_1, V_{mean1}\right) &= \eta_{DA2}\left(d_2, V_{mean2}\right) \\
\Leftrightarrow 1 - exp(C_1) &= 1 - exp(C_2) \\
\Leftrightarrow C_1 &= C_2 \\
\Leftrightarrow \frac{w_{th1}L}{V_{mean1}s} &= \frac{w_{th2}L}{V_{mean2}s} \\
\Leftrightarrow \frac{w_{th1}}{V_{mean1}} &= \frac{w_{th2}}{V_{mean2}} \\
\Leftrightarrow V_{mean2} &= \frac{w_{th2}}{w_{th1}} V_{mean1} \\
\Leftrightarrow V_{mean2} &= \frac{Q_{p2}(d_2)EC_{c2}(d_2)}{3\pi\eta d_2} \frac{3\pi\eta d_1}{Q_{p1}(d_1)EC_{c1}(d_1)} V_{mean1} \\
\Leftrightarrow V_{mean2} &= \frac{Q_{p2}(d_2)C_{c2}(d_2)}{d_2} \frac{d_1}{Q_{p1}(d_1)C_{c1}(d_1)} V_{mean1} \\
\Leftrightarrow V_{mean2} &= \frac{Q_{p2}(d_2)}{Q_{p1}(d_1)} \frac{C_{c2}(d_2)}{C_{c1}(d_1)} \frac{d_1}{d_2} V_{mean1}.
\end{aligned}
$$

We have now derived an equation for equivalence fluid velocity V_{mean2} for particle $d_2 > 1\ \mu m$ to give equal trajectory to that of particle $d_1 < 1\ \mu m$ immersed in a fluid flowing with velocity V_{mean1}.